AFOSR - TR - 77 - 0258

ADA038205

NEAR-FIELD SEISMOGRAMS FROM A TWO-DIMENSIONAL PROPAGATING DISLOCATION

By

Joe Jean Litehiser, Jr.

DISSERTATION

1976

DDC
RECEIVED
APR 8 1977
D

GRADUATE DIVISION
of the
UNIVERSITY OF CALIFORNIA, BERKELEY

AD No. ____
DDC FILE COPY

DISTRIBUTION STATEMENT A
Approved for public release;
Distribution Unlimited

AIR FORCE OFFICE OF SCIENTIFIC RESEARCH (AFSC)
NOTICE OF TRANSMITTAL TO DDC
This technical report has been reviewed and is approved for public release IAW AFR 190-12 (7b).
Distribution is unlimited.
A. D. BLOSE
Technical Information Officer

UNCLASSIFIED

SECURITY CLASSIFICATION OF THIS PAGE (When Data Entered)

REPORT DOCUMENTATION PAGE

READ INSTRUCTIONS BEFORE COMPLETING FORM

AFOSR - TR - 77 - 0258

4. TITLE (and Subtitle)

NEAR-FIELD SEISMOGRAMS FROM A TWO-DIMENSIONAL PROPAGATING DISLOCATION.

5. TYPE OF REPORT & PERIOD COVERED

Interim rept.

6. PERFORMING ORG. REPORT NUMBER

7. AUTHOR(s)

Joe Jean Litehiser, Jr

8. CONTRACT OR GRANT NUMBER(s)

F44620-75-C-0049

ARPA Order-2134

9. PERFORMING ORGANIZATION NAME AND ADDRESS

University of California, Berkeley
Seismographic Station
Berkeley, California 94720

401665

10. PROGRAM ELEMENT, PROJECT, TASK AREA & WORK UNIT NUMBERS

ARPA Order No. 2134
Program Code 2F10

11. CONTROLLING OFFICE NAME AND ADDRESS

Defense Advanced Research Projects Agency
1400 Wilson Boulevard
Arlington, Virginia 22209

12. REPORT DATE

1976

13. NUMBER OF PAGES

184

14. MONITORING AGENCY NAME & ADDRESS(if different from Controlling Office)

Air Force Office of Scientific Research
Bolling AFB, Bldg.#410
Washington, D. C. 20332

193p.

15. SECURITY CLASS. (of this report)

UNCLASSIFIED

15a. DECLASSIFICATION/DOWNGRADING SCHEDULE

16. DISTRIBUTION STATEMENT (of this Report)

Approved for public release; distribution unlimited

17. DISTRIBUTION STATEMENT (of the abstract entered in Block 20, if different from Report)

18. SUPPLEMENTARY NOTES

TECH, OTHER

19. KEY WORDS (Continue on reverse side if necessary and identify by block number)

seismology
earthquake
dislocation source
strong ground motion
San Fernando earthquake

20. ABSTRACT (Continue on reverse side if necessary and identify by block number)

The exact mathematical formulation for displacements on the surface of an isotropic, homogeneous, perfectly elastic half-space due to an embedded line dislocation source is developed and used to model the observed strong-motion accelerometer records generated at Pacoima Dam during the San Fernando earthquake of February 9, 1971.

DD FORM 1473 EDITION OF NOV 65 IS OBSOLETE

401665

Near-Field Seismograms from a Two-Dimensional Propagating Dislocation

By

Joe Jean Litehiser, Jr.

A.B. (Indiana University) 1969
M.A. (University of California) 1970

DISSERTATION

Submitted in partial satisfaction of the requirements for the degree of

DOCTOR OF PHILOSOPHY

in

Geophysics

in the

GRADUATE DIVISION

of the

UNIVERSITY OF CALIFORNIA, BERKELEY

Approved:

Lane R. Johnson

Bruce A. Bolt

J. J. Sackman

Committee in Charge

DDC
RECEIVED
APR 8 1977
D

White Section
Buff Section
AVAIL. and/or SPECIAL
A

DISTRIBUTION STATEMENT A
Approved for public release;
Distribution Unlimited

NEAR-FIELD SEISMOGRAMS FROM A TWO-DIMENSIONAL PROPAGATING DISLOCATION

ABSTRACT

Joe Jean Litehiser, Jr.

The exact mathematical formulation for displacements on the surface of an isotropic, homogeneous, perfectly elastic half-space due to an embedded line dislocation source is developed after the method of Cagniard (1939) as modified by de Hoop (1960). This formulation is then used to model the observed strong-motion accelerometer records generated at Pacoima Dam during the San Fernando earthquake of February 9, 1971.

A number of model accelerograms are generated using several dislocation time histories, fault geometries, and fault rupture propagation velocities. The dislocation time histories considered are the simple finite ramp and its first and second order continuous counterparts for rise times of 0.1, 0.25, and 0.5 seconds. The two fault geometries used are planar, after Canitez and Toksöz (1972), and hinged, after Alewine and Jordan (1973). Finally, fault rupture propagation velocities are considered over the approximate range of from 2.0 kilometers/second to 2.5 kilometers/second.

Within the limitations of the mathematical idealizations used it is found that the faulting process of the San Fernando earthquake is best represented by a dislocation whose time history at any point on the fault is that of a second order continuous smoothed finite ramp of 0.25 second rise time propagating at approximately 2.3 kilometers/second over a hinged fault surface. The average dislocation amplitude as constrained by the observed Pacoima Dam peak acceleration in that part of the record for which a model motion match is successful is between one and two meters.

One fundamental difficulty with all models tried is the failure to match both vertical and horizontal observed motions simultaneously. In general, the vertical component is more successfully duplicated. This problem is not resolved by this study.

Lane R. Johnson

To Happy's

ACKNOWLEDGMENTS

I am indebted to Professor Lane R. Johnson for his suggestion of this topic and for his guidance during its investigation. I also thank Dr. Bruce A. Bolt for expressing interest throughout and for carefully reading the finished manuscript, and Mr. C. R. McClure of Bechtel Inc. for his active encouragement. The present study was supported, in part, by the Advanced Research Projects Agency of the Department of Defense and was monitored by the Air Force Office of Scientific Research under F44620-75-C-0049.

Finally, I would like to express my gratitude to my parents who provided moral support throughout my somewhat overlong academic career, to Dr. C. P. Ocampo who provided friendship as well as a great deal of indirect financial support, to my children, Jeni Lynn and J.R., who by their daily growth provided a constant and gentle reminder that I too must continue to grow, and to my wife Soxy, whose love is at the very center of my world.

Table of Contents

	Page
Dedication	i
Acknowledgments	ii
Table of Contents	iii
Chapter 1 Introduction and Review of Previous Studies	1
1.1 Introduction	1
1.2 Review of Previous Studies	2
Chapter 2 The Green's Functions of the Problem	18
2.1 Some Basic Considerations	18
2.2 The Green's Functions	23
2.21 The $\zeta \rightarrow z$ Inverse Transform and Boundary Conditions	27
2.22 The $\xi \rightarrow x$ and $s \rightarrow t$ Inverse Transforms	35
2.23 Spatial Derivatives of the Green's Functions	47
Chapter 3 Development of Several Source-Instrument Terms	57
3.1 Introduction	57
3.2 The Strong-Motion Instruments	57
3.3 The Time History of a Point Source	62
3.31 The Source as a Finite Ramp Function	63
3.32 The Source as a Finite Ramp Function with Continuous First Derivatives	66
3.33 The Source as a Finite Ramp Function with Continuous First and Second Derivatives	70
3.34 Comparison of the Source Terms	75
3.4 Additional Parameters	78
Chapter 4 Comparison of Model and Actual Accelerograms	84
4.1 Introduction	84
4.2 The Pacoima Dam Accelerograms	86

		Page
4.3	Presentation of Model Accelerograms	93
	4.31 Model Accelerograms from a Planar Fault	109
	4.32 Model Accelerograms from a Hinged Fault	143
4.4	Discussion of the Results	164
Chapter 5	Conclusions and Areas for Future Study	177
References		181

Chapter 1

INTRODUCTION AND REVIEW OF PREVIOUS STUDIES

1.1 Introduction

The San Fernando earthquake of February 9, 1971 was the most damaging earthquake in the United States since the Alaskan earthquake of 1964. Although only a moderate event of magnitude 6.5, sixty-four lives were lost and property damage in excess of five hundred fifty million dollars occurred. Both of these numbers could very easily have been much larger as the near failure of the lower Van Norman Dam convincingly indicates.

This earthquake was also important from a scientific viewpoint. Occurring in a metropolitan region, it provided a valuable test of the adequacy of modern engineering design practices. Many structures, most notably Olive View Hospital and many freeway overpasses, did not perform up to expectations. There is obviously still much to learn in the area of earthquake-resistant design. Seismologically, this earthquake presents many unique opportunities. The faulting episode with which it was associated had a large thrust component. This is unusual in California where the vast majority of seismic activity is related to strike-slip movement along the San Andreas fault and its branches. Most important, however, is the vast number of high-quality, strong-motion records obtained from this single event--more, indeed, than in all previous earthquakes combined.

One record in particular of these, that generated at Pacoima Dam, is especially significant because it presents a recording of strong ground motion at a site directly above the region of faulting. The endeavor here is to seek a description in some detail of the faulting

process associated with the San Fernando earthquake of February 9, 1971 as evidenced by the strong-motion record written at Pacoima Dam.

This is an inverse problem of some complexity which will depend for success upon the applicability of the medium transfer function used as well as upon the judicious use of the work of many previous investigators on the subject of seismic sources in general and on the source of of the San Fernando earthquake in particular.

In this chapter we shall briefly review that small portion of the literature that is of immediate significance to the evolution of the ultimate conclusions of this thesis. This review is by no means exhaustive but is, it is hoped, adequate to indicate the original impetus for this research.

1.2 Review of Previous Studies

Previous solutions to the inverse problem posed by the large and varied data set of the San Fernando Valley earthquake have incorporated mathematical idealizations of many forms. Indeed, several important papers discuss the problem in almost purely qualitative terms, and many early papers take a comprehensive approach using data of several different forms to compliment one another, using them collectively to generate a complete conception of the faulting process of the event. For the purposes of this introduction it is useful to classify previous investigations as being essentially quantitative or qualitative, by the dominant frequency range of ground motion considered, and by the distance from the source region of the data analyzed. Such a classification scheme is largely superficial but by considering first those papers employing long period or teleseismic data and then those studies using increasingly higher frequency, closer observations it is hoped that the method of

this thesis may be seen as a logical continuation of the evolution of the understanding of the seismic source.

An important attempt aimed at satisfying several teleseismic and static manifestations of the San Fernando earthquake of February 9, 1971 is undertaken in the paper of Canitez and Toksöz (1972). These authors wish to determine this event's source mechanism characteristics by analysis of the polarity of teleseismic P- and S-waves, of the spectra of surface waves (also at teleseismic distances) and of the static displacements, strains, and tilts in the source area.

The groundwork necessary to the calculation of near-field static fields has been profitably researched in a number of papers (Steketee, 1958; Chinnery, 1963; Maruyama, 1964; Mansinha and Smylie, 1971). Using the formulation of Maruyama (1964) which may be integrated numerically over a fault surface composed of discrete dislocations of arbitrary orientation in a half-space, Canitez and Toksöz calculate the pertinent static fields. The solution is constrained so that the fault surface is planar and rectangular with the sides of the rectangle being parallel or perpendicular to the surface of the earth. A constant amplitude of dislocation over the fault surface was also assumed. Within these constraints the authors find that the static strain steps recorded at Isabella, the Nevada Test Site, and San Diego (Jungels and Anderson, 1971; Berger, 1971) as well as the vertical displacements near the surface fault trace (Burford et al, 1971) may generally be fit by a single theoretical model whose parameters appear in Table 1-1.

A dynamic source model is also calculated by the authors on the basis of polarity of first P-wave arrivals at one hundred twenty-eight stations and from the spectra of the vertical components of Rayleigh

wave motion at six stations. In the first motion polarity studies, angle of incidence tables of Nuttli (1969) are used for computing the reduced distances using a focal depth of 15 kilometers. In the Rayleigh wave study the average continental crust and upper mantle model of Canitez and Toksöz (1971) is used. For attenuation corrections constant Q values are used in two intervals: Q = 175 for periods of from 10 to 28 seconds, and Q = 200 for longer periods. These are chosen as being in the mid-range of measured Rayleigh wave Q values of Tsai and Aki (1969) and Solomon (1971). The source parameters obtained from this part of the study are also summarized in Table 1-1 and are in substantial agreement with the statically constrained parameters.

The authors feel that, using extreme values allowable for Q, the depth of the initial rupture may vary by ± 4 kilometers without destroying the distinctive character of the surface wave spectra at several stations.

For the purposes of the present study the most important parameters derived in this paper are the dip of the fault plane at 52 degrees and the focal depth of approximately 14 kilometers. The primary datum constraining the dip angle is the fault plane solution derived from first motion polarity values. As Canitez and Toksöz note, this datum is most pertinent to that part of the fault where rupture is initiated, inferred to be at the lower end of the fault plane. The focal depth of 14 kilometers is supported by all dynamic evidence within the uncertainty mentioned above.

One difficulty with the Canitez and Toksöz study is the teleseismic distances at which all dynamic data are evaluated. Some spherically symmetric model of the earth is implicit in all teleseismic data

inversion schemes. Any departure of the real earth from this ideal model will result in a biased determination of the source parameters and the longer the wave transmission path the greater will be the likelihood of such a departure. Furthermore, far-field data can give no direct measure of the ability of a source model to explain near-field ground motions which are of great theoretical and practical importance. For these reasons some benefit is to be expected from the consideration of near-field data.

This is done by Mikumo (1973) as part of another comprehensive approach to source parameter determination for the San Fernando earthquake. Mikumo carries out a detailed investigation of the source mechanism using vertical and horizontal displacement, strain, and tilt data, dynamic ground motions in the near-field, and the spatial distribution of aftershocks and features of the surface fault break.

The study of the static displacements undertaken by Mikumo is essentially identical to that of Canitez and Toksöz (1972). A slightly more general fault geometry is considered based on evidence of the spatial distribution of aftershocks (Allen et al, 1971; Wesson et al, 1971; Hanks et al, 1971; Allen et al, 1972; Bolt and Gopalakrishnan, 1975), of focal mechanism solutions (Whitcomb, 1971; Canitez and Toksöz, 1972), and surface faulting (Kamb et al, 1971; U. S. Geological Survey Staff, 1971). The fault surface is still planar and approximately rectangular, but it is tilted so that it intersects the ground surface obliquely. This has the effect of truncating one corner of the fault plane at the ground surface, the strike of this truncation being approximately that of the surface expression of the observed fault.

Mikumo also wishes to explore the effects of allowing the

amplitude of dislocation to vary over the fault surface. Since pre-earthquake stresses and frictional stress during faulting may not be uniformly distributed with depth (Chinnery and Petrak, 1968), several schemes of dislocation amplitude variation are considered and their resulting static surface displacements compared with those observed near the fault break. In all cases dislocation amplitude is assumed to decrease with depth, either linearly or exponentially attaining zero displacement near the hypocenter. Several of the exponential decay schemes are found to best fit the observations. Thus, it is found that static displacements may be fit by a roughly rectangular fault of approximately 14 kilometer length and 19 kilometer width, intersecting the ground somewhat obliquely, with the dislocation amplitude having a maximum of 3.5 to 4.5 meters at the surface and decreasing exponentially with depth.

Mikumo's dynamic displacement model analysis is of a much different type than that of Canitez and Toksöz (1972). Here an attempt is made to calculate the theoretical dynamic displacements appropriate to the source-receiver geometries at the Pacoima Dam and Pasadena Seismological Laboratory strong-motion recording sites using the pertinent fault parameters developed in the static part of the study and the near-field displacement formulation of Maruyama (1963) and Haskell (1969) which apply to moving dislocations in an infinite homogeneous medium. It is reasonable to suppose that such a transfer function may successfully be used to model direct P and S body wave motion (with the exception of amplitude) although waves that depend explicitly on the existence of a surface and on more complex medium geometries will not be adequately modeled.

Some parameters necessary to the consideration of a dynamic model are, of course, unrecoverable from static data. Such parameters are the time history of the dislocation at any given point on the fault and the fault propagation velocity. Mikumo assumes a Haskell (1969) finite ramp dislocation time history with rise time between 0.2 and 4 seconds. Several different modes of fault rupture are considered corresponding to several orientations of the fault slip vector, and rupture propagation velocity is allowed the discrete values of 2.0, 2.5, or 3.0 kilometer/second. The P-wave velocity in the epicentral region is taken to be 6.10 kilometer/second from seismic refraction studies by Wesson and Gibbs (1971). The S-wave velocity is then approximated by 3.5 kilometer/second assuming the customary Poisson's ratio of 0.25.

The somewhat complex modes of fault propagation chosen by Mikumo require numerical integration of the appropriate equations. There is, of course, nothing in the Haskell or Maruyama formulation to preclude contributions to the ground displacements from all frequencies including zero frequency. However, since he wishes to compare his results with the data of Trifunac and Hudson (1971) which represents the band limited approximation to the real ground displacement between essentially 0.04 and 15 seconds, Mikumo approximates this band limiting process by applying a boxcar bandpass filter with cutoff frequencies of 25 and 0.05 Hertz to his raw ground displacements. In this way direct comparison of data and theoretical displacements are made.

It is concluded on the basis of such comparisons that fair agreement in waveform, arrival time, and absolute amplitude is obtained for propagation velocities of 2.5 kilometer/second or slightly less and for rise times between 0.6 and 1.2 seconds. Generally satisfactory

agreement is obtained between the theoretical and observed ground displacements at the Pasadena Seismological Laboratory using similar fault motion parameters. Appropriate fault parameters derived in this study are summarized in Table 1-1.

Trifunac (1974) undertakes a very similar dynamic motion study of the implications to the source mechanism of various San Fernando earthquake strong-motion records. He, however, considers the strong-motion records of five stations (Pacoima Dam; 8244 Orion Blvd., 1st floor; Jet Propulsion Laboratory basement; Palmdale Fire Station; Castaic Old Ridge Route) and allows considerably more complexity in his fault geometry. The fault remains planar but now is broken into irregular rectangular subareas whose dislocations are allowed to differ from each other in both amplitude and direction within the plane of the fault. The medium transfer function is again that of a homogeneous, isotropic whole-space as developed by Haskell (1969). The inversion procedure itself, however, is more formalized in that, having specified the final fault shape, the best values for fault propagation velocity, slip direction and amplitude, and the rise time are determined in the least squares sense.

In this study Trifunac, as Mikumo before him, uses near-field displacements as the data to be inverted rather than velocities or accelerations. This is done because fewer inadequacies in the whole-space medium transfer function are likely to manifest themselves at the lower frequencies apparent in displacements as opposed to velocity and acceleration records. This contention is supported by several recent studies (e.g., Reimer, 1973; Trifunac, 1973; Boore, 1972; Smith, 1975). The conclusions reached as a basis of this study are listed in Table 1-1.

Table 1-1

Model Parameters from Previous Studies

	Fault Characterization	Fault area (km^2)	Dip (deg)	Focal Depth (km)	$\overline{\Delta u}$ (m)	Rupture Velocity (km/sec)	Rise Time (sec)
Canitez & Toksoz (1972)							
Static Study	planar and rectangular	196	52	11	2.8	-	-
Dynamic Study	-	-	-	14	-	-	-
Mikumo (1973)							
Static Study	planar and ~ rectangular	255	52	13	1.4	-	-
Dynamic Study	-	-	-	-	-	2.5	0.16-1.2
Trifunac (1974)	planar and of irregular shape	130	40	9.2	3.9	2.0	0.5-1.0

All studies considered so far treat the fault as planar with a single dip angle for all segments of the fault. There was growing evidence, however, that the fault might be more accurately represented by a curved surface with dip decreasing as successively shallower segments of the fault were considered. For example, fault plane solutions derived from first motion studies indicated an initial fault dip angle of approximately 52 degrees (Canitez and Toksöz, 1972; Mikumo, 1973) while surface and near-surface fault expression indicated a fault plane of much shallower dip angle (Kamb et al, 1971). This is suggestive of a curved fault surface and this interpretation is consistent with the aftershock data. Static dislocation models that incorporated the curved or hinged fault plane concept (Jungels, 1973; Alewine and Jordan, 1973) were also shown to be compatible with the observed static surface displacements.

Turnbull and Battis (1973) in a continuation of earlier work began by Tsai and Patton (1972; 1973) brought the hinged fault model under consideration for the near-field dynamic analysis of the Pacoima Dam strong-motion record. In this study comparison is made between the computed Pacoima Dam velocity waveforms (Trifunac and Hudson, 1971) and the whole-space theoretical velocity waveforms computed from the Haskell (1969) formulation as in previous papers considered above. The hinged fault effect is obtained by linearly summing the contributions from several planar Haskell-type faults with delay times properly arranged to simulate continuous fault propagation from one segment to the next.

Besides orientation, such parameters as rupture velocity, dislocation amplitude, and fault width are also conceptually allowed to vary between contiguous fault segments to generate a source model whose

complexity can match that of the observed velocity record. As in the study of Trifunac (1974) the inclusion of such complexity is an advantage that exacts its price. The final solution obtained takes advantage of the complete generality of the above formulation to only a limited extent. This solution consists of two planar segments, the lower dipping at 60 degress and the upper at 33 degrees. The lower segment is further divided into two co-planar segments while the upper segment is subdivided into three co-planar segments. The ranges of fault width, longitudinal (up dip) dislocation, and rupture propagation velocity among these segments are 12.0 to 16.0 kilometers, 100 to 250 centimeters, and 3.2 to 2.85 kilometer/second respectively. The functional form of the source, as in all previous dynamic studies, is the Haskell (1969) finite ramp whose rise time is found to be 0.6 seconds for all segments.

Turnbull and Battis feel that the fit of their generated waveforms to those observed is superior to previous efforts in at least one respect: the initial motion of the large pulse on the vertical record now has the currect polarity with their fault model. This is purely a result of the geometry of the above model. They also conclude that the rupture velocities of different segments of the fault are not well constrained by this approach within a moderate range.

It must be noted that even with the added complexity of the segmented fault the complexity of the motion after the large S-wave pulse is not well represented. This could be due to the failure of the Haskell transfer function used to explicitly consider the presence of the ground surface, any layering, or surface topography. Alternatively, it could be due to an insufficient number of fault segments. This

possibility is not explored since if rupture velocity, rise time, dip angle, dislocation amplitude, and fault width are allowed to vary for each of a large number of segments the inverse problem generall treated (even within narrow limits for all parameters) soon becomes unmanageable.

An alternative approach to extracting the sourch mechanism information contained in the Pacoima Dam strong-motion record may be characterized as semi-quantitative. In this approach an attempt is made to extract implications from the most fundamental data of seismology--phase arrival times. Two papers of this type are those of Bolt and Gopalakrishnan (1975) and Bolt (1972). In these papers the recorded components are resolved along directions parallel to the strike of the fault plane, down dip in the fault plane, and normal to the fault plane. This is done to facilitate the analysis in terms of elastic wave theory. The fault is modeled by a planar surface dipping at 45 degrees. Assuming P- and S-wave velocities of 5.5 and 3.3 kilometer/second, respectively, the salient features of the Pacoima records are explained in terms of direct P- and S-wave arrivals from the hypocenter and a later S arrival from a point on the fault closes to the Pacoima Dam site. Still later arrivals are conjectured to be due to S-wave arrivals from more distant points on the fault surface. The contribution of surface waves is not considered important in the near-field since their far-field dominance is due to the slower attenuation characteristic of surface waves relative to the attentuation of body waves.

Such an approach is very appealing in some respects. Primarily, it is tempting to apply intuition and knowledge of elastic wave behavior, gained almost exclusively from far-field observations, to a near-field

problem. However, conclusions reached from such analysis must be regarded as more circumstantial than those derived from more straightforward inversion techniques. This contention is supported by a similar study undertaken by Hanks (1974).

In this study a hinged fault plane similar to several considered before is favored and P- and S-wave velocities of 5.6 and 3.2 kilometer/second, respectively, are used. As in the previous study by Turnbull and Battis (1973) the fault geometry is found to conform to initial motion polarity requirements. It is also noted that the orientation of the deeper part of the fault is such that the P-wave excitation is near a minimum while the S-wave excitation is near a maximum, a circumstance that explains qualitatively the relative compressional wave-shear wave amplitudes apparent on all components of the Pacoima Dam strong-motion record. As in the previous studies of Bolt (1972) and Bolt and Gopalakrishnan (1975) explanations for several important phase arrivals on this record are sought which are understandable in terms of elastic wave arrivals from some part of the fault. Besides P- and S-waves from the initial rupture three other arrivals are investigated. The last of these, arriving at a time of approximately 7.3 seconds after the compressional wave, is interpreted as the breakout phase or that surface wave phase associated with the rupture of the earth's surface. No very convincing explanation is found for the two phases between this breakout phase and the initial S-wave arrival although the second of these is more impressive looking on the acceleration and velocity records than is the motion attributed to the surface rupture. Based primarily on the interpretation of this breakout phase arrival and the fault geometry a minimum fault propagation velocity of 3.8 kilometer/second is calculated.

As demonstrated by a comparison of the conclusions reached by Bolt and Bolt and Gopalakrishnan with those derived by Hanks, small uncertainties in model parameters such as seismic wave velocities or fault geometry may have profound implications to the faulting process as evidenced by the strong-motion data. Both analyses depend primarily on the interpretation of three arrival times--initial compressional and shear wave arrivals, and one later phase. In the case of Bolt this later phase arrives at approximately 3.9 seconds after the onset of the recorded motion and is explained in terms of an S-wave arrival from the point of closest approach of the fault surface to the Pacoima Dam Station. In Hanks' study, as we have seen, a later arrival is identified as the surface wave generated when the fault rupture reaches the surface. The phase arrives at over 7 seconds after the P-wave. In both cases the proper identification and interpretation of this later arrival provides a very important constraint on the fault rupture propagation velocity. The inherent difficulty in this type of study is made apparent by noting that the S-wave arrival time chosen by Bolt and Bolt and Gopalakrishnan is approximately 0.7 seconds earlier than that favored by Hanks. This is a significant difference over the short ray paths pertinent to a near-field study.

We have now briefly discussed a number of important contributions to the understanding of the faulting process associated with the February 9, 1971 San Fernando earthquake. It is obvious that a great deal has been learned and a great deal remains to be learned. For example, little has been determined regarding the details of the faulting episode at any one point on the fault. Is the time history of faulting adequately represented by a finite ramp displacement function? Is there

hope of recreating an acceleration record from some fairly simple medium transfer function or must substantial complexity be called upon? It is the purpose of this thesis to find the answers to these questions.

As we have seen, previous solutions to the inverse problem posed by the large amount of data generated by this earthquake have incorporated mathematical idealizations of many forms. Ultimately, however, the transfer function which models the effect of the real earth is not well known even over the short distances characteristic of the near-field. The ideal near-field transfer function would be one that could adequately take into consideration the effects of a layered half-space composed of material not necessarily perfectly elastic and perhaps not even isotropic. It would also allow explicit consideration of geometric inhomogeneities of a fairly extreme nature such as surface topography and material differences across a dipping fault surface.

The medium transfer function used in all the above dynamic near-field studies, that of Haskell (1969) and Maruyama (1963), may be improved in a more modest fashion, however, by generalizing it to include explicitly the effects of the ground surface. This is done in Chapter 2 where the displacements at the surface due to line forces and dislocations are formulated exactly. This work, which was carried out by Dr. Lane Johnson preparatory to his more general three-dimensional formulation (Johnson, 1974) of the same problem, will allow the straightforward inclusion of Rayleigh waves in the model interpretation of the recorded data as well as one body wave phase whose existence depends on the surface--a wave that leaves the source as an S-wave and is reflected along the surface as a P-wave. The two-dimensional nature of the formulation of Chapter 2 requires that the data considered be close enough to

the source that this source may be treated as two-dimensional. That is, the station must be close enough to the source so that the distance between source and receiver is small relative to the dimension of the source. This requirement is fulfilled by the position of Pacoima Dam relative to the zone of energy release of the San Fernando earthquake and so it is these records that are used as the observational basis for comparison with generated model accelerograms.

In Chapter 3 those additional parameters necessary to the generation of a model accelerogram are considered. They include the instrument response of the accelerometer through which the ground motion is recorded, the time history of the source at any point on the model fault surface, the geometry of some two-dimensional fault relative to the location on the surface at which acceleration is to be evaluated, the fault rupture propagation velocity, and the amplitude of the final displacements of the sides of the fault relative to each other as a function of position along the fault. As we shall see in Chapter 3 it is necessary to consider ground motions at frequencies high relative to the rise time of the source time history in order to have any opportunity to distinguish the functional smoothness of this time history. From previous work we have seen that derived rise times of approximately 0.5 seconds are commonly found so that, by the above contention, ground motions of 2 Hertz or higher frequency must be considered. Such high frequencies are most characteristic of accelerometer records and this is one reason why these records are chosen as the data base rather than their velocity or displacement equivalents which may be derived from them. This study is the first quantitative attempt to explain an actual observed accelerometer record. With the exceptions of basic review in sections 3.2 and 3.5 all

work in Chapter 3 is original as is the work in succeeding chapters.

In Chapter 4 the results of the previous two chapters are combined to allow the generation of a series of model accelerograms which may then be compared with the recorded accelerations of the Pacoima Dam strong-motion site. The degree and manner of the success or failure of such model accelerograms to match the observations are used to draw inferences about the faulting process of the San Fernando earthquake.

Finally, in Chapter 5 conclusions are drawn and areas for further exploration briefly mentioned.

Chapter 2

The Green's Functions of the Problem

2.1 Some Basic Considerations

Consider the general linear differential equation

$$Ly(x) = f(x)$$

where L is a known linear differential operator, $f(x)$ is some known function and $y(x)$ is to be determined. The inverse of a differential operator is an integral operator which we may symbolize by

$$L^{-1}f(x) = \int G(x,\xi)f(\xi)d\xi$$

provided that the kernal $G(x,\xi)$ can be chosen so that

$$LL^{-1}f(x) = f(x) \quad .$$

Thus we wish

$$LL^{-1}f(x) = L\int G(x,\xi)f(\xi)d\xi = \int [LG(x,\xi)]f(\xi)d\xi = f(x) \quad .$$

This condition can be easily fulfilled if

$$LG(x,\xi) = \delta(x-\xi) \qquad 2.1\text{-}1$$

where $\delta(x-\xi)$ is the Dirac delta function defined such that

$$\delta(x-\xi) = \begin{cases} 0, & x \neq \xi \\ \infty, & x = \xi \end{cases}$$

and

$$\int \delta(x-\xi)f(\xi)d\xi = f(x)$$

over any interval that includes x. When $G(x,\xi)$ has been found (where $G(x,\xi)$ is the general solution to 2.1-1) the solution to the original equation is

$$y(x) = L^{-1}Ly(x) = L^{-1}f(x) = \int G(x,\xi)f(\xi)d\xi \quad .$$

The particular kernal with this property is known as the Green's function for the general linear differential operator L.

For the problem to be attempted here the linear differential

operator of interest is that appropriate to the equation of motion for a homogeneous, isotropic, perfectly elastic solid. Initially, however, the more general case of an inhomogeneous, anisotropic elastic solid will be considered. The equation of motion then is (using the standard notation as in Burridge and Knopoff, 1964)

$$[C_{ijpq}(\vec{x})\ u_{p,q}(\vec{x},t)]_{,j} - \rho(\vec{x})\ \ddot{u}_i(\vec{x},t) = -f_i(\vec{x},t) \qquad 2.1\text{-}2$$

where

$\vec{x} = x_1\hat{x}_1 + x_2\hat{x}_2 + x_3\hat{x}_3$ is the Cartesian position vector,

$u_i(\vec{x},t)$ is the ith component of displacement at $\vec{x}$ and at time t,

$f_i(\vec{x},t)$ is the ith component of the body force at $\vec{x}$ and t,

$C_{ijpq}(\vec{x})$ are the elastic constants of the medium, and

$$u_{p,q}(\vec{x},t) = \frac{\partial}{\partial x_q}\, u_p(\vec{x},t) \quad ,$$

$$\ddot{u}_i(\vec{x},t) = \frac{\partial}{\partial t^2}\, u_i(\vec{x},t) \quad .$$

The summation convention is in effect so all repeated indices are to be summed from 1 to 3. It may be shown from conservation principles that even in the most general elastic solid

$$C_{ijpq} = C_{jipq} = C_{pqij} \quad . \qquad 2.1\text{-}3$$

Now let $v_i(\vec{x},t)$ be another motion due to a body force $g_i(\vec{x},t)$. Then in an inhomogeneous, anisotropic elastic solid we may write

$$[C_{ijpq}(\vec{x})v_{p,q}(\vec{x},t)]_{,j} - \rho(\vec{x})\ddot{v}_i(\vec{x},t) = -\ g_i(\vec{x},t) \qquad 2.1\text{-}4$$

These equations (2.1-2 and 2.1-4) are satisfied within a volume V bounded by the surface S for all time.

Next we wish to require that $f_i(\vec{x},t)$ and $g_i(\vec{x},t)$ vanish for some time $t < -T$ where T is a constant. Then from the principle of causality

$v_i(\vec{x},t)$ and $u_i(\vec{x},t)$ must also vanish for $t < -T$. In 2.1-4 replace t by $-t$ so that

$$[C_{ijpq}(\vec{x})v_{p,q}(\vec{x},t)]_{,j} - \rho(\vec{x})\ddot{v}(\vec{x},t) = -\bar{g}_i(\vec{x},t) \qquad 2.1\text{-}5$$

where

$$\bar{v}_i(\vec{x},t) = v_i(\vec{x},-t)$$

$$\bar{g}_i(\vec{x},t) = g_i(\vec{x},-t)$$

and $\bar{g}_i(\vec{x},t) = \bar{v}_i(\vec{x},t) = 0$ for $t > T$.

We now multiply 2.1-2 by $v_i(\vec{x},t)$ and 2.1-5 by $u_i(\vec{x},t)$, subtract the products and integrate over the volume V for all time t.

$$-\int_{-\infty}^{\infty} dt \int_V \{[C_{ijpq}\, u_{p,q}]_{,j}\, \bar{v}_i - [C_{ijpq}\, \bar{v}_{p,q}]_{,j}\, u_i - [\rho\ddot{u}_i\bar{v}_i - \rho\ddot{\bar{v}}_i u_i]\}dV =$$

$$-\int_{-\infty}^{\infty} dt \int_V [u_i\bar{g}_i - \bar{v}_i f_i]dV \qquad 2.1\text{-}6$$

We may immediately dispose of the second term on the left of equation 2.1-6 since

$$-\int_{-\infty}^{\infty} dt \int_V [\rho\ddot{u}_i\bar{v}_i - \rho\ddot{\bar{v}}_i u_i]dV =$$

$$-\int_{-\infty}^{\infty} dt \int_V \rho \frac{\partial}{\partial t}[\dot{u}_i\bar{v}_i - \dot{\bar{v}}_i u_i]dV =$$

$$\int_V \rho[\dot{u}_i\bar{v}_i - \dot{\bar{v}}_i u_i]dV \Big|_{t=-\infty}^{t=\infty}$$

But u_i vanishes for $t < -T$, and $\bar{v}_i$ vanishes for $t > T$ so the integrand is identically zero.

Next using the expressions

$$[C_{ijpq}\, u_{p,q}]_{,j}\, \bar{v}_i = [C_{ijpq}\, u_{p,q}\, \bar{v}_i]_{,j} - [C_{ijpq}\, u_{p,q}]\, \bar{v}_{i,j}$$

and similarly

$$[C_{ijpq}\,\bar{v}_{p,q}]_{,j}\,u_i = [C_{ijpq}\,\bar{v}_{p,q}\,u_i]_{,j} - [C_{ijpq}\,\bar{v}_{p,q}]u_{i,j}$$

We may write the first term in 2.1-6 as

$$-\int_{-\infty}^{\infty}dt\int_V\{[C_{ijpq}u_{p,q}]_{,j}\,\bar{v}_i - [C_{ijpq}\,\bar{v}_{p,q}]_{,j}\,u_i\}dV =$$

$$-\int_{-\infty}^{\infty}dt\int_V\{[\bar{v}_iC_{ijpq}u_{p,q} - u_iC_{ijpq}\bar{v}_{p,q}]_{,j} -$$

$$C_{ijpq}[\bar{v}_{i,j}u_{p,q} - u_{i,j}\bar{v}_{p,q}]\}dV \qquad 2.1\text{-}7$$

The last term of this expression vanishes because $C_{ijpq} = C_{pqij}$ as indicated in equation 2.1-3. That is, since ij and pq are repeated and therefore dummy indices under the summation convention, they may be interchanged at will so that

$$C_{ijpq}\bar{v}_{i,j}u_{p,q} - C_{ijpq}\bar{v}_{p,q}u_{i,j} =$$

$$C_{ijpq}\bar{v}_{i,j}u_{p,q} - C_{pqij}\bar{v}_{i,j}u_{p,q} =$$

$$C_{ijpq}\bar{v}_{i,j}u_{p,q} - C_{ijpq}\bar{v}_{i,j}u_{p,q} = 0 \qquad 2.1\text{-}8$$

From these considerations and from equations 2.1-6 and 2.1-7 we have

$$-\int_{-\infty}^{\infty}dt\int_V\{[\bar{v}_i\,C_{ijpq}u_{p,q} - u_iC_{ijpq}\bar{v}_{p,q}]_{,j}\}dV$$

$$= -\int_{-\infty}^{\infty}dt\int_V[u_i\bar{g}_i - \bar{v}_if_i]dV \qquad 2.1\text{-}9$$

We may now use the divergence theorem on the left side of this expression to derive

$$-\int_{-\infty}^{\infty}dt\int_S n_j[\bar{v}_iC_{ijpq}u_{p,q} - u_iC_{ijpq}\bar{v}_{p,q}]dS$$

$$= -\int_{-\infty}^{\infty}dt\int_V[u_i\bar{g}_i - \bar{v}_if_i]dV \qquad 2.1\text{-}10$$

In this expression n_j is the outward pointing normal to the surface S. Equation 2.1-9 is a form of the reciprocity theorem of Betti and Rayleigh.

We may now show how to solve for u_i in terms of its Green's function. As suggested by equation 2.1-1 let

$$\bar{g}_i(x,t) = \delta_{ni}\,\delta(\vec{x}-\vec{x}')\,\delta(t-t') \qquad 2.1\text{-}11$$

where δ_{ni} is the Kronecker delta

$$\delta_{ni} = \begin{cases} 0, & i \neq n \\ 1, & i = n \end{cases}$$

Substituting into equation 2.1-10 and integrating we have

$$u_n(\vec{x}',t') = -\int_{-\infty}^{\infty} dt \int_V G_{in}(\vec{x},-t;\vec{x}',-t') f_i(\vec{x},t)\,dV$$

$$+ -\int_{-\infty}^{\infty} dt \int_S n_j \{G_{in}(\vec{x},-t;\vec{x}',-t') C_{ijpq}(\vec{x}) u_{p,q}(\vec{x},t)$$

$$- u_i(\vec{x},t) C_{ijpq}(\vec{x}) G_{pn,q}(\vec{x},-t;\vec{x}',-t')\}\,dS \qquad 2.1\text{-}12$$

In this expression we have written G_{in} instead of v_i to symbolize the solution to equation 2.1-4 with $\bar{g}_i$ defined as in equation 2.1-11. This is in conformity to the notation of equation 2.1-1. $G_{in}(\vec{x},t;\vec{x}',t')$ is the displacement in the i direction at $(\vec{x},t)$ due to an impulsive point force in the n direction at $(\vec{x}',t')$. If in equation 2.1-12 u_i and G_{in} satisfy the same homogeneous boundary conditions on S and if we require f_i to be an impulsive point force we may derive the general form for the Green's function reciprocity theorem for the differential equation 2.1-2

$$G_{ij}(\vec{x},t;\vec{x}',t') = G_{ji}(\vec{x}',-t';\vec{x},-t) \qquad 2.1\text{-}13$$

Interchanging the variables $\vec{x}$ with $\vec{x}'$ and t with t' and using equation 2.1-13 we may write equation 2.1-12 as

$$u_n(\vec{x},t) = -\int_{-\infty}^{\infty} dt' \int_V G_{ni}(\vec{x},t;\vec{x}',t') f_i(\vec{x}',t')\,dV'$$

$$+ -\int_{-\infty}^{\infty} dt' \int_S n_j \{G_{ni}(\vec{x},t;\vec{x}',t') C_{ijpq}(\vec{x}') u_{p,q}(\vec{x}',t')$$

$$- u_i(\vec{x}',t') C_{ijpq}(\vec{x}') G_{np,q}(\vec{x},t;\vec{x}',t')\}\,dS' \qquad 2.1\text{-}14$$

where integration is now with respect to the primed variables and where

$$G_{np,q}(\vec{x},t;\vec{x}',t') = \frac{\partial}{\partial x'_q} G_{np}(\vec{x},t;\vec{x}',t')$$

Of course the summation convention still applies. Equation 2.1-14 is the generalized representation theorem of de Hoop and Knopoff. This expression will give us the displacements at any point $\vec{x}$ at time t due to forces within or at the boundary of volume V'.

Let us now find u_i for prescribed discontinuities in the displacement and its derivatives across a surface Σ embedded in V. Let ν_j be the unit normal to Σ and let $[u_i(\vec{x}',t')]$ and $[u_{p,q}(\vec{x}',t')]$ be the discontinuities in u_i and $u_{p,q}$ across Σ. Assume u_i and G_{ni} to satisfy the same homogeneous boundary conditions on S and apply equation 2.1-14 to the region bounded internally by Σ and externally by S. G_{ni} does not have prescribed discontinuities on Σ. Then the surface integrals over S are replaced by integrals over Σ only. Let us further require that there be no body forces in V and no stress discontinuities across Σ so that

$$f_i(\vec{x}',t') = 0 \quad \text{for } \vec{x}' \text{ in V, and}$$

$$[u_{p,q}(\vec{x}',t')] = 0 \quad \text{for } \vec{x}' \text{ on } \Sigma$$

Equation 2.1-14 now becomes

$$u_n(\vec{x},t) = -\int_{-\infty}^{\infty} dt' \int_{\Sigma} \nu_j \{[u_i(\vec{x}',t')] C_{ijpq}(\vec{x}') \cdot G_{np,q}(\vec{x},t;\vec{x}',t')\} d\Sigma' \qquad 2.1\text{-}15$$

where $\vec{x}'$ is made to conform to the dislocation surface Σ and the spatial integration is over this surface. It is obvious that to proceed further we will need the solution for the Green's functions themselves, or more specifically for the purposes of evaluating equation 2.1-15, we will need the spatial derivatives of the Green's functions. These will be found below.

2.2 The Green's Functions

Let us consider a line source buried in a half space as shown in

Figure 2.2(1). Let us further restrict the forces acting along this line to be in a direction perpendicular to this buried line source. If, as in Figure 2.2(1) the line is oriented in the $\hat{y}$ direction at $x' = 0$ and at a depth h below the surface of the half space the forces are constrained to act in the xz plane.

Then from the conservation of linear momentum and assuming that the half space is homogeneous, isotropic, and perfectly elastic we may write

$$\rho \frac{\partial^2}{\partial t^2} \vec{u}(x,z,t) = \vec{f}(x,z,t) + \mu\vec{\nabla}^2\vec{u}(x,z,t) + (\lambda+\mu)\vec{\nabla}(\vec{\nabla}\cdot u(x,z,t)) \qquad 2.2\text{-}1$$

where

$\vec{u}(x,z,t) = v(x,a,t)\ \hat{x} + W(x,z,t)\hat{z}$,

$\vec{f}(x,z,t) = [e(t)\hat{x} + g(t)\hat{z}]\delta(x)\delta(z-h)$,

ρ is the density of the medium,

μ and λ are Lame's elastic constants,

$\vec{\nabla}^2$ is the Laplacian operator,

$\vec{\nabla}$ is the gradient operator, and

$\vec{\nabla}\cdot$ is the divergence operator.

Carrying out the operations in equation 2.2-1 and resolving into components we may write a matrix equation of the form

$$\underline{A}\underline{x} = \underline{b}$$

where

$$\underline{A} = \begin{vmatrix} \{(\lambda+2\mu)\frac{\partial^2}{\partial x^2} + \mu\frac{\partial^2}{\partial z^2} - \rho\frac{\partial^2}{\partial t^2}\} & \{(\lambda+\mu)\frac{\partial^2}{\partial x \partial z} \\ \{(\lambda+\mu)\frac{\partial^2}{\partial x \partial z}\} & \{(\lambda+2\mu)\frac{\partial^2}{\partial z^2} + \mu\frac{\partial^2}{\partial x^2} - \rho\frac{\partial^2}{\partial t^2}\} \end{vmatrix}$$

$$\underline{x} = \begin{vmatrix} v(x,z,t) \\ w(x,z,t) \end{vmatrix} \quad ; \quad \underline{b} = \begin{vmatrix} -e(t)\ \delta(x)\ \delta(z-h) \\ -g(t)\ \delta(x)\ \delta(z-h) \end{vmatrix}$$

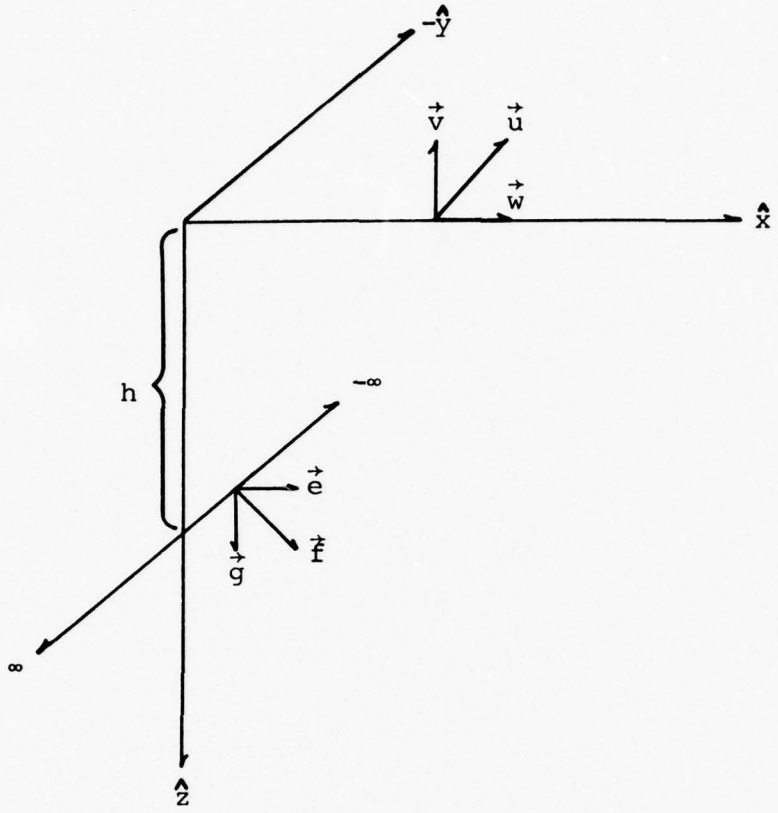


Fig 2.2(1) The geometry of the problem

Now let us take the Laplace transform of this matrix equation in the order $t \to s$, $x \to \xi$, and $z \to \zeta$. The Laplace transform with respect to t is the ordinary one-sided Laplace transform while those with respect to x and z are the generalized two-sided Laplace transforms. In later development we will require s to be real and positive. With this requirement the remaining two transform variables must be restricted as outlined below in order to assure convergence of the transform integrals.

If s is real and positive with

$$\alpha = \left[\frac{\lambda+2\mu}{\rho}\right]^{1/2} \quad ; \quad \beta = \left[\frac{\mu}{\rho}\right]^{1/2}$$

$$K_\alpha = \frac{s}{\alpha} \quad ; \quad K_\beta = \frac{s}{\beta}$$

then in taking the $x \to \xi$ transform we find that we must have

$$|\mathrm{Re}\{\xi\}| \leq \text{minimum } (K_\alpha, K_\beta)$$

where $|\mathrm{Re}\{\xi\}|$ is the absolute value of the real part of ξ. If we further define

$$\nu_\alpha = [K_\alpha^2 - \xi^2]^{1/2} \quad ; \quad \nu_\beta = [K_\beta^2 - \xi^2]^{1/2}$$

we see that the above restriction on ξ requires that

$$\mathrm{Re}\{\nu_\alpha\} \geq 0 \quad ; \quad \mathrm{Re}\{\nu_\beta\} \geq 0$$

Then in taking the $z \to \zeta$ transform we must require that

$$|\mathrm{Re}\{\zeta\}| \leq \text{minimum } [\mathrm{Re}\{\nu_\alpha\}, \mathrm{Re}\{\nu_\beta\}]$$

When the transforms have been taken under the above conditions and in the given order we know that the Laplace transform of A exists and we may write

$$\underline{\tilde{A}}\,\underline{\tilde{x}} = \underline{\tilde{b}} \qquad 2.2\text{-}2$$

where $\underline{\tilde{A}} = \mathcal{L}\{\underline{A}\}$ and similarly for the other terms and where

$$\underset{\sim}{A} = \begin{vmatrix} \{(\lambda+2\mu)\xi^2 + \mu\zeta^2 - \rho s^2\} & (\lambda+\mu)\xi\zeta \\ (\lambda+\mu)\zeta\xi & \{(\lambda+2\mu)\zeta^2 + \mu\xi^2 - \rho s^2\} \end{vmatrix}$$

$$\underset{\sim}{x} = \begin{vmatrix} V(\xi,\zeta,s) \\ W(\xi,\zeta,s) \end{vmatrix} \quad ; \quad \underset{\sim}{b} = \begin{vmatrix} -E(s)e^{-\zeta h} \\ -G(s)e^{-\zeta h} \end{vmatrix}$$

where $E(s) = \mathcal{L}\{e(t)\} = \int_0^\infty e(t)e^{-st}dt$ and similarly for V, W, and G.

From elementary matrix theory it may be shown that the system of algebraic equations symbolized by the matrix equation 2.2-2 may be solved if the determinant of the 2x2 coefficient matrix $\underset{\sim}{A}$ is not zero. That is

$$\underset{\sim}{x} = \underset{\sim}{A}^{-1}\underset{\sim}{b} \qquad 2.2\text{-}3$$

where, from equation 2.2-2

$$\underset{\sim}{A}^{-1} = \frac{1}{D} \begin{vmatrix} \{\mu\xi^2 + (\lambda+2\mu)\zeta^2 - \rho s^2\} & -(\lambda+\mu)\xi\zeta \\ -(\lambda+\mu)\xi\zeta & \{(\lambda+2\mu)\xi^2 + \mu\zeta^2 - \rho s^2\} \end{vmatrix} \qquad 2.2\text{-}4$$

Here D is the determinant of the matrix $\underset{\sim}{A}$ and may be written

$$D = [(\lambda+2\mu)\xi^2 + \mu\zeta^2 - \rho s^2][(\lambda+2\mu)\zeta^2 + \mu\xi^2 - \rho s^2] - [(\lambda+\mu)\zeta\xi]^2$$

We wish to write this in such a way that it will be meaningful when the inverse Laplace transform of the variable ζ is taken. With some algebraic manipulation D may be rewritten as

$$D = \mu(\lambda+2\mu)[(\zeta^2 - \nu_\alpha^2)(\zeta^2 - \nu_\beta^2)] \qquad 2.2\text{-}5$$

We have now solved the problem in the transform domain. It is now necessary to return to the real domain.

2.21 The $\zeta \to z$ Inverse Transform and Boundary Conditions

Let us consider the $V(\xi,\zeta,s)$ term of the matrix equation 2.2-3. This may be written out as

$$V(\xi,\zeta,s) = \frac{1}{D}\{(\mu\xi^2 + (\lambda+2\mu)\zeta^2 - \rho s^2)(-E(s)e^{-\zeta h}) + (\lambda+\mu)\xi\zeta G(s)e^{-\zeta h}\} \qquad 2.2\text{-}6$$

Then since

$$L^{-1}[F(\zeta)] = f(z) = \frac{1}{2\pi i}\int_{-i\infty}^{i\infty} F(\zeta)e^{\zeta z}d\zeta$$

we have from equation 2.2-6

$$V(\zeta,z,s) = \frac{1}{2\pi i}\int_{-i\infty}^{i\infty}[\frac{1}{D}\{(\mu\xi^2+(\lambda+2\mu)\zeta^2-\rho s^2)(-E(s))$$

$$+ (\lambda+\mu)\xi\zeta G(s)\}e^{-\zeta(h-z)}]d\zeta \qquad 2.2\text{-}7$$

From this expression it is seen how intimately the determinant controls our problem since it specifies the poles whose residues determine the value of this integral. From equation 2.2-5 it is clear that the integrand of equation 2.2-7 has simple poles at

$$\zeta = \pm \nu_\alpha \quad ; \quad \zeta = \pm \nu_\beta$$

There are two cases to consider. For $z<h$ we have $h-z>0$ and for $z>h$ we have $h-z<0$. Thus for the integral to exist in equation 2.2-7 we must close the contour in the right half plane of ζ space for $z<h$. This implies residues from the poles at ν_α and ν_β. Note that this contour is closed clockwise so that an additional minus sign is necessary. For $z>h$ we close the contour in the left half plane picking up the residues from the poles at $-\nu_\alpha$ and $-\nu_\beta$. These two cases are shown in Figure 2.2(2).

For $z<h$ we have the two residues

$$\text{Res}[\zeta=\nu_\alpha] = C_1[\xi^2E(s)+\xi\nu_\alpha G(s)]\frac{e^{-\nu_\alpha(h-z)}}{\nu_\alpha} \qquad 2.2\text{-}8$$

where C_1 is a constant such that

$$C_1 = \frac{(\lambda+\mu)}{2\mu(\lambda+2\mu)}\,(K_\alpha^2-K_\beta^2)^{-1}$$

Similarly

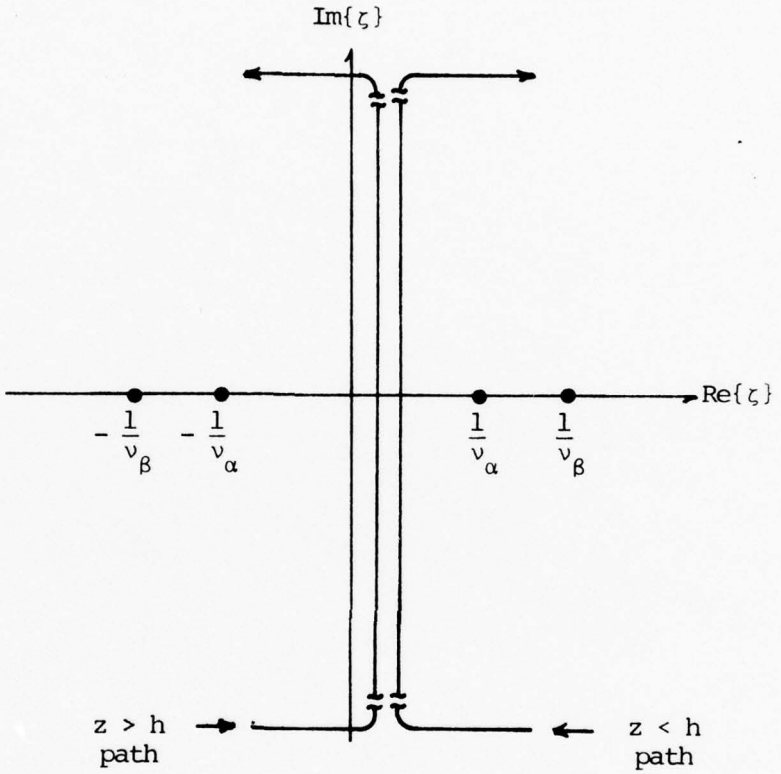


Fig. 2.2(2) Contours for the evaluation of the $\zeta \to z$ inverse transform for the two cases $z<h$ and $z>h$.

$$\text{Res}[\zeta=\nu_\beta] = -C_1[\nu_\beta^2 E(s)-\xi\nu_\beta G(s)]\frac{e^{-\nu_\beta(h-z)}}{\nu_\beta} \qquad 2.2\text{-}9$$

From equations 2.2-7, 2.2-8, and 2.2-9 we have

$$V(\xi,z,s) = \frac{1}{2\pi i}(-2\pi i)\{\text{Res}[\zeta=\nu_\alpha] + \text{Res}[\zeta=\nu_\beta]\}$$

or

$$V(\xi,z,s) = C_1\{(\xi^2 E(s)+\xi\nu_\alpha G(s))\frac{e^{-\nu_\alpha(h-z)}}{\nu_\alpha}$$

$$+ (\nu_\beta^2 E(s)-\xi\nu_\beta G(s))\frac{e^{-\nu_\beta(h-z)}}{\nu_\beta}\}, \quad z<h \qquad 2.2\text{-}10$$

This is one quarter of the complete solution in (ξ,z,s) space. Now we wish to find $W(\xi,z,s)$ for $z<h$, and $V(\xi,z,s)$, $W(\xi,z,s)$ for $z>h$. The essentials of the derivation of these quantities are the same as those used above. Therefore, we write without proof the whole solution below. In this matrix equation

$$\text{sgn}(h-z) = \begin{cases} 1, & h>z \\ -1, & h<z \end{cases}$$

$$\begin{vmatrix} V(\xi,z,s) \\ W(\xi,z,s) \end{vmatrix} = C_1\left[\begin{vmatrix} \xi^2 & \xi\nu_\alpha \text{sgn}(h-z) \\ \xi\nu_\alpha \text{sgn}(h-z) & \nu_\alpha^2 \end{vmatrix} \begin{vmatrix} \frac{e^{-\nu_\alpha|h-z|}}{\nu_\alpha} \end{vmatrix}\right.$$

$$\left. + \begin{vmatrix} \nu_\beta^2 & -\xi\nu_\beta \text{sgn}(h-z) \\ -\xi\nu_\beta \text{sgn}(h-z) & \xi^2 \end{vmatrix} \begin{vmatrix} \frac{e^{-\nu_\beta|h-z|}}{\nu_\beta} \end{vmatrix}\right] \begin{vmatrix} E(s) \\ G(s) \end{vmatrix} \qquad 2.2\text{-}11$$

Having solved for this particular solution we wish to find the complimentary solution to the homogeneous equivalent to equation 2.2-2 in (ξ,z,s) space. That is, we wish to find the solution to the set of equations

$$\begin{vmatrix} \{(\lambda+2\mu)\xi^2 + \mu\frac{\partial^2}{\partial z^2} - \rho s^2\} & (\lambda+\mu)\xi\frac{\partial}{\partial z} \\ (\lambda+\mu)\xi\frac{\partial}{\partial z} & \{(\lambda+2\mu)\frac{\partial^2}{\partial z^2} + \mu\xi^2 - \rho s^2\} \end{vmatrix} \begin{vmatrix} V(\xi,z,s) \\ W(\xi,z,s) \end{vmatrix} = \begin{vmatrix} 0 \\ 0 \end{vmatrix} \qquad 2.2\text{-}12$$

These equations may be shown to have solutions which remain finite as z approaches $+\infty$ of the form

$$V(\xi,z,s) = A\xi e^{-\nu_\alpha z} + B\nu_\beta e^{-\nu_\beta z}$$

$$W(\xi,z,s) = -A\nu_\alpha e^{-\nu_\alpha z} + B\xi e^{-\nu_\beta z} \qquad 2.2\text{-}13$$

That these are the only nontrivial solutions to equation 2.2-12 may be seen from direct substitution. A and B are constants in the sense that they are independent of z. Otherwise A and B are not restricted. Later algebra will be greatly simplified if we write

$$A \equiv C_1[A_e E(s) + A_g G(s)]\frac{e^{-\nu_\alpha h}}{\nu_\alpha}$$

$$B \equiv C_1[B_e E(s) + B_g G(s)]\frac{e^{-\nu_\beta h}}{\nu_\beta}$$

Then the general solution to the problem may be written in matrix form as

$$\begin{vmatrix} V(\xi,z,s) \\ W(\xi,z,s) \end{vmatrix} = C_1\left[\begin{vmatrix} \xi^2 & \xi\nu_\alpha \mathrm{sgn}(h-z) \\ \xi\nu_\alpha \mathrm{sgn}(h-z) & \nu_\alpha^2 \end{vmatrix}\frac{e^{-\nu_\alpha|h-z|}}{\nu_\alpha} + \right.$$

$$\begin{vmatrix} \xi A_e & \xi A_g \\ -\nu_\alpha A_e & -\nu_\alpha A_g \end{vmatrix}\frac{e^{-\nu_\alpha(h+z)}}{\nu_\alpha} + \begin{vmatrix} \nu_\beta^2 & -\xi\nu_\beta \mathrm{sgn}(h-z) \\ -\xi\mu_\beta \mathrm{sgn}(h-z) & \xi^2 \end{vmatrix}\frac{e^{-\nu_\beta|h-z|}}{\nu_\beta} +$$

$$\left.\begin{vmatrix} \nu_\beta B_e & \nu_\beta B_g \\ \xi B_e & \xi B_g \end{vmatrix}\frac{e^{-\nu_\beta(h+z)}}{\nu_\beta}\right]\begin{vmatrix} E(s) \\ G(s) \end{vmatrix} \qquad 2.2\text{-}14$$

where A_e, B_e, A_g, and B_g are constants in the same sense as A and B and must be determined from boundary conditions. Since the solution is now in (ξ,z,s) space let us briefly examine boundary conditions in this space.

As is usually done, let the stress on a surface whose normal is in the i direction due to a force in the j direction be τ_{ij}. Thus, if we wish to specify the stresses along a surface of constant z (or one whose normal is in the z direction) we need to find τ_{zx}, τ_{zy}, and τ_{zz}.

Let us further define the strain, e_{ij}, as that strain in the i direction due to a displacement in the j direction. Then, for the type of medium under consideration it may be shown that

$$e_{ij} = \frac{1}{2}\left(\frac{\partial u_i}{\partial x_j} + \frac{\partial u_j}{\partial x_i}\right)$$

where, as before, u_i is the displacement in the i direction. Then

$$\tau_{ij} = \lambda\delta_{ij}\theta + 2\mu e_{ij} \qquad 2.2\text{-}15$$

where $\theta = e_{kk} = e_{11} + e_{22} + e_{33}$ and δ_{ij} is the Kronecker delta as previously defined. In previous notation $u_1 = u(x,z,t)$ and $u_3 = w(s,z,t)$. Then

$$e_{xx} = \frac{\partial}{\partial x}u(x,z,t) \quad , \quad e_{yy} = 0 = e_{zy} \quad , \quad e_{zz} = \frac{\partial}{\partial z}w(x,z,t)$$

$$e_{zx} = \frac{1}{2}\left(\frac{\partial}{\partial z}u(x,z,t) + \frac{\partial}{\partial x}w(s,z,t)\right)$$

and from equation 2.2-15

$$\tau_{zx} = \left(\frac{\partial}{\partial z}u(x,z,t) + \frac{\partial}{\partial x}w(s,z,t)\right)$$

$$\tau_{zy} = 0$$

$$\tau_{zz} = \lambda\frac{\partial}{\partial x}u(x,z,t) + (\lambda+2\mu)\frac{\partial}{\partial z}w(s,z,t)$$

Taking the Laplace transforms $t \to s$ and $x \to \xi$ as before we have

$$\begin{aligned}\bar{\tau}_{zx}(\xi,z,s) &= \mu\left(\frac{\partial}{\partial z} V(\xi,z,s) + \xi W(\xi,z,s)\right)\\ \bar{\tau}_{zz}(\xi,z,s) &= \lambda\xi V(\xi,z,s) + (\lambda+2\mu)\frac{\partial}{\partial z} W(\xi,z,s)\end{aligned} \qquad 2.2\text{-}16$$

Now we may explicitly write the boundary conditions. That is from equation 2.2-14

$$\begin{aligned}\frac{\partial}{\partial z} V(\xi,z,s)\Big|_{z=0} &= C_1\{[\xi(\xi-A_e)e^{-\nu_\alpha h} + \\ &\quad (\nu_\beta^2 - B_e\nu_\beta)e^{-\nu_\beta h}]E(s) + \\ &\quad [(\xi\mu_\alpha - \xi A_g)e^{-\nu_\alpha h} - \nu_\beta(\xi + B_g)e^{-\nu_\beta h}]G(s)\}\\ \frac{\partial}{\partial z} W(\xi,z,s)\Big|_{z=0} &= C_1\{[\nu_\alpha(\xi+A_e)e^{-\nu_\alpha h} - \\ &\quad \xi(\nu_\beta+B_e)e^{-\nu_\beta h}]E(s) + \\ &\quad [\nu_\alpha(\nu_\alpha+A_g)e^{-\nu_\alpha h} + \xi(\xi-B_g)e^{-\nu_\beta h}]G(s)\}\end{aligned}$$

From these expressions and similar ones for $V(\xi,z,s)\big|_{z=0}$ and $W(\xi,z,s)\big|_{z=0}$ we may write expressions for $\bar{\tau}_{zx}(\xi,o,s)$ and $\bar{\tau}_{zz}(\xi,o,s)$ and from these equations it will be possible to solve for the constants A_e, A_g, B_e, and B_g using the usual boundary conditions that the stresses vanish at z=0 for arbitrary E(s) and G(s). That is, from equations 2.2-16 and 2.2-17 we have

$$\begin{vmatrix}\bar{\tau}_{zx}(\xi,o,s)\\ \bar{\tau}_{zz}(\xi,o,s)\end{vmatrix} = C_1\left[\begin{vmatrix}2\xi(\xi-A_e) & 2\xi(\nu_\alpha-A_g)\\ \frac{1}{\nu_\alpha}(\nu_\beta^2-\xi^2)(\xi+A_e) & \frac{1}{\nu_\alpha}(\nu_\beta^2-\xi^2)(\nu_\alpha+A_g)\end{vmatrix} e^{-\nu_\alpha h} + \right.$$

$$\left.\begin{vmatrix}\frac{1}{\nu_\beta}(\nu_\beta^2-\xi^2)(\nu_\beta-B_e) - \frac{1}{\nu_\beta}(\nu_\beta^2-\xi^2)(\xi+B_g)\\ -2\xi(\nu_\beta+B_e) \qquad 2\xi(\xi-B_g)\end{vmatrix} e^{-\nu_\beta h}\right] \begin{vmatrix}E(s)\\ G(s)\end{vmatrix} \qquad 2.2\text{-}18$$

From equation 2.2-18 it is easily seen that for $\bar{\tau}_{zx}(\xi,o,s)$ and $\bar{\tau}_{zz}(\xi,o,s)$ to be zero for arbitrary E(s) and G(s) we must have the four conditions

$$2\xi(\xi-A_e)e^{-\nu_\alpha h} + \frac{1}{\nu_\beta}(\nu_\beta^2-\xi^2)(\nu_\beta-B_e)e^{-\nu_\beta h} = 0$$

$$\frac{1}{\nu_\beta}(\nu_\beta^2-\xi^2)(\xi+A_e)e^{-\nu_\alpha h} - 2\xi(\nu_\beta+B_e)e^{-\nu_\beta h} = 0$$

$$2\xi(\nu_\alpha-A_g)e^{-\nu_\alpha h} - \frac{1}{\nu_\beta}(\nu_\beta^2-\xi^2)(\xi+B_g)e^{-\nu_\beta h} = 0$$

$$\frac{1}{\nu_\alpha}(\nu_\beta^2-\xi^2)(\nu_\alpha+A_g)e^{-\nu_\alpha h} + 2\xi(\xi-B_g)e^{-\nu_\beta h} = 0$$

Solving these two sets of two simultaneous equations in two unknowns we find

$$A_e = -\frac{\xi}{R}\left[(\nu_\beta^2-\xi^2)^2 - 4\xi^2\nu_\alpha\nu_\beta - 4\nu_\alpha\nu_\beta(\nu_\beta^2-\xi^2)e^{(\nu_\alpha-\nu_\beta)h}\right]$$

$$B_e = \frac{\nu_\beta}{R}\left[(\nu_\beta^2-\xi^2)^2 - 4\xi^2\nu_\alpha\nu_\beta + 4\xi^2(\nu_\beta^2-\xi^2)e^{(\nu_\beta-\nu_\alpha)h}\right]$$

$$A_g = -\frac{\nu_\alpha}{R}\left[(\nu_\beta^2-\xi^2)^2 - 4\xi^2\nu_\alpha\nu_\beta + 4\xi^2(\nu_\beta^2-\xi^2)e^{(\nu_\alpha-\nu_\beta)h}\right]$$

$$B_g = -\frac{\xi}{R}\left[(\nu_\beta^2-\xi^2)^2 - 4\xi^2\nu_\alpha\nu_\beta - 4\nu_\alpha\nu_\beta(\nu_\beta^2-\xi^2)e^{(\nu_\beta-\nu_\alpha)h}\right]$$

where $R = (\nu_\beta^2-\xi^2)^2 + 4\xi^2\nu_\alpha\nu_\beta$.

We may now return to equation 2.2-14, set z=0 and substitute for A_e, A_g, B_e, and B_g to solve for the general solution at the surface in (ξ,z,s) space. That is, we have now solved for a line source in a half-space with the correct boundary condition in the transform space. From equation 2.2-14 and the above expressions we have

$$\begin{vmatrix} V(\xi,o,s) \\ W(\xi,o,s) \end{vmatrix} = -\frac{2K_\beta^2}{R} C_1 \left[\begin{vmatrix} 2\xi^2\nu_\beta & 2\xi\nu_\alpha\nu_\beta \\ \xi(\nu_\beta^2-\xi^2) & \nu_\alpha(\nu_\beta^2-\xi^2) \end{vmatrix} e^{-\nu_\alpha h} \right.$$

$$+ \begin{vmatrix} \nu_\beta(\nu_\beta^2-\xi^2) & -\xi(\nu_\beta^2-\xi^2) \\ -2\xi\nu_\alpha\nu_\beta & 2\xi^2\nu_\alpha \end{vmatrix} e^{-\nu_\beta h} \Bigg] \begin{vmatrix} E(s) \\ G(s) \end{vmatrix} \qquad 2.2\text{-}19$$

2.22 The $\xi \to x$ and $s \to t$ Inverse Transforms

In taking these last two inverse transforms we shall be using the method of Cagniard (1939) as modified by de Hoop (1960). This method involves the playing of a pair of inverse transforms against one another so that the evaluation of either of the inverse transforms becomes unnecessary. That is, we wish to manipulate two integrals in such a manner that we may find an expression that is recognized as the inverse transform of a transform so that

$$v(x,o,t) = \mathcal{L}^{-1}\{\mathcal{L}^{-1}\{V(\xi,o,s)\}_{\xi\to x}\}_{s\to t}$$

$$= \mathcal{L}^{-1}\{\mathcal{L}\{v(x,o,t)\}_{t\to s}\}_{s\to t}$$

Thus, it is necessary to find under what conditions

$$\mathcal{L}^{-1}\{V(\xi,o,s)\}_{\xi\to x} = \mathcal{L}\{v(x,o,t)\}_{t\to s} \qquad 2.2\text{-}20$$

If such conditions can be found the argument of the Laplace transform on the right hand side of equation 2.2-20 will be the desired answer.

To begin with, let us write the $\xi \to x$ inverse transform of equation 2.2-19 explicitly as

$$V(x,o,s) = \frac{1}{\mu 2\pi i}\int_{-i\infty}^{i\infty}\frac{1}{R}\{[2\xi^2\nu_\beta e^{-\nu_\alpha h} + \nu_\beta(\nu_\beta^2-\xi^2)e^{-\nu_\beta h}]E(s)$$

$$+ [2\xi\nu_\alpha\nu_\beta e^{-\nu_\alpha h} - \xi(\nu_\beta^2-\xi^2)e^{-\nu_\beta h}]G(s)\}e^{\xi x}d\xi$$

or

$$V(x,o,s) = \frac{1}{\mu 2\pi i}\int_{-i\infty}^{i\infty}\frac{1}{R}\{[2\xi^2\nu_\beta E(s)+2\xi\nu_\beta\nu_\alpha G(s)]e^{\xi x-\nu_\alpha h}$$

$$+ [\nu_\beta(\nu_\beta^2-\xi^2)E(s)-\xi(\nu_\beta^2-\xi^2)G(s)]e^{\xi x-\nu_\beta h}\}d\xi$$

where we have used the fact that $2K_\beta^2 C_1 = \frac{1}{\mu}$. Similarly

$$W(x,o,s) = \frac{1}{\mu 2\pi i}\int_{-i\infty}^{i\infty}\frac{1}{R}\{[\xi(\nu_\beta^2-\xi^2)E(s)+\nu_\alpha(\nu_\beta^2-\xi^2)G(s)]e^{\xi x-\nu_\alpha h}$$

$$- [2\xi\nu_\alpha\nu_\beta E(s)-2\xi^2\nu_\alpha G(s)]e^{\xi x-\nu_\beta h}\}d\xi$$

Let us now consider the problem in polar coordinates (r,θ) where $x = r\sin\theta$, $h = r\cos\theta$ and conversely $r = \sqrt{x^2+h^2}$, $\theta = \tan^{-1}(\frac{x}{h})$. Also let $\xi \equiv s\gamma$, $\nu_\alpha \equiv s\eta_\alpha$, and $\nu_\beta \equiv s\eta_\beta$ where from previous requirements on ν_α and ν_β we have

$$\eta_\alpha \equiv \sqrt{\frac{1}{\alpha^2} - \gamma^2} \quad , \quad \mathrm{Re}\{\eta_\alpha\} \geq 0$$

$$\eta_\beta \equiv \sqrt{\frac{1}{\beta^2} - \gamma^2} \quad , \quad \mathrm{Re}\{\eta_\beta\} \geq 0$$

Making these substitutions into the above expressions for V(x,o,s) and W(x,o,s) we have

$$V(x,o,s) = \frac{1}{\mu 2\pi i}\int_{-i\infty}^{i\infty}\frac{1}{R}\{[2\gamma^2\eta_\beta E(s)+2\gamma\eta_\alpha\eta_\beta G(s)]e^{s(\gamma x-\eta_\alpha h)}$$

$$+ [\eta_\beta(\eta_\beta^2-\gamma^2)E(s)-\gamma(\eta_\beta^2-\gamma^2)G(s)]e^{s(\gamma x-\eta_\beta h)}\}d\gamma$$

$$W(x,o,s) = \frac{1}{\mu 2\pi i}\int_{-i\infty}^{i\infty}\frac{1}{R}\{[\gamma(\eta_\beta^2-\gamma^2)E(s)+\eta_\alpha(\eta_\beta^2-\gamma^2)G(s)]e^{s(\gamma x-\eta_\alpha h)}$$

$$- [2\gamma\eta_\alpha\eta_\beta E(s)-2\gamma^2\eta_\alpha G(s)]e^{s(\gamma x-\eta_\beta h)}\}d\gamma \qquad 2.2\text{-}21$$

where now $R \equiv (\eta_\beta^2-\gamma^2)^2 + 4\gamma^2\eta_\alpha\eta_\beta$.

Let us now consider a contour with the following properties in the complex γ plane: this contour is symmetric about the real γ axis ($\mathrm{Im}\{\gamma\} = 0$) and one part of it is the line $\mathrm{Re}\{\gamma\} = C$ where C is a positive constant. Such a contour is shown in Figure 2.2(3). We know from Cauchy's Integral Theorem that if this contour encloses no singularities the total

contribution of an integral along this contour is identically zero. Furthermore, if all singularities are arbitrarily close to the real γ axis the contributions to the integral along the segments of the contour at $\gamma = \pm i\infty$ are also zero. Therefore, if s is real and positive and using the notation of Figure 2.2(3) we have from Cauchey's Integral Theorum

$$\int_{-i\infty}^{i\infty} V(s\gamma,o,s)e^{s\gamma x}d\gamma = \int_{\Gamma_1+\Gamma_1'} V(s\gamma,o,s)e^{s\gamma x}d$$

Finally, since on segment Γ_1 $\mathrm{Im}\{\gamma\} > 0$ and on Γ_1' $\mathrm{Im}\{\gamma\} < 0$, and since Γ_1 and Γ_1' are symmetric mirror images of each other across the $\mathrm{Im}\{\gamma\} = 0$ axis we have for any general function of γ, $f(\gamma)$

$$\int_{\Gamma_1+\Gamma_1'} f(\gamma)d\gamma = \int_{\Gamma_1} \{f(\gamma)+f^*(\gamma)\}d\gamma = 2i \int_{\Gamma_1} \mathrm{Im}\{f(\gamma)\}d\gamma$$

where $f^*(\gamma)$ is the complex conjugate of $f(\gamma)$. With these considerations we may alter equations 2.2-21 to read

$$V(x,o,s) = \frac{1}{\pi\mu}\int_0^{i\infty} \mathrm{Im}\{\frac{1}{R}\{[2\gamma^2\eta_\beta E(s)+2\gamma\eta_\alpha\eta_\beta G(s)]e^{s(\gamma x-\eta_\alpha h)}$$

$$+ [\eta_\beta(\eta_\beta^2-\gamma^2)E(s)-\gamma(\eta_\beta^2-\gamma^2)G(s)]e^{s(\gamma x-\eta_\beta h)}\}\}d\gamma$$

$$W(x,o,s) = \frac{1}{\pi\mu}\int_0^{i\infty} \mathrm{Im}\{\frac{1}{R}\{[\gamma(\eta_\beta^2-\gamma^2)E(s)$$

$$+ \eta_\alpha(\eta_\beta^2-\gamma^2)G(s)]e^{s(\gamma x-\eta_\alpha h)}$$

$$- [2\gamma\eta_\alpha\eta_\beta E(s)-2\gamma^2\eta_\alpha G(s)]e^{s(\gamma x-\eta_\beta h)}\}\}d\gamma \qquad 2.2\text{-}22$$

Since our general aim now is to make these integrals look like the forward Laplace transform $\mathcal{L}\{f(t)\}_{t\to s}$ let us define two new variables

$$\tau_\alpha = -\gamma_\alpha x + \eta_\alpha h$$

$$\tau_\beta = -\gamma_\beta x + \eta_\beta h$$

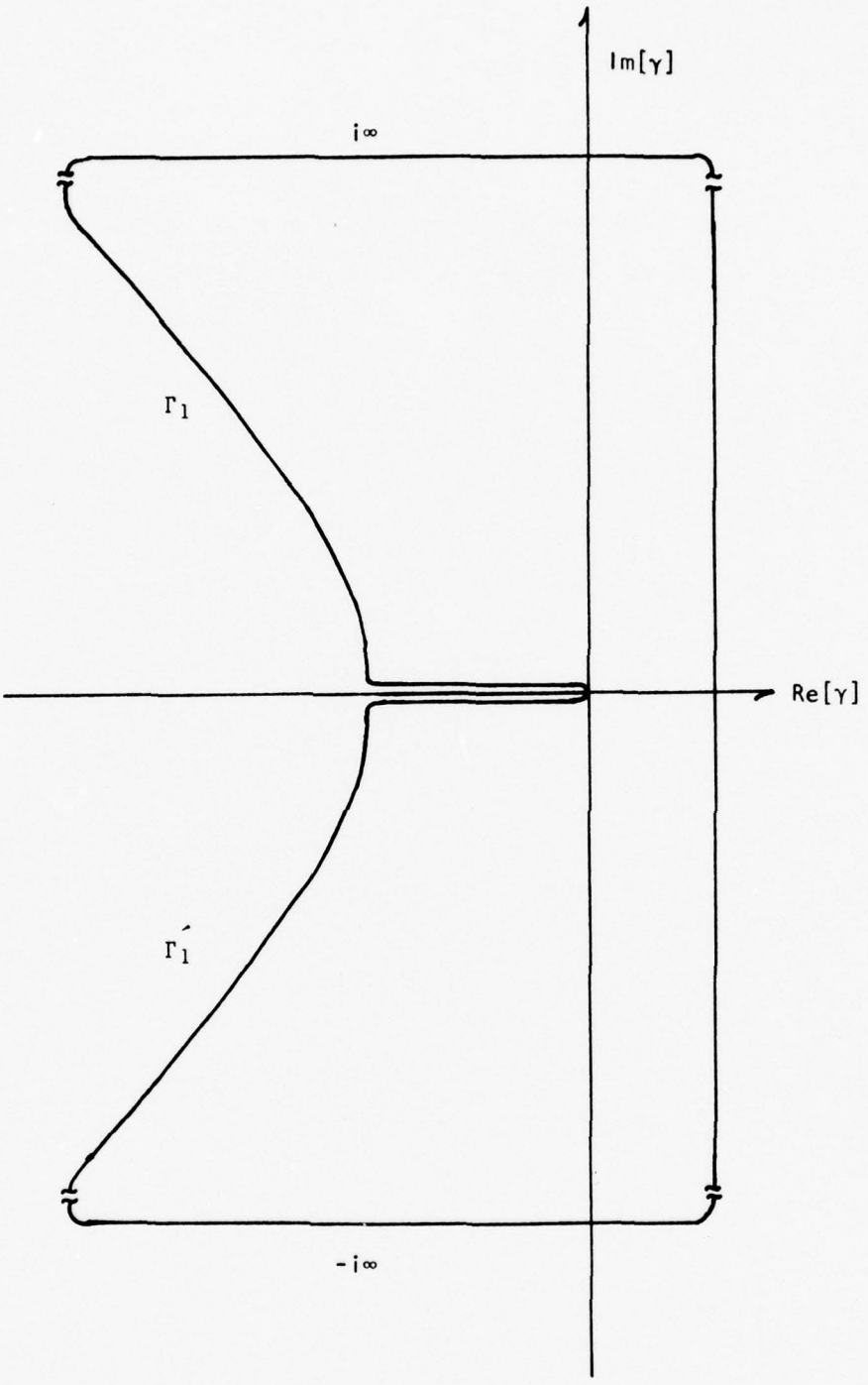


Fig. 2.2(3) Contour for the application of Cauchy's Integral Theorum to the $\xi \to x$ inverse transform integral representation.

or $\tau_c = -\gamma_c x + \eta_c h$ where c may be either α or β. If we now substitute for η_c in terms of γ and c and solve for γ we find

$$\gamma_c = -\frac{\tau_c \sin\theta}{r} + \sqrt{r^2/c^2 - \tau_c^2}\ \frac{\cos\theta}{r} \quad , \quad \tau_c^2 \leq \frac{r^2}{c^2}$$

$$\gamma_c = -\frac{\tau_c \sin\theta}{r} + i\sqrt{\tau_c^2 - r^2/c^2}\ \frac{\cos\theta}{r} \quad , \quad \tau_c^2 > \frac{r^2}{c^2} \qquad 2.2\text{-}23$$

And from these expressions, we may derive

$$d\gamma_c = \frac{-\eta_c}{\sqrt{r^2/c^2 - \tau_c^2}}\, d\tau_c \quad , \quad \tau_c^2 \leq \frac{r^2}{c^2}$$

$$d\gamma_c = \frac{i\eta_c}{\sqrt{\tau_c^2 - r^2/c^2}}\, d\tau_c \quad , \quad \tau_c^2 > \frac{r^2}{c^2} \qquad 2.2\text{-}24$$

We now come to the crux of the problem. It is wished to find a path of integration in the complex γ plane such that τ_α and τ_β will be positive and real for each term of the integrand of equation set 2.2-22. For example let us consider the term

$$V_1(x,o,s) = \frac{1}{\mu\pi} \int_0^{i\infty} Im\left\{\frac{2\gamma^2\eta_\beta E(s) + 2\gamma\eta_\alpha\eta_\beta G(s)}{R}\, e^{-s\tau_\alpha}\right\} d\gamma \qquad 2.2\text{-}25$$

The singularities of the integrand are of prime importance since we must be able to construct a contour segment that has the properties required of Γ_1 in Figure 2.2(3) and along which τ_c (τ_α in the case of the above expression) is real and positive. Specifically, this contour segment must be such as to enclose no singularities. In expressions such as the one above $\gamma \equiv \gamma_c$ where c is the velocity subscript of τ_c in the same expression. R, as noted above, is the Rayleigh's equation for this problem which entered naturally when we considered the free surface boundary conditions. Thus, it is easily shown that there are singularities at $\gamma = \pm 1/\alpha$ $\gamma = \pm 1/\beta$, and $\gamma = \pm 1/c_r$ where c_r is the solution to Rayleigh's equation. The first two sets of singularities are branch points while

the last set are simple poles. Since for a realizable elastic solid $\alpha > \beta > c_r$ we may draw the pertinent singularities as in Figure 2.2(4). The values used in this figure are α = 5.58 km/sec and β = 2.90 km/sec. A branch line is drawn between the two branch points - $1/\alpha$ and - $1/\beta$. It may be seen from equation 2.2-23 that for integrals involving τ_c such as equation 2.2-25 γ is real and negative for $\tau_c \leq r/c$ and will become complex beyond this point. Notice also that for very large τ_c $\gamma \rightarrow \tau_c/r\,[-\sin\theta+i\cos\theta]$. Thus γ asymptotically approaches this line in the complex γ plane. This path of integration over the variable γ satisfies all the above conditions on Γ_1 and τ_c and has the proper integration limits. It is also shown in Figure 2.2(4) for the above elastic wave velocities and for x = h = 10 km.

We now wish to change the variable of integration from γ to τ_c for each term of the equation set 2.2-22 individually. Let us consider first equation 2.2-25. *This term involves changing integration* over γ to that over τ_α. The limits of integration may be easily found. From equation 2.2-23 we see that

$$\lim_{\gamma\to 0} \tau_\alpha = \frac{r\cos\theta}{\alpha}$$

and from the identities $\tau_\alpha = -\gamma x+\eta_\alpha h$, $\eta_\alpha = [1/\alpha^2-\gamma^2]^{1/2}$, $x = r\sin\theta$, and $h = r\cos\theta$ as well as the asymptotic approach of γ to the line $\tau_\alpha/r[-\sin\theta+i\cos\theta]$ for large τ_α we have

$$\lim_{\gamma\to-\infty+i\infty} \tau_\alpha = \lim_{\tau_\alpha/r\to\infty} \{r\cos\theta[\frac{1}{\alpha^2} - \{\frac{\tau_\alpha}{r}(-\sin\theta+i\cos\theta)\}^2]^{1/2}$$

$$- r\sin\theta[\frac{\tau_\alpha}{r}(-\sin\theta+i\cos\theta)]\}$$

$$= \lim_{\tau_\alpha/r\to\infty} \{r\cos\theta[\frac{1}{\alpha^2}+\frac{\tau_\alpha^2}{r^2} e^{i2\theta}]^{1/2} - ir\frac{\tau_\alpha}{r}\sin\theta e^{i\theta}\}$$

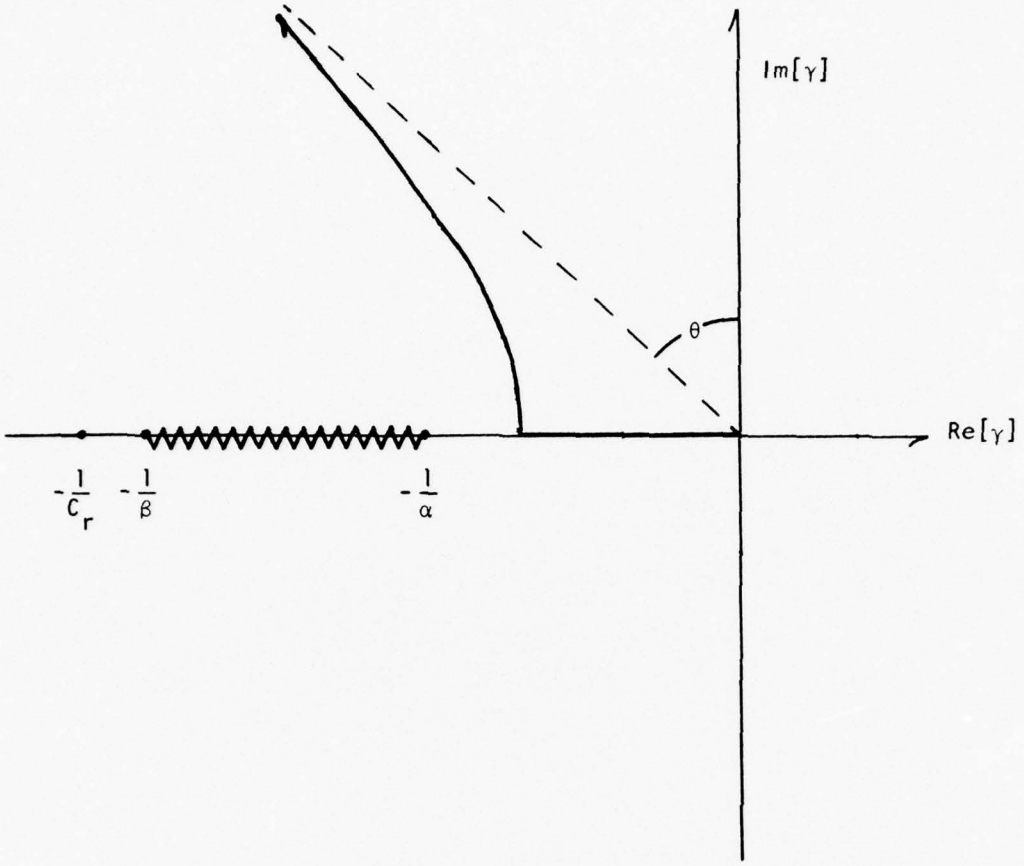


Fig. 2.2(4) Contour for which the application of the Cagniard-de Hoop method is allowed. The singularities of the problem are also shown. In this figure α=5.58 km/sec, β=2.90 km/sec, and θ=45°.

$$= \lim_{\tau_\alpha/r\to\infty} \{r\cos\theta \frac{\tau_\alpha}{r} e^{i\theta} - ir\sin\theta \frac{\tau_\alpha}{r} e^{i\theta}\}$$

$$= \lim_{\tau_\alpha/r\to\infty} \{\tau_\alpha e^{i\theta} e^{-i\theta}\} = \infty$$

where we have used Euler's formula

$$e^{i\theta} = \cos\theta + i\sin\theta$$

For $\theta \leq \pi/2$ we have $r\cos\theta/\alpha \leq r/\alpha$. This and equations 2.2-23 and 2.2-24 suggest that the integrals be separated into several terms to avoid ambiguity. Using the above limits of integration and equation 2.2-24 we may write equation 2.2-25 as

$$V_1(x,o,s) = \frac{1}{\pi\mu} \int_{\frac{r\cos\theta}{\alpha}}^{\frac{r}{\alpha}} \mathrm{Im}\{\frac{2\gamma^2\eta_\beta E(s)+2\gamma\eta_\alpha\eta_\beta G(s)}{R} \cdot \frac{-\eta_\alpha e^{-s\tau_\alpha}}{\sqrt{r^2/\alpha^2-\tau_\alpha^2}}\}d\tau_\alpha$$

$$+ \frac{1}{\pi\mu} \int_{\frac{r}{\alpha}}^{\infty} \mathrm{Im}\{\frac{2\gamma^2\eta_\beta E(s)+2\gamma\eta_\alpha\eta_\beta G(s)}{R} \cdot \frac{i\eta_\alpha e^{-s\tau_\alpha}}{\sqrt{\tau_\alpha^2-r^2/\alpha^2}}\}d\tau_\alpha$$

But for $r\cos\theta/\alpha < \tau_\alpha < r/\alpha$ we have seen that γ is real and, furthermore, $\gamma < 1/\alpha < 1/\beta$ in this range. Then η_α, η_β, and R are also real so that the integrand of the first term in the above expression is identically zero. We are left with

$$V_1(x,o,s) = \frac{1}{\pi\mu} \int_{\frac{r}{\alpha}}^{\infty} \mathrm{Re}\{\frac{2\gamma^2\eta_\alpha\eta_\beta E(s)+2\gamma\eta_\alpha^2\eta_\beta G(s)}{R\sqrt{\tau_\alpha^2-r^2/\alpha^2}} e^{-s\tau_\alpha}\}d\tau_\alpha \qquad 2.2\text{-}26$$

where we have used

$$\int \mathrm{Im}\{iz\}\,dz - \int \mathrm{Re}\{z\}\,dz$$

We now make one final concession to generality. Let the functional form of the forcing function be the Dirac delta as previously defined. Then $E(s) = G(s) = \mathcal{L}\{\delta(t)\} = 1$. The problem has now been maneuvered

into the form indicated in equation 2.2-20. That is, with the judicious use of the Heaviside unit step function defined as

$$H(x) = \begin{cases} 0 & , \quad x < 0 \\ 1 & , \quad x > 0 \end{cases}$$

we have,

$$V_1(x,o,s) = \frac{1}{\pi\mu} \int_0^\infty \frac{H(\tau_\alpha - r/\alpha)}{\sqrt{\tau_\alpha^2 - r^2/\alpha^2}} \left[\mathrm{Re}\left\{ \frac{2\gamma^2 \nu_\alpha \eta_\beta}{R} \right\} + \mathrm{Re}\left\{ \frac{2\gamma \eta_\alpha^2 \eta_\beta}{R} \right\} \right] e^{-s\tau_\alpha} d\tau_\alpha$$

But this is just the definition of the t s forward Laplace transform so that we have finally that

$$v_1(x,o,t) = \frac{1}{\pi\mu} \frac{H(t - r/\alpha)}{\sqrt{t^2 - r^2/\alpha^2}} \left[\mathrm{Re}\left\{ \frac{2\gamma^2 \eta_\beta \eta_\alpha}{R} \right\} + \mathrm{Re}\left\{ \frac{2\gamma \eta_\alpha^2 \eta_\beta}{R} \right\} \right]$$

The physical interpretation of this expression is straightforward. $v_1(x,o,t)$ is the vertical displacement at (x,o,t) due to the arrival of compressional waves from a point source at (o,h,o).

There is one additional complication encountered in taking $d\tau_\beta$ integrals as we shall now see.

Let us now consider the second term in the expression for $V(x,o,s)$ as it appears in equation 2.2-22. This is

$$V_2(x,o,s) = \frac{1}{\pi\mu} \int_0^{i\infty} \mathrm{Im}\left\{ \frac{1}{R} \left(\left[\eta_\beta (\eta_\beta^2 - \gamma^2) E(s) - \gamma(\eta_\beta^2 - \gamma^2) G(s) \right] e^{s(\gamma x - \eta_\beta h)} \right) \right\} d\gamma \qquad 2.2\text{-}27$$

We may now proceed essentially as before. Now, however, the appropriate c in the expressions 2.2-23 and 2.2-24 is β. The limits of integration are found to be

$$\lim_{\gamma \to 0} \tau_\beta = \frac{r \cos\theta}{\beta}$$

$$\lim_{\gamma \to -\infty + i\infty} \tau_\beta = \infty$$

and we have from equations 2.2-23, 2.2-24, 2.2-27, and the above considerations

$$V_2(x,o,s) = \frac{1}{\pi\mu} \int_{\frac{r\cos\theta}{\beta}}^{\frac{r}{\alpha}} \mathrm{Im}\left\{\frac{[\eta_\beta(\eta_\beta^2-\gamma^2)E(s)-\gamma(\eta_\beta^2-\gamma^2)G(s)]}{R} \frac{-\eta_\beta e^{-s\tau_\beta}}{\sqrt{r^2/\beta^2-\tau_\beta^2}}\right\} d\tau_\beta$$

$$+ \frac{1}{\pi\mu} \int_{\frac{r}{\beta}}^{\infty} \mathrm{Im}\left\{\frac{\eta_\beta(\eta_\beta^2-\gamma^2)E(s)-\gamma(\eta_\beta^2-\gamma^2)G(s)}{R} \frac{i\eta_\beta e^{-s\tau_\beta}}{\sqrt{\tau_\beta^2-r^2/\beta^2}}\right\} d\tau_\beta \qquad 2.2\text{-}28$$

It is easily shown that for integration over the variable τ_β the argument of the integrand of the first integral in the above expression is not real for all τ_β between $r\cos\theta/\beta$ and r/β. That is, the first integral may no longer be disregarded. Since $\alpha > \beta$ for any elastic solid it follows that $1/\alpha < 1/\beta$. Then for some θ between 0 and $\pi/2$ we must have $r\cos\theta/\beta < r/\alpha$. Let us denote that angle for which the above inequality is first true as θ_{cr}. For relative source-receiver geometries such that $\theta \geq \theta_{cr}$ it may be shown that there is a time, $t = t_{cr}$ at which $\gamma = -1/\alpha$. At greater times γ and η_β remain real but η_α becomes complex. It may be further shown that

$$\frac{r\cos\theta}{\beta} \leq t_{cr} \leq \frac{r}{\beta}$$

and that

$$t_{cr} = \frac{r\sin\theta}{\alpha} + \frac{r\cos\theta}{\beta}\cos\theta_{cr}$$

where $\cos\theta_{cr} = \sqrt{1-\beta^2/\alpha^2}$

Thus equation 2.2-28 may be written

$$V_2(x,o,s) = \frac{1}{\pi\mu}\int_{t_{cr}}^{\frac{r}{\beta}} \mathrm{Im}\{\frac{\eta_\beta(\eta_\beta^2-\gamma^2)E(s)-\gamma(\eta_\beta^2-\gamma^2)G(s)}{R} \frac{-\eta_\beta e^{-s\tau_\beta}}{\sqrt{r^2/\beta^2-\tau_\beta^2}}\}d\tau_\beta$$

$$+ \frac{1}{\pi\mu}\int_{\frac{r}{\beta}}^{\infty} \mathrm{Im}\{\frac{\eta_\beta(\eta_\beta^2-\gamma^2)E(s)-\gamma(\eta_\beta^2-\gamma^2)G(s)}{R} \frac{i\eta_\beta e^{-s\tau_\beta}}{\sqrt{\tau_\beta^2-r^2/\beta^2}}\}d\tau_\beta$$

As before we may use the Heaviside unit step function and the i in the second integral to write

$$V_2(x,o,s) = \frac{1}{\pi\mu}\int_0^\infty \frac{H(\tau_\beta-r/\beta)}{\sqrt{\tau_\beta^2-r^2/\beta^2}}\mathrm{Re}\{\frac{\eta_\beta^2(\eta_\beta^2-\gamma^2)E(s)-\gamma\eta_\beta(\eta_\beta^2-\gamma^2)G(s)}{R}\}e^{-s\tau_\beta}d\tau_\beta$$

$$- \frac{1}{\pi\mu}\int_0^\infty H(\tau_\beta-t_{cr})\frac{H(r/\beta-\tau_\beta)}{\sqrt{r^2/\beta^2-\tau_\beta^2}}\mathrm{Im}\{\frac{\eta_\beta^2(\eta_\beta^2-\gamma^2)E(s)-\gamma\eta_\beta(\eta_\beta^2-\gamma^2)G(s)}{R}\}e^{-s\tau_\beta}d\tau_\beta$$

Finally, we require $e(t) = g(t) = \delta(t)$ so that $E(s) = G(s) = 1$. Then the above expression again becomes the definition of the forward Laplace transform and we have

$$v_2(x,o,t) = \frac{1}{\pi\mu}\{\frac{H(t-r/\beta)}{\sqrt{t^2-r^2/\beta^2}}[\mathrm{Re}\{\frac{\eta_\beta^2(\eta_\beta^2-\gamma^2)}{R}\}-\mathrm{Re}\{\frac{\gamma\eta_\beta(\eta_\beta^2-\gamma^2)}{R}\}]$$

$$- H(t-t_{cr})\frac{H(r/\beta-t)}{\sqrt{r^2/\beta^2-t^2}}[\mathrm{Im}\{\frac{\eta_\beta^2(\eta_\beta^2-\gamma^2)}{R}\}-\mathrm{Im}\{\frac{\gamma\eta_\beta(\eta_\beta^2-\gamma^2)}{R}\}]\}$$

The physical interpretation is again straightforward. $v_2(x,o,t)$ is the vertical displacement at (x,o,t) due to the arrival of the shear wave (first term) and a wave that is reflected along the surface of the half space (second term). This reflected arrival leaves the source at (o,h,o) as a shear wave and is reflected as a compressional wave. This arrival can only exist for those source-receiver geometries for which $t_{cr} \leq r/\beta$ which we have seen is equivalent to those geometries for which $\theta \geq \theta_{cr}$.

Thus, the physical significance of θ_{cr} is also clear. For any given α and β, it is the angle of incidence on the half-space surface of a shear wave such that a compressional wave is reflected, by Snell's Law, along the surface of the half-space.

We may now solve similarly for W(x,o,s). Doing this and separating each solution into those parts due to point forces in the horizontal and vertical directions we have the desired Green's functions. That is, we derive four equations of the form

$$G_{ij}^{\delta}\ (x,o,t;o,h,o)$$

where this is the displacement in the i direction at (x,o,t) due to an impulseive point force in the j direction at the point (o,h,o). These four equations are written below.

$$G_{xx}^{\delta} = \frac{1}{\pi\mu}\left[\frac{H(t-r/\alpha)}{\sqrt{t^2-r^2/\alpha^2}}\ \mathrm{Re}\left\{\frac{2\gamma^2\eta_\alpha\eta_\beta}{R}\right\}+\frac{H(t-r/\beta)}{\sqrt{t^2-r^2/\beta^2}}\ \mathrm{Re}\left\{\frac{\eta_\beta^{\,2}(\eta_\beta^{\,2}-\gamma^2)}{R}\right\}\right.$$

$$\left. - H(t-t_{cr})\ \frac{H(r/\beta-t)}{r^2/\beta^2-t^2}\ \mathrm{Im}\left\{\frac{\eta_\beta^{\,2}(\eta_\beta^{\,2}-\gamma^2)}{R}\right\}\right]$$

$$G_{xz}^{\delta} = \frac{1}{\pi\mu}\left[\frac{H(t-r/\alpha)}{\sqrt{t^2-r^2/\alpha^2}}\ \mathrm{Re}\left\{\frac{2\gamma\eta_\alpha^{\,2}\eta_\beta}{R}\right\} - \frac{H(t-r/\beta)}{\sqrt{t^2-r^2/\beta^2}}\ \mathrm{Re}\left\{\frac{\gamma\eta_\beta(\eta_\beta^{\,2}-\gamma^2)}{R}\right\}\right.$$

$$\left. + H(t-t_{cr})\ \frac{H(r/\beta-t)}{\sqrt{r^2/\beta^2-t^2}}\ \mathrm{Im}\left\{\frac{\gamma\eta_\beta(\eta_\beta^{\,2}-\gamma^2)}{R}\right\}\right]$$

$$G_{zx}^{\delta} = \frac{1}{\pi\mu}\left[\frac{H(t-r/\alpha)}{\sqrt{t^2-r^2/\alpha^2}}\ \mathrm{Re}\left\{\frac{\gamma\eta_\alpha(\eta_\beta^{\,2}-\gamma^2)}{R}\right\} - \frac{H(t-r/\beta)}{\sqrt{t^2-r^2/\beta^2}}\ \mathrm{Re}\left\{\frac{2\gamma\eta_\alpha\eta_\beta^{\,2}}{R}\right\}\right.$$

$$\left. + H(t-t_{cr})\ \frac{H(r/\beta-t)}{\sqrt{r^2/\beta^2-t^2}}\ \mathrm{Im}\left\{\frac{2\gamma\eta_\alpha\eta_\beta^{\,2}}{R}\right\}\right]$$

$$G^{\delta}_{zz} = \frac{1}{\pi\mu}\left[\frac{H(t-r/\alpha)}{\sqrt{t^2-r^2/\alpha^2}}\ \mathrm{Re}\left\{\frac{\eta_\alpha{}^2(\eta_\beta{}^2-\gamma^2)}{R}\right\} + \frac{H(t-r/\beta)}{\sqrt{t^2-r^2/\beta^2}}\ \mathrm{Re}\left\{\frac{2\gamma^2\eta_\alpha\eta_\beta}{R}\right\}\right.$$

$$\left. - H(t-t_{cr})\ \frac{H(r/\beta-t)}{\sqrt{r^2/\beta^2-t^2}}\ \mathrm{Im}\left\{\frac{2\gamma^2\eta_\alpha\eta_\beta}{R}\right\}\right] \qquad 2.2\text{-}29$$

These functions are plotted below in Figures 2.2(5) and 2.2(6) for the case x = 5 km, z = 0.5 km, α = 5.58 km/sec, β = 3.26 km/sec, and μ = 2.81 x 10" dynes/cm^2. This implies a material density of 2.64 gm/cm^3. This general source geometry was chosen so that $\theta > \theta_{cr}$ and, thus, all phases possible of this medium are present. The shallow source also assures that the Rayleigh wave pulse is well developed. The abscissa scale in each of these plots is 1 sec/in. Following a criterion that will be more pertinent for the model accelerograms to be presented in Chapter 4 than it is here, the ordinant scale is such that the maximum value of either component of a given figure is the zero to peak full scale value for the ordinate scale of that figure. Thus, the ordinate scale will generally vary from figure to figure although it is always the same for both components of any given figure.

The arrival at $t = t_{cr}$ of the reflected SP phase is visible, although small, on the G^{δ}_{xx} and G^{δ}_{xz} traces of Figure 2.2(5) as a small step in displacement approximately 0.1 second after the compressional, or P-wave, arrival. The $[t^2-r^2/c^2]^{-1/2}$ amplitude decrease after the arrival of a phase is also quite noticeable, especially for the G^{δ}_{xx} and G^{δ}_{zz} time histories. This form of amplitude degeneration is, of course, characteristic of the two-dimensional problem.

2.23 The Spatial Derivatives of the Green's Functions

As has been shown in equation 2.1-12, it is the spatial derivatives of the Green's functions developed in the previous section and not

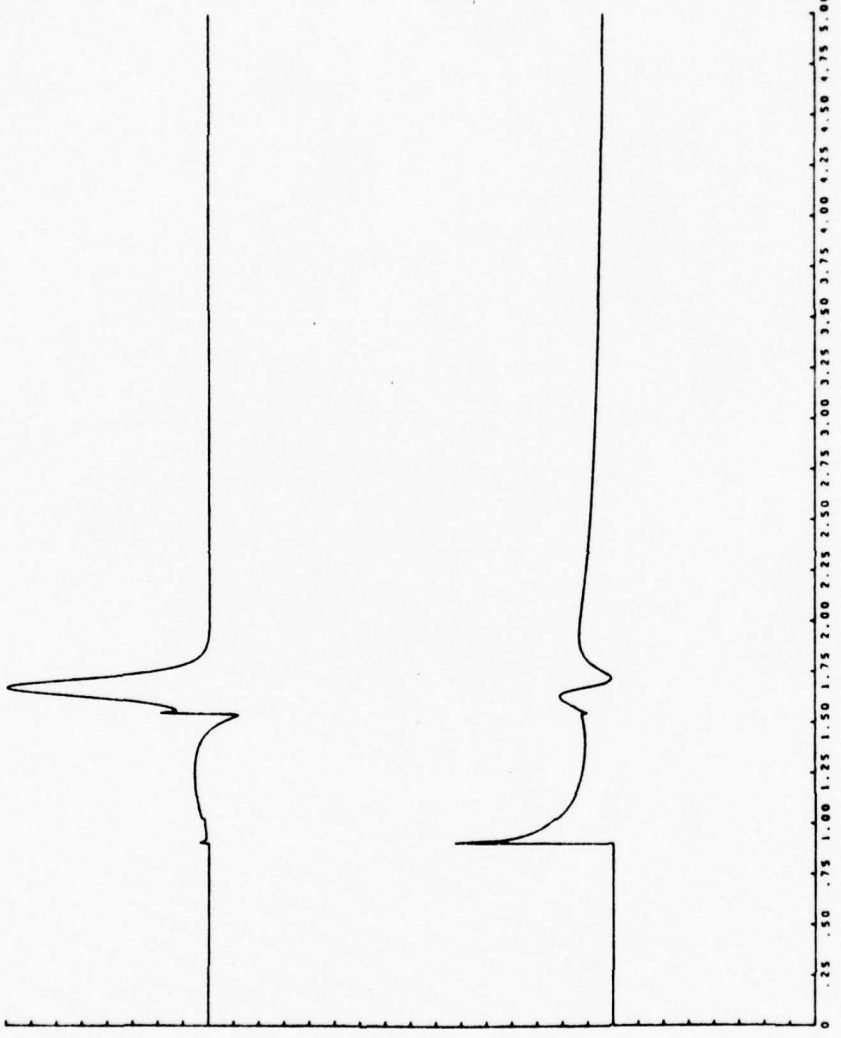


Fig. 2.2(5) $G_{xz}(5,0,t;0,0.5,0)$ - top - and $G_{xx}(5,0,t;0,0.5,0)$ - bottom - for α = 5.58 km/sec and β = 3.26 km/sec.

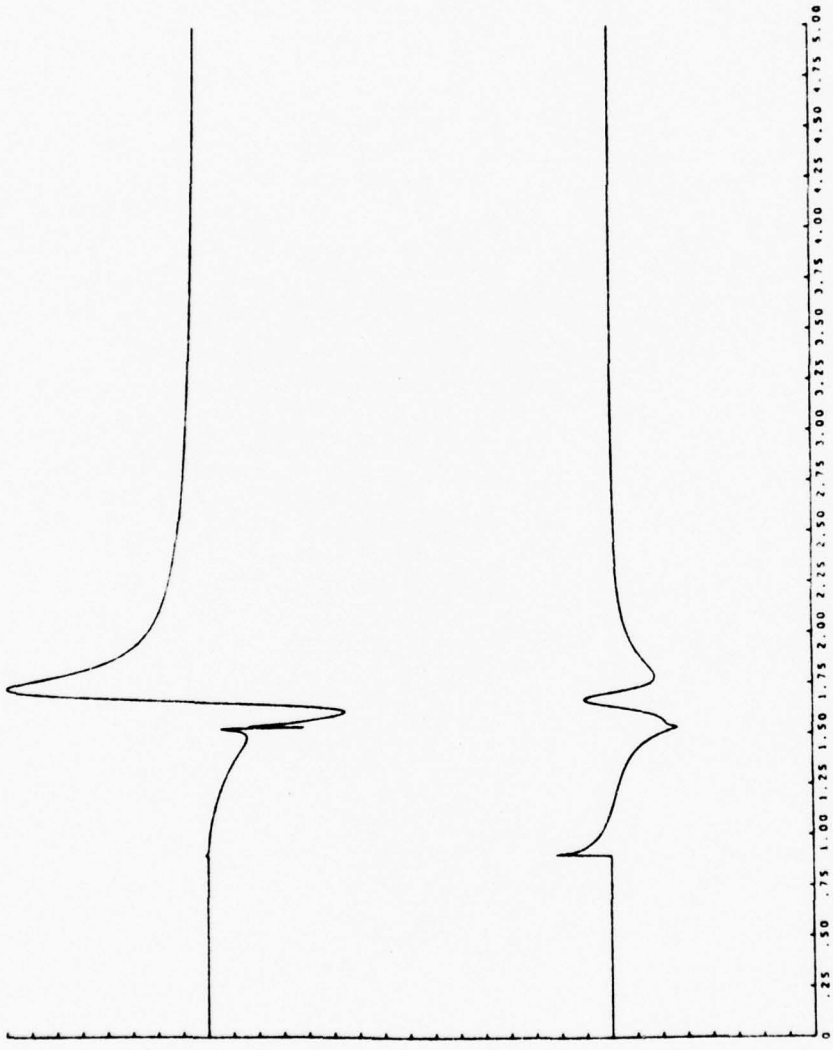


Fig. 2.2(6) $G_{zz}(5,0,t;0,0.5,0)$ - top - and $G_{z\hat{x}}(5,0,t;0,0.5,0)$ - bottom - for α = 5.58 km/sec and β = 3.26 km/sec.

the Green's functions themselves that are needed if we are to calculate displacements due to dislocations on some surface Σ. Straightforward chain rule differentiation of the expressions in equation set 2.2-29 is certainly possible but is also sufficiently monotonous and difficult to suggest looking for an alternative method. Another analytic procedure for evaluating these derivatives does, in fact, exist.

Let us return to the expressions 2.2-22 writing them in conformity with the notation of equation 2.2-29 as

$$\bar{G}_{xx}(x,o,s;o,h,o) = \frac{1}{\pi\mu_o}\int_0^{i\infty} \mathrm{Im}\{\frac{1}{R}[2\gamma^2\eta_\beta e^{s(\gamma x-\eta_\alpha h)} + \eta_\beta(\eta_\beta^2-\gamma^2)e^{s(\gamma x-\eta_\beta h)}]E(s)\}d\gamma$$

$$\bar{G}_{xz}(x,o,s;o,h,o) = \frac{1}{\pi\mu_o}\int_0^{i\infty} \mathrm{Im}\{\frac{1}{R}[2\gamma\eta_\alpha\eta_\beta e^{s(\gamma x-\eta_\alpha h)} - \gamma(\eta_\beta^2-\gamma^2)e^{s(\gamma x-\eta_\beta h)}]G(s)\}d\gamma$$

$$\bar{G}_{zx}(x,o,s;o,h,o) = \frac{1}{\pi\mu_o}\int_0^{i\infty} \mathrm{Im}\{\frac{1}{R}[\gamma(\eta_\beta^2-\gamma^2)e^{s(\gamma x-\eta_\alpha h)} - 2\gamma\eta_\alpha\eta_\beta e^{s(\gamma x-\eta_\beta h)}]E(s)\}d\gamma$$

$$\bar{G}_{zz}(x,o,s;o,h,o) = \frac{1}{\pi\mu_o}\int_0^{i\infty} \mathrm{Im}\{\frac{1}{R}[\eta_\alpha(\eta_\beta^2-\gamma^2)e^{s(\gamma x-\eta_\alpha h)} + 2\gamma^2\eta_\alpha e^{s(\gamma x-\eta_\beta h)}]G(s)\}d\gamma$$

Because of the invarience of the problem with respect to translation in the x direction it may be shown that

$$\frac{\partial}{\partial_{x'}} G = -\frac{\partial}{\partial_x} G$$

$$\frac{\partial}{\partial_{z'}} G = \frac{\partial}{\partial_h} G \qquad 2.2\text{-}30$$

where the primed coordinates are those of the source. In further development we will consider only one of the eight desired derivations explicitly. The others will follow virtually by inspection. Let us differentiate $\bar{G}_{xx}$ with respect to x'. Then from the previous expression for $\bar{G}_{xx}$ and the relationships of equation 2.2-30 we have

$$\frac{\partial}{\partial x'}\bar{G}_{xx} = \frac{-1}{\pi\mu}\int_0^{i\infty}\frac{\partial}{\partial x}\,\mathrm{Im}\,\{i\left[\frac{2\gamma^2\eta_\beta}{R}e^{s(\gamma x-\eta_\alpha h)}\right.$$

$$\left.+\frac{\eta_\beta(\eta_\beta^2-\gamma^2)}{R}e^{s(\gamma x-\eta_\beta h)}\right]E(s)\}d\gamma$$

This differentiation is trivial because γ, and therefore η_α, η_β, and R are all independent of x (or h) at this stage. The dependence of these complex quantities upon x and h does not enter the problem until we require $-\tau_c = \gamma_x - \eta_c h$ to be such that τ_c is real and positive. Thus,

$$\frac{\partial}{\partial x'}\bar{G}_{xx} = -\frac{1}{\pi\mu}\int_0^{i\infty}\mathrm{Im}\,\{\left[\frac{2\gamma^3\eta_\beta}{R}e^{s(\gamma x-\eta_\alpha h)}\right.$$

$$\left.+\frac{\eta_\beta\gamma(\eta_\beta^2-\gamma^2)}{R}e^{s(\gamma x-\eta_\beta h)}\right]sE(s)\}d\gamma$$

Now, just as before, we require $-\tau_c = \gamma x - \eta_c h$ deriving expressions for γ and $d\gamma/d\tau_c$ identical to equations 2.2-23 and 2.2-24, respectively. The limits of integration are also changed as before in changing from γ to τ_c for the variable of integration. Then we have

$$\frac{\partial}{\partial x'}\bar{G}_{xx}(x,o,s;o,h,o) = \frac{1}{\pi\mu}\int_{\frac{r\cos\theta}{\alpha}}^{\frac{r}{\alpha}}\mathrm{Im}\,\frac{2\gamma^3\eta_\beta\eta_\alpha}{R}\,\frac{sE(s)}{\sqrt{r^2/\alpha^2-\tau_\alpha^2}}e^{-s\tau_\alpha}\}d\tau_\alpha$$

$$+\int_{\frac{r\cos\theta}{\beta}}^{\frac{r}{\beta}}\mathrm{Im}\{\frac{\gamma\eta_\beta^2(\eta_\beta^2-\gamma^2)}{R}\,\frac{sE(s)}{\sqrt{r^2/\beta^2-\tau_\beta^2}}e^{-s\tau_\beta}\}d\tau_\beta$$

$$- \int_{\frac{r}{\alpha}}^{\infty} \mathrm{Re}\left\{\frac{2\gamma^3\eta_\beta\eta_\alpha}{R}\,\frac{sE(s)}{\sqrt{\tau_\alpha^2 - r^2/\alpha^2}}\,e^{-s\tau_\alpha}\right\}d\tau_\alpha$$

$$- \int_{\frac{r}{\beta}}^{\infty} \mathrm{Re}\left\{\frac{\gamma\eta_\beta^2(\eta_\beta^2-\gamma^2)}{R}\,\frac{sE(s)}{\sqrt{\tau_\beta^2 - r^2/\beta^2}}\,e^{-s\tau_\beta}\right\}d\tau_\beta\Big]$$

As before the first integral is zero and the lower limit of integration in the second integral may be changed from $r\cos\theta/\beta$ to t_{cr} where t_{cr} is as defined previously. Using the Heaviside step function for convenience of manipulation and noting that $e^{-s\tau_c}$ is real and positive we may write

$$\frac{\partial}{\partial x'}\,\bar{G}_{xx}(x,o,s;o,h,o) = -\frac{1}{\pi\mu}\Big\{\int_0^{\infty}\frac{H(\tau_\alpha - r/\alpha)}{\sqrt{\tau_\alpha^2 - r^2/\alpha^2}}\,\mathrm{Re}\,\frac{2\gamma^3\eta_\alpha\eta_\beta}{R}\,sE(s)\Big\}d\tau_\alpha$$

$$+ \int_0^{\infty}\frac{H(\tau_\beta - r/\beta)}{\sqrt{\tau_\beta^2 - r^2/\beta^2}}\,\mathrm{Re}\Big\{\frac{\gamma\eta_\beta^2(\eta_\beta^2-\gamma^2)}{R}\,sE(s)\Big\}d\tau_\beta$$

$$- \int_0^{\infty}\frac{H(r/\beta - \tau_\beta)}{\sqrt{r^2/\beta^2 - \tau_\beta^2}}\,H(\tau_\beta - t_{cr})\,\mathrm{Im}\Big\{\frac{\gamma\eta_\beta^2(\eta_\beta^2-\gamma^2)}{R}\,sE(s)\Big\}d\tau_\beta\Big\} \qquad 2.2\text{-}31$$

From this point there are several logical ways to proceed. Most fundamentally we may recognize that s is real and positive by definition and may be regarded as a constant for the purposes of integration over τ_c. Thus, removing s from the integrals and again requiring $e(t) = g(t) = \delta(t)$ we have an expression of the general form

$$\frac{\partial}{\partial x'}\,\bar{G}^{\delta}_{xx}(x,o,s;o,h,o) = s\,\mathcal{L}\{f(t)\} \qquad 2.2\text{-}32$$

But from the theory of Laplace transforms

$$s\,\mathcal{L}\{f(t)\} = \{\frac{\partial}{\partial t}\,f(t)\}$$

or, taking the inverse transform of both sides of equation 2.2-32 we have

$$\frac{\partial}{\partial x'} G^{\delta}_{xx}(x,o,t;o,h,o) = \frac{\partial}{\partial t} f(t) \qquad 2.2\text{-}33$$

where, as before, f(t) is just the sum of the integrands of equation 2.2-31 with sE(s) omitted. Thus,

$$\frac{\partial}{\partial x'} G^{\delta}_{xx} = \frac{1}{\pi\mu} \frac{\partial}{\partial t}\left[H(t-t_{cr}) \frac{H(r/\beta-t)}{\sqrt{r^2/\beta^2-t^2}} \operatorname{Im}\left\{\frac{\gamma\eta_\beta^2(\eta_\beta^2-\gamma^2)}{R}\right\}\right.$$

$$\left. - \frac{H(t-r/\alpha)}{\sqrt{t^2-r^2/\alpha^2}} \operatorname{Re}\left\{\frac{2\gamma^3\eta_\alpha\eta_\beta}{R}\right\} - \frac{H(t-r/\beta)}{\sqrt{t^2-r^2/\beta^2}} \operatorname{Re}\left\{\frac{\gamma\eta_\beta^2(\eta_\beta^2-\gamma^2)}{R}\right\}\right] \qquad 2.2\text{-}34$$

Alternatively, we may require e(t) = g(t) = H(t) where H(t) is the Heaviside unit step function. Then E(s) = G(s) = 1/s and sE(s) = sG(s) = 1. Then

$$\frac{\partial}{\partial x'} \bar{G}^{H}_{xx}(x,o,s;o,h,o) = \mathcal{L}\{f(t)\}$$

or

$$\frac{\partial}{\partial x'} G^{H}_{xx}(x,o,t;o,h,o) = f(t) \qquad 2.2\text{-}35$$

Here G^{H}_{xx} is the displacement at (x,o,t) due to a point force whose time functional dependency is H(t) at (o,h,o). With G^{δ} and G^{H} as defined above, equations 2.2-33 and 2.2-35 are seen to be special cases of the more general identity

$$G^{\delta}_{ij}(x,o,t;o,h,o) = \frac{\partial}{\partial t} G^{H}_{ij}(x,o,t;o,h,o)$$

The seven other desired quantities may be derived from equation 2.2-29 and the above considerations virtually by inspection. They are

$$\frac{\partial}{\partial z'} G^{\delta}_{xx} = -\frac{1}{\pi\mu} \frac{\partial}{\partial t}\left[\frac{H(t-r/\alpha)}{\sqrt{t^2-r^2/\alpha^2}} \operatorname{Re}\left\{\frac{2\gamma^2\eta_\alpha^2\eta_\beta}{R}\right\}\right.$$

$$+ \frac{H(t-r/\beta)}{\sqrt{t^2-r^2/\beta^2}} \, Re\{\frac{\eta_\beta{}^3(\eta_\beta{}^2-\gamma^2)}{R}\}$$

$$- H(t-t_{cr}) \, \frac{H(r/\beta-t)}{\sqrt{r^2/\beta^2-t^2}} \, Im\{\frac{\eta_\beta{}^3(\eta_\beta{}^2-\gamma^2)}{R}\}]$$

$$\frac{\partial}{\partial x'} G^{\delta}_{xz} = - \frac{1}{\pi\mu} \frac{\partial}{\partial t}[\frac{H(t-r/\alpha)}{\sqrt{t^2-r^2/\alpha^2}} \, Re\{\frac{2\gamma^2\eta_\alpha{}^2\eta_\beta}{R}\}$$

$$- \frac{H(t-r/\beta)}{\sqrt{t^2-r^2/\beta^2}} \, Re\{\frac{\gamma^2\eta_\beta(\eta_\beta{}^2-\gamma^2)}{R}\}$$

$$+ H(t-t_{cr}) \, \frac{H(r/\beta-t)}{\sqrt{r^2/\beta^2-t^2}} \, Im\{\frac{\gamma^2\eta_\beta(\eta_\beta{}^2-\gamma^2)}{R}\}]$$

$$\frac{\partial}{\partial z'} G^{\delta}_{xz} = - \frac{1}{\pi\mu} \frac{\partial}{\partial t}[\frac{H(t-r/\alpha)}{\sqrt{t^2-r^2/\alpha^2}} \, Re\{\frac{2\gamma\eta_\alpha{}^3\eta_\beta}{R}\}$$

$$- \frac{H(t-r/\beta)}{\sqrt{t^2-r^2/\beta^2}} \, Re\{\frac{\gamma\eta_\beta{}^2(\eta_\beta{}^2-\gamma^2)}{R}\}$$

$$+ H(t-t_{cr}) \, \frac{H(r/\beta-t)}{\sqrt{r^2/\beta^2-t^2}} \, Im\{\frac{\gamma\eta_\beta{}^2(\eta_\beta{}^2-\gamma^2)}{R}\}]$$

$$\frac{\partial}{\partial x'} G^{\delta}_{zx} = - \frac{1}{\pi\mu} \frac{\partial}{\partial t}[\frac{H(t-r/\alpha)}{\sqrt{t^2-r^2/\alpha^2}} \, Re\{\frac{\gamma^2\eta_\alpha(\eta_\beta{}^2-\gamma^2)}{R}\}$$

$$- \frac{H(t-r/\beta)}{\sqrt{t^2-r^2/\beta^2}} \, Re\{\frac{2\gamma^2\eta_\alpha\eta_\beta}{R}\}$$

$$+ H(t-t_{cr}) \, \frac{H(r/\beta-t)}{\sqrt{r^2/\beta^2-t^2}} \, Im\{\frac{2\gamma^2\eta_\alpha\eta_\beta}{R}\}]$$

$$\frac{\partial}{\partial z'} G^{\delta}_{zx} = - \frac{1}{\pi\mu} \frac{\partial}{\partial t}[\frac{H(t-r/\alpha)}{\sqrt{t^2-r^2/\alpha^2}} \, Re\{\frac{\gamma\eta_\alpha{}^2(\eta_\beta{}^2-\gamma^2)}{R}\}$$

$$- \frac{H(t-r/\beta)}{\sqrt{t^2-r^2/\beta^2}} \, Re\{\frac{2\gamma\eta_\alpha\eta_\beta^3}{R}\}$$

$$+ H(t-t_{cr}) \, \frac{H(r/\beta-t)}{\sqrt{r^2/\beta^2-t^2}} \, Im\{\frac{2\gamma\eta_\alpha\eta_\beta^3}{R}\}]$$

$$\frac{\partial}{\partial x'} G^{\delta}_{zz} = - \frac{1}{\pi\mu} \frac{\partial}{\partial t}[\frac{H(t-r/\alpha)}{\sqrt{t^2-r^2/\alpha^2}} \, Re\{\frac{\gamma\eta_\alpha^2(\eta_\beta^2-\gamma^2)}{R}\}$$

$$+ \frac{H(t-r/\beta)}{\sqrt{t^2-r^2/\beta^2}} \, Re\{\frac{2\gamma^3\eta_\alpha\eta_\beta}{R}\}$$

$$- H(t-t_{cr}) \, \frac{H(r/\beta-t)}{\sqrt{r^2/\beta^2-t^2}} \, Im\{\frac{2\gamma^3\eta_\alpha\eta_\beta}{R}\}]$$

$$\frac{\partial}{\partial z'} G^{\delta}_{zz} = - \frac{1}{\pi\mu} \frac{\partial}{\partial t}[\frac{H(t-r/\alpha)}{\sqrt{t^2-r^2/\alpha^2}} \, Re\{\frac{\eta_\alpha^3(\eta_\beta^2-\gamma^2)}{R}\}$$

$$+ \frac{H(t-r/\beta)}{\sqrt{t^2-r^2/\beta^2}} \, Re\{\frac{2\gamma^2\eta_\alpha\eta_\beta^2}{R}\}$$

$$- H(t-t_{cr}) \, \frac{H(r/\beta-t)}{\sqrt{r^2/\beta^2-t^2}} \, Im\{\frac{2\gamma^2\eta_\alpha\eta_\beta^2}{R}\}]$$

In each case the equivalent expressions for $\partial/\partial x' \; G^H_{ij}$ or $\partial/\partial z' \; G^H_{ij}$ may be found by deleting the differentiation with respect to time in the above equations. As we shall see in the next chapter the general ground motion or instrumental record appropriate for more sophisticated source time histories may be derived from the convolution of the above Green's functions with a source and instrumental term. In such a case it is always possible to modify the source or instrument response terms in a straightforward way so that G^H_{ij} terms may be used to obtain results equivalent to those derived from the use of G^{δ}_{ij} expressions as required

by equation 2.1-15. Thus, the differentiation implied in equations 2.2-34 and 2.2-36 is, in practice, never necessary.

The development of these source and instrument terms is the principal topic of the next chapter.

Chapter 3

Development of Several Source-Instrument Terms

3.1 Introduction

Having solved the problem of an implusive line source in a half space we are ready to apply this solution to some practical question. Therefore, it is of interest to find an earthquake whose ground motion was recorded at a site approximately satisfying the conditions under which the mathematical solution was derived.

As we have seen these requirements are fairly well met by the Pacoima Dam strong-motion station for the source fault-geometry of the San Fernando earthquake of February 9, 1971. However, before we can attempt to understand the strong-motion records written at Pacoima Dam for the San Fernando earthquake we must consider all the parameters necessary to the generation of a model acceleration record. These will include the instrument response of the accelerometer, the time history of the source at any point on the model fault, the geometry of some two-dimensional fault relative to the location on the surface of the half space at which we wish to evaluate acceleration, the propagation velocity of the time history along this fault surface, and the amplitude of the final displacements of the sides of the fault relative to each other as a function of position along the fault.

It is the purpose of this chapter to discuss these parameters in a general way. The actual synthesis of artificial accelerograms will be deferred to Chapter 4.

3.2 The Strong-Motion Instruments

The mathematical theory developed in Chapter 2 will give the ground displacement at some surface point which has been fixed

geometrically relative to a line source at some depth in the half space. Even when a collection of these line sources have been manipulated so as to model the desired history of motion on some model fault surface we must convert the model motion at the desired recording site into the equivalent accelerogram that would be written by some specified instrument at this site. This record can then be directly compared to the actual strong-motion record of the test earthquake. This comparison is, of course, the criterion by which the success or failure of a model is judged.

To see how we may include the instrument in the synthesis of the accelerogram for a given model, let us consider the theory of forced and unforced single degree of freedom harmonic oscillators.

First consider the damped, unforced simple harmonic system represented by the equation

$$\ddot{x}(t) + 2\eta\dot{x}(t) + \omega_n^2 x(t) = 0 \qquad 3.2\text{-}1$$

In this expression a dot stands for differentiation with respect to time, ω_n is the undamped or natural angular frequency of the oscillator, and η is a constant related to the damping of the system. Where $x(o)$ and $\dot{x}(o)$ are the initial displacement and velocity of the system, respectively, the well-known solution to the differential equation 3.2-1 is:

$$x(t) = e^{-\eta t}\{x(o)\cos(\sqrt{\omega_n^2-\eta^2}\ t) + \frac{\dot{x}(o)+\eta x(o)}{\sqrt{\omega^2-\eta^2}}\sin(\sqrt{\omega_n^2-\eta^2}\ t)\} \qquad 3.2\text{-}2$$

Equations 3.2-1 and 3.2-2 are useful for demonstrating the significance of the two constants η and ω_n and they are also helpful in relating the

many constant pairs equivalent to η and ω_n.

For example, let us take advantage of the periodic nature of equation 3.2-2 and define ε to be the ratio of two successive peaks in amplitude of $x(t)$. This ratio will obviously be a function of the degree of damping of the system and we see from equation 3.2-2 that the period of harmonic motion is also a function of damping. Let us call the damped angular frequency ω_d and the equivalent damped period T_d, where

$$\omega_d \equiv \sqrt{\omega_n^2 - \eta^2} \equiv \frac{2\pi}{T_d}$$

Then

$$\cos(\sqrt{\omega_n^2 - \eta^2}\, t) \equiv \cos \omega_d t \equiv \cos \omega_d (t+T_d)$$

$$\sin(\sqrt{\omega_n^2 - \eta^2}\, t) \equiv \sin \omega_d t \equiv \sin \omega_d (t+T_d)$$

and it follows that

$$\varepsilon \equiv \frac{x(t)}{x(t+T_d)} = \frac{e^{-\eta t}}{e^{-\eta(t+T_d)}} = e^{\eta T_d} \qquad 3.2\text{-}3$$

So defined, ε is known as the damping ratio. η is the damping coefficient. Another common way of relating ω_d to ω_n is as below:

$$\omega_d \equiv \sqrt{\omega_n^2 - \eta^2} = \omega_n \sqrt{1 - \eta^2/\omega_n^2} \equiv \omega_n \sqrt{1-\rho^2} \qquad 3.2\text{-}4$$

where obviously $\rho = \eta/\omega_n$. This new constant is useful because it is the percent critical damping since for $\rho = 1$ $\omega_d = 0$ and this is the criterion for critical damping. We may define a new constant, μ, such that this is the ratio of the damped to the undamped angular frequency. Thus we have

$$\mu \equiv \frac{\omega_d}{\omega_n} = \sqrt{1-\rho^2} \qquad 3.2\text{-}5$$

We may use these relationships to find percent critical damping, ρ, in terms of the damping ratio, ε. That is, from above considerations

$$\varepsilon = e^{2\pi\rho/\mu} = e^{2\pi\rho/\sqrt{1-\rho^2}}$$

Taking the natural logarithm of both sides and performing some algebra we find

$$\rho = \frac{\ln\varepsilon}{[(2\pi)^2+(\ln\varepsilon)^2]^{1/2}} \qquad 3.2\text{-}6$$

Using these formulas we may find any of the common constants (ω_n, ω_d, η, ρ, μ, ε) once we know any two of them. Since all of these constants are in popular use, these relationships will prove useful later.

Now let us continue the analysis to consider the forced case. The equation of motion now becomes:

$$\ddot{x} + 2\eta\dot{x} + \omega_n^2 = -\ddot{u} \qquad 3.2\text{-}7$$

where u(t) is the ground displacement and a dot represents differentiation with respect to time, as before. The response of a damped single degree of freedom oscillator to general ground motion is well known. Housner (1941) has presented the results for an undamped oscillator using a method given by Lord Rayleigh (Theory of Sound, v. 1 p.74). A somewhat more straightforward method using variation of parameters and applicable to damped as well as undamped systems is outlined by Bullen (1965, p.145). From these earlier studies we may write:

$$x(t) = -\frac{1}{\omega_d}\int_0^t \ddot{u}(\tau)e^{-\eta(t-\tau)}\sin\omega_d(t-\tau)d\tau$$

$$= -\frac{1}{\omega_d}[\ddot{u}(t) * e^{-\eta t}\sin\omega_d t] \qquad 3.2\text{-}8$$

where ω_d and η are as defined in equation 3.2-4. The asterisk denotes convolution.

It is often convenient to define instrument response in terms of ground velocity or ground displacement. Integrating equation 3.2-8 by parts and writing the solution in terms of a convolution we have:

$$x(t) = \dot{u}(o)\,\frac{e^{-\eta t}}{\omega_d}\sin\omega_d t + \frac{1}{\omega_d}\left[\dot{u}(t) * e^{-\eta t}(\eta\sin\omega_d t - \omega_d\cos\omega_d t)\right]$$

$$= \dot{u}(o)\,\frac{e^{-\eta t}}{\omega_d}\sin\omega_d t - \frac{1}{\omega_d}\left[\dot{u}(t) * \frac{d}{dt}(e^{-\eta t}\sin\omega_d t)\right] \qquad 3.2\text{-}9$$

Finally, integrating once more by parts we find:

$$x(t) = [\dot{u}(o)-\eta u(o)]\frac{e^{-\eta t}}{\omega_d}\sin\omega_d t + u(o)e^{-\eta t}\cos\omega_d t - u(t) - \frac{1}{\omega_d}\{u(t)*e^{-\eta t}[(\eta^2-\omega_d{}^2)\sin\omega_d t - 2\eta\omega_d\cos\omega_d t]\}$$

$$= [\dot{u}(o)-\eta u(o)]\frac{e^{-\eta t}}{\omega_d}\sin\omega_d t + u(o)e^{-\eta t}\cos\omega_d t - u(t) - \frac{1}{\omega_d}\left[u(t)*\frac{d^2}{dt^2}(e^{-\eta t}\sin\omega_d t)\right] \qquad 3.2\text{-}10$$

In these expressions $\dot{u}(o)$ and $u(o)$ are the initial velocity and displacement of the forcing function respectively.

Finally, we may take the Laplace transform of equation 3.2-7 to get the frequency domain equivalent of equation 3.2-10. This is

$$\bar{X}(s) = -\frac{s^2}{[(s+\eta)^2+\omega_d{}^2]}\,\bar{U}(s) + \frac{[\dot{u}(o)-\eta u(o)]}{[(s+\eta)^2+\omega_d{}^2]} + \frac{(s+\eta)\,u(o)}{[(s+\eta)^2+\omega_d{}^2]} \qquad 3.2\text{-}11$$

where $\underline{\bar{X}}(s) = x(t)$ etc. This form of the solution is useful if $u(t)$ is such that

$$\frac{s^2}{[(s+\eta)^2+\omega_d^2]}\,\bar{U}(s)$$

has a recognizable inverse transform. Obviously where $\dot{u}(o) = u(o) = 0$ the problem is somewhat simplified.

3.3 The Time History of a Point Source

As before we will adopt the convention of using the term "point source" when talking about an infinite line source since this is equivalent to a two-dimensional point source. Let us consider for the moment one such point source.

When we first considered this problem it was natural to talk about forces acting at this point. These forces produced motion at the surface of the half space which we found we could determine. The problem was then to find a way to model motion at the surface due to a dislocation at the same source point because it was desired to simulate surface motion due to faulting. The point *dislocation*, of course, has long been though of as the fundamental mathematical unit of fault model motion.

We know, however, that this jump from one position to another, this process whereby two originally coincident points find themselves some finite distance apart with no passage of time, is unlikely to be an accurate description of what happens on a fault surface during a seismic event. Knowing this does not help tell us what actually does happen.

In this section we will examine three source terms that will get us from the original to the final state more smoothly.

3.31 The Source as a Finite Ramp Function

The simplest way to require a finite time for finite displacement at the source is to use the truncated ramp function.

$$s(t) = \frac{t}{T}\,[H(t)-H(t-T)] + H(t-T) \qquad 3.3\text{-}1$$

as seen in Figure 3.3(1) motion begins at t = 0, proceeds linearly until t = T, and then stops. T is called the rise time. The amplitude of the final displacement is normalized to one by the form used in equation 3.3-1. We may easily find the Laplace transform of the source term equation 3.3-1. This is:

$$L\{s(t)\} \equiv S(s) = \frac{1}{Ts^2}\,(1-e^{-sT}) \qquad 3.3\text{-}2$$

Now as before let u(t) represent the ground motion at a given location and let x(t) be the motion displayed on the record of the instrument placed at the same location. If now we define i(t) to be the time domain equivalent of the instrument transfer function we have:

$$x(t) = i(t) * u(t) \qquad 3.3\text{-}3$$

Let us further resolve u(t) into a geometrical term and a source term, G(t) and s(t) respectively. For convenience we define G(t) to be the ground motion at some given location due to a point dislocation that turns on and off like the Dirac delta function $\delta(t)$. In short, G(t) is the dislocation Green's function for our problem. Another useful quantity is a similar G(t) giving ground motion at the same location due to a point dislocation that turns on like the Heaviside unit step function. We will call the first quantity $G^{\delta}(t)$ and the second $G^{H}(t)$.

These two quantities are closely related to each other since:

$$G^{\delta}(t) = \frac{d}{dt}\,G^{H}(t)$$

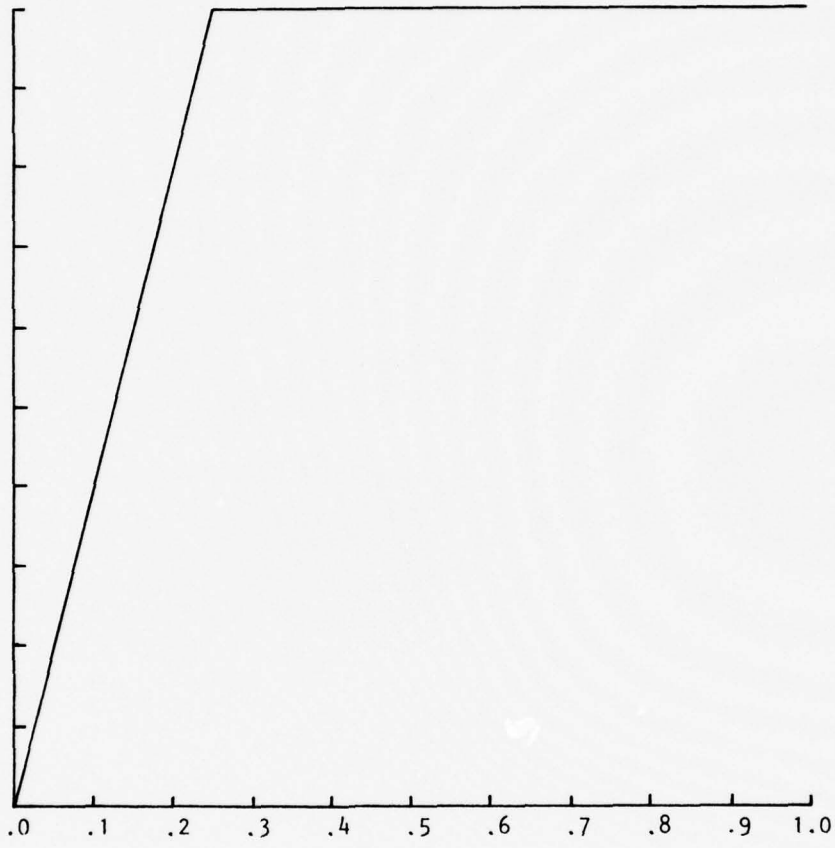


Fig. 3.3(1) The finite ramp source function.
$s(t) = \frac{t}{T}[H(t) - H(t-T)] + H(t-T)$, $T = .25$

The only reason to distinguish between them at this point will now be made clear. In equation 3.3-3 we may now write

$$x(t) = i(t) * [G^{\delta}(t) * s(t)] \qquad 3.3\text{-}4$$

The precise manner in which our point along the fault moves is clear in this expression since it is just s(t). However, the more useful Green's function to use in this equation is $G^{H}(t)$ since it is this value that may be found analytically for a two-dimensional dislocation without the cumbersome necessity of taking a time derivative. Thus, having made the distinction between $G^{\delta}(t)$ and $G^{H}(t)$ we may still keep a simple mental picture of what the fault is doing and write

$$x(t) = i(t) * [\frac{d}{dt} G^{H}(t) * s(t)]$$

from which it is a simple step to find:

$$x(t) = i(t) * [G^{H}(t) * \frac{d}{dt} s(t)] \qquad 3.3\text{-}5$$

For the simple sources we will investigate here it will always be possible to find the quantity

$$i(t) * \frac{d}{dt} s(t) \qquad 3.3\text{-}6$$

analytically. Thus, we need only take one numerical convolution to arrive at the final model record derived from a point dislocation with some straightforward source term.

The part of equation 3.3-5 represented by equation 3.3-6 can be easily solved. We have already seen the transform of i(t).

$$\mathcal{L}\{i(t)\} = \frac{s^2}{(s+\eta)^2+b^2}$$

Also where s(t) is as defined in equation 3.3-1

$$\mathcal{L}\{\frac{d}{dt} s(t)\} = \frac{1}{Ts} (1-e^{-sT})$$

where $b = \omega_d = \sqrt{\omega_n^2 - \eta^2}$ and:

$$L\{i(t) * \frac{d}{dt} s(t)\} = [\frac{s^2}{(s+\eta)^2+b^2}] \frac{1}{Ts} (1-e^{-sT})$$

$$= \frac{1}{T} \{\frac{s}{(s+\eta)^2+b^2} (1-e^{-sT})\} \qquad 3.3\text{-}7$$

From tables we may find the inverse transform of this expression to be:

$$i(t) * \frac{d}{dt} s(t) = \frac{e^{-\eta t}}{bT} [b \cos bt - \sin bt] H(t)$$

$$- \frac{e^{-\eta(t-T)}}{bT} [b \cos b(t-T) - \eta \sin b(t-T)] H(t-T)$$

3.3-8

A plot of this function for T = .25 second appears in Figure 3.3(2). It is obvious from equation 3.3-8 and from its plot that discontinuities exist at t = 0 and at t = T. It will be seen later that these discontinuities introduce severe difficulties into the problem of generating a model accelerogram. For the moment further discussion of this problem will be deferred until two progressively smoother finite ramp functions can be proposed.

3.32 The Source as a Finite Ramp Function with Continuous First Derivatives

Consider the source term:

$$s(t) = \frac{1}{2} [1-\cos(\frac{\pi t}{T})] (H(t)-H(t-T)) + H(t-T) \qquad 3.3\text{-}9$$

We see that displacement represented by this equation starts at a value of zero at t = 0 and stops at a value of one at $t \geq T$ in such a way that this displacement and its first derivative are continuous for all $t \geq 0$. A plot of this source term with T = .25 appears in Figure 3.3(3).

As before, we start further analysis of this function by taking

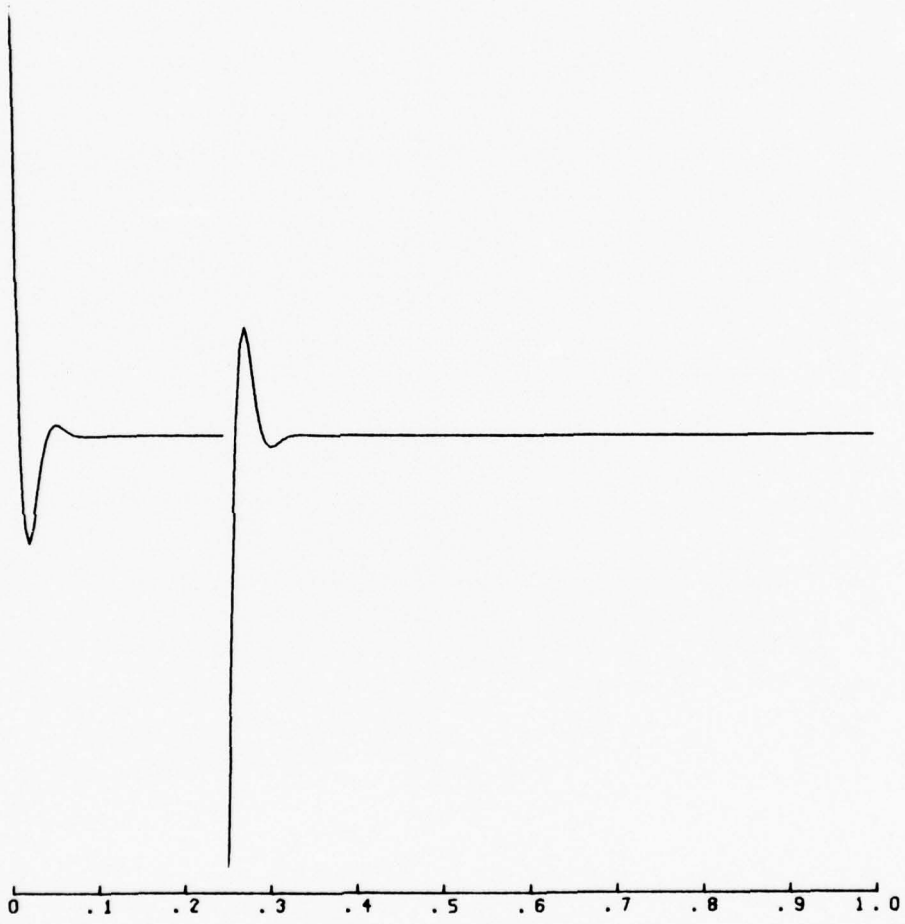


Fig. 3.3(2) $i(t)*\frac{d}{dt}\,s(t)$, T = .25 where s(t) is the source of Fig. 3.3(1).

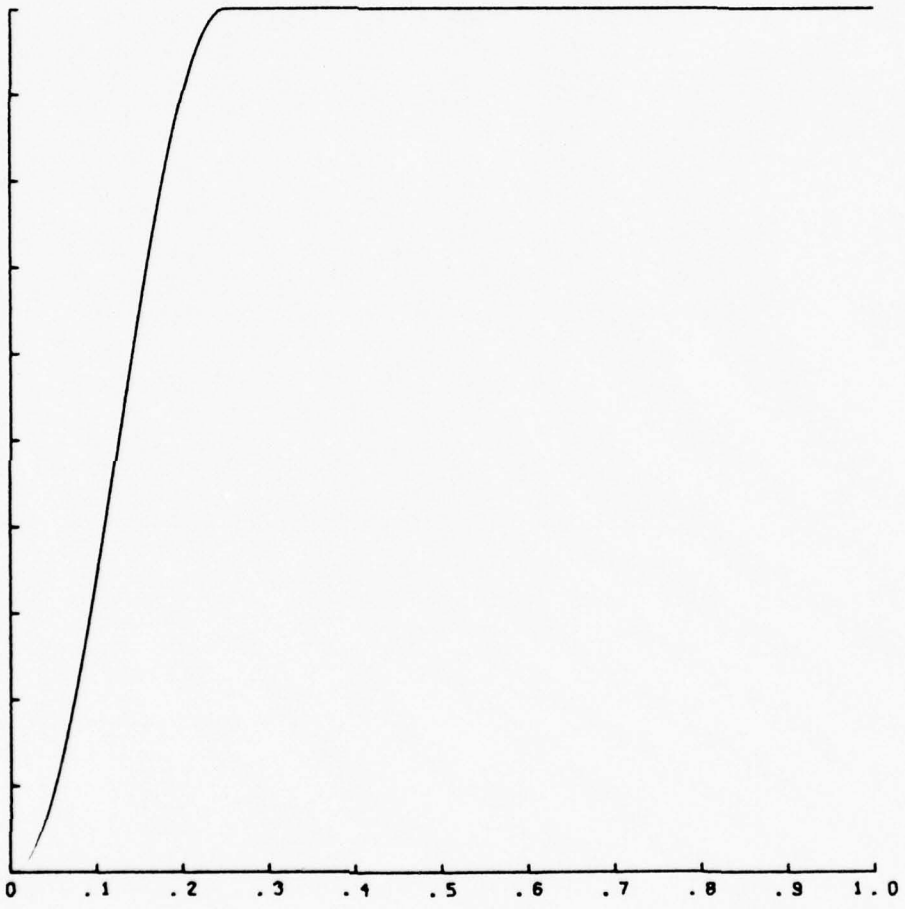


Fig. 3.3(3) The quarter cycle cosine source term.
$s(t) = \frac{1}{2}[1-\cos(\frac{\pi t}{T})][H(t)-H(t-T)] + H(t-T)$, $T = .25$

its Laplace transform which may be shown to be:

$$L\{s(t)\} = \frac{1}{2}(1+e^{-sT})\left[\frac{(\pi/T)^2}{s(s^2+(\pi/T)^2}\right] \qquad 3.3\text{-}10$$

Also:

$$L\{\frac{d}{dt}\, s(t)\} = \frac{1}{2}(1+e^{-st})\left[\frac{(\pi/T)^2}{s^2+(\pi/T)^2}\right]$$

and, as before,

$$L\{i(t)*\frac{d}{dt}\, s(t)\} = \frac{1}{2}(1+e^{-st})\left[\frac{(\pi/T)^2}{s^2+(\pi/T)^2}\right]\left[\frac{s^2}{(s+\eta)^2+b^2}\right] \qquad 3.3\text{-}11$$

Ignoring for the moment the translation factor e^{-sT} consider the problem

$$\frac{1}{2}\left[L^{-1}\left\{\frac{a^2}{s^2+a^2} \cdot \frac{s^2}{(s+\eta)^2+b^2}\right]\right.$$

$$= \frac{1}{2}\left[L^{-1}\left\{\frac{a^2 s}{s^2+a^2}\right\} * L^{-1}\left\{\frac{s}{(s+\eta)^2+b^2}\right\}\right]$$

where a = /T. Now from Laplace transform tables we have:

$$i(t)*\frac{d}{dt}\, s(t) = \frac{1}{2}\left[L^{-1}\left\{\frac{a^2 s}{s^2+a^2}\right\}*L^{-1}\left\{\frac{s}{(s+\eta)^2+b^2}\right\}\right]$$

$$= \frac{1}{2}\left[a^2 \text{cosat} * \left[e^{-\eta t}\text{cosbt} - \frac{\eta}{b}e^{-\eta t}\text{sinbt}\right]\right]$$

$$= \frac{1}{2}\left[(\text{cosat} * a^2 e^{-\eta t}\text{cosbt}) - \left(\text{cosat} * \frac{a^2\eta}{b}e^{-\eta t}\text{sinbt}\right)\right]$$

Finally, from integration tables and some algebra we have:

$$\frac{a^2}{2b}\left[(\eta^2+(a-b)^2)^{-1}\{[b\text{cosat}-\eta\text{sinat}] \cdot\right.$$

$$[\eta+e^{-\eta t}\{(a-b)\text{sin}(a-b)t - \eta\text{cos}(a-b)t\}]$$

$$+ [b\text{sinat}+\eta\text{cosat}]\cdot[(a-b)-e^{-\eta t}\{\eta\text{sin}(a-b)t +$$

$$(a-b)\text{cos}(a-b)t\}]\}$$

$$+ (\eta^2+(a+b)^2)^{-1}\{[b\cos at + \sin ct]\cdot$$

$$[\eta+e^{-\eta t}\{(a+b)\sin(a+b)t-\eta\cos(a+b)t\}]$$

$$+ [b\sin at-\eta\cos at]\cdot[(a+b)-e^{-\eta t}\{\eta\sin(a+b)t +$$

$$(a+b)\cos(a+b)t\}]\}] \qquad 3.3\text{-}12$$

As may be seen in Figure 3.3(4), a plot of this function for T = .25 has no discontinuities at t = 0 and t = T but the slope is discontinuous at these points. If we include the factor e^{-sT}, the form of equation 3.3-12 is unchanged. We have only to substitute (t-T) for T whenever it occurs. The total source-instrument term is then the difference of these two factors. It is, of course, this difference that is plotted in Figure 3.3(4).

It is now of interest to carry the smoothing of the source term one step farther.

3.33 The Source as a Finite Ramp Function with Continuous First and Second Derivatives

Consider the following polynomial source:

$$s(t) = at^5+bt^4+ct^3+dt^2+et+f$$

We wish to determint the coefficients by requiring that

$$s(o) = \frac{d}{dt}\,s(o) = \frac{d^2}{dt^2}\,s(o) = \frac{d}{dt}\,s(T) = \frac{d^2}{dt^2}\,s(T) = 0$$

$$s(T) = 1$$

It is trivial to show that under these conditions

$$s(t) = \frac{6}{T^5}\,t^5 - \frac{15}{T^4}\,t^4 + \frac{10}{T^3}\,t^3\Bigg|_{0 \le t \le T}$$

Of course s(t) is defined as being equal to one for t > T so that we may write

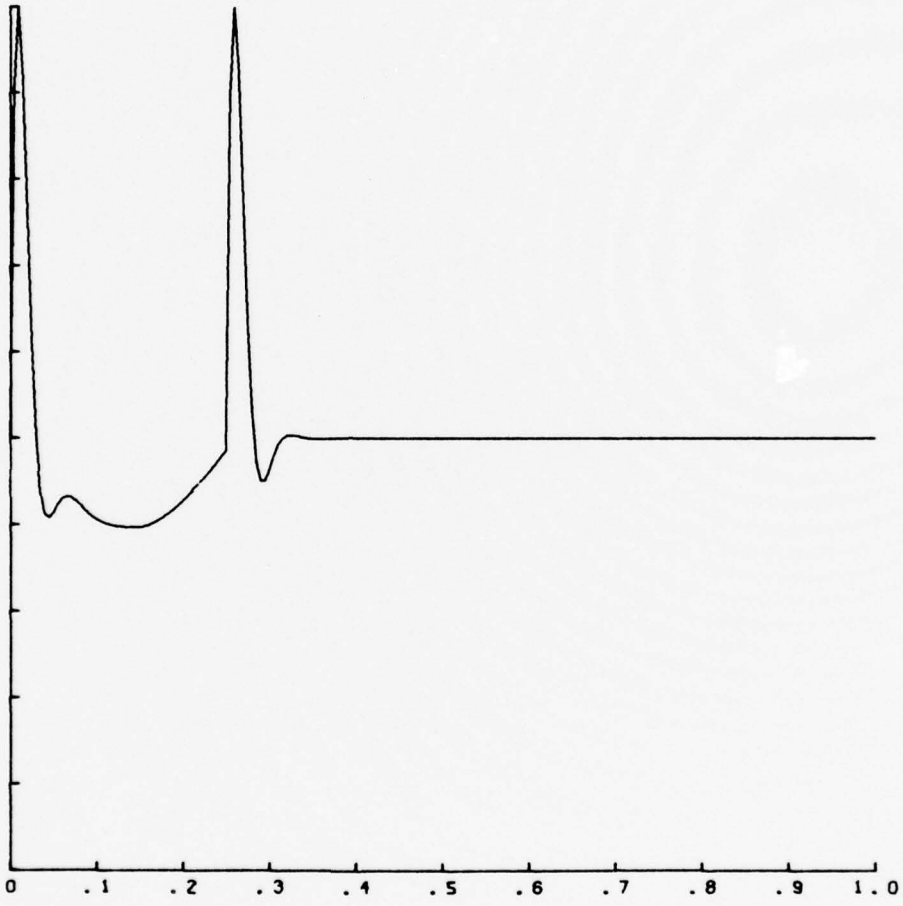


Fig. 3.3(4) $i(t)*\frac{d}{dt}s(t)$, T = .25 where s(t) is the source of Fig. 3.3(3)

$$s(t) = \{[\frac{6}{T^5} t^5 - \frac{15}{T^4} t^4 + \frac{10}{T^3} t^3][H(t) - H(t-T)]$$

$$+ H(t-T)\} \qquad 3.3\text{-}13$$

We see that this equation represents a displacement on the fault much like that of the last source term we considered. Now, however, no discontinuities exist through the second derivative. A plot of equation 3.3-13 appears in Figure 3.3(5), again for T = .25 second.

We may rewrite equation 3.3-13 in a form whose Laplace transform is more easily evaluated.

$$s(t) = \{[\frac{6}{T^5} t^5 - \frac{15}{T^4} t^4 + \frac{10}{T^3} t^3] H(t)$$

$$- [\frac{6}{T^5} (t-T)^5 + \frac{15}{T^4} (t-T)^4 + \frac{10}{T^3} (t-T)^3] H(t-T)\}$$

The Laplace transform of this expression is simply:

$$L\{s(t)\} = \{\frac{60}{T^3 s^4} [\frac{12}{T^2 s^2} - \frac{6}{Ts} + 1]$$

$$- \frac{60e^{-sT}}{T^3 s^4} [\frac{12}{T^2 s^2} + \frac{6}{Ts} + 1]\} \qquad 3.3\text{-}14$$

Again we have the sum of two essentially identical terms. As before, one of the terms has been shifted by the e^{-sT} factor but we know that this is of no concern. Here there is also a different sign in the second term. However, this too will offer no particular difficulty. Considering only the first term of equation 3.3-14 we have:

$$[i(t) * \frac{d}{dt} s(t)]_{\text{first term}} = L^{-1}\{\frac{60}{(s+\eta)^2+b^2}\} *$$

$$L^{-1}\{\frac{1}{sT^3} \frac{12}{T^2 s^2} - \frac{6}{Ts} + 1]\} \qquad 3.3\text{-}15$$

We may immediately write the inverse of the first transform.

$$L^{-1}\{\frac{60}{(s+\ )^2+b^2}\} = \frac{60}{b} e^{-\eta t} \sin bt$$

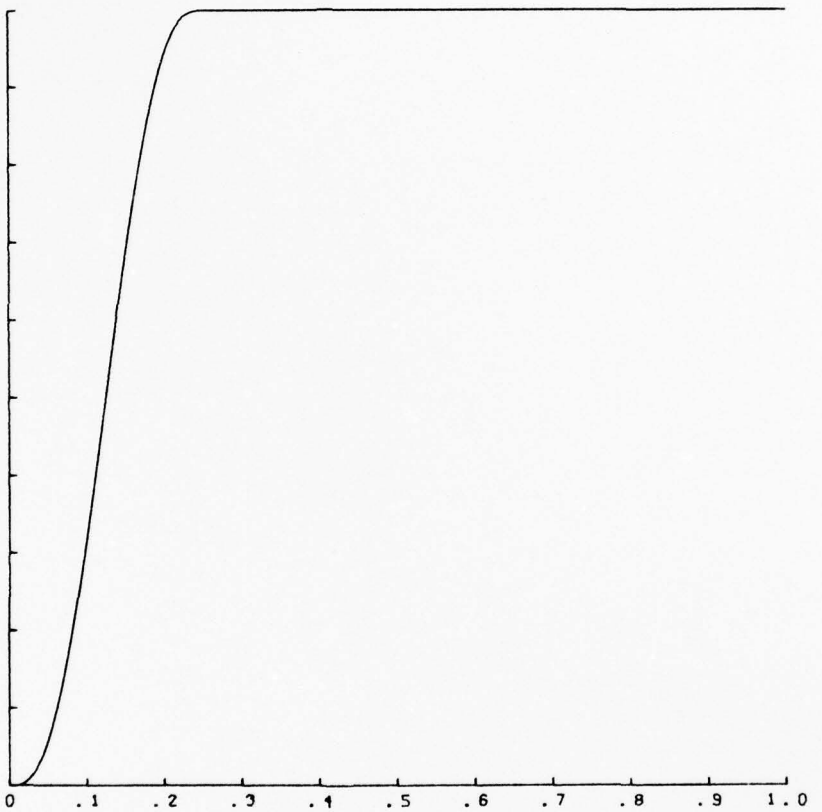


Fig. 3.3(5) Polynomial source function. $s(t) = \{[6(\frac{t}{T})^5 - 15(\frac{t}{T})^4 + 10(\frac{t}{T})^3][H(t)-H(t-T)] + H(t-T)\}$, $T = .25$

The inverse of the second transform is also easily found to be:

$$\frac{1}{T^3} L^{-1}\{\frac{1}{s}[\frac{12}{T^2s^2} - \frac{6}{Ts} + 1]\} = \frac{1}{T^3}[\frac{6t^2}{T^2} - \frac{6t}{T} - 1]$$

Thus

$$[i(t) * \frac{d}{dt} s(t)]_{\text{first term}} = \frac{60}{T^3}[(\frac{e^{-\eta t}}{b} \sin bt) * (\frac{6t^2}{T^2} - \frac{6t}{T} + 1)] \qquad 3.3\text{-}16$$

After several integration by parts schemes and some algebra we find for the inidividual terms

$$\frac{60}{T^3b}\int_0^t e^{-\eta\tau}\sin b\tau d\tau = \frac{60}{T^3b(\eta^2+b^2)}\{b-e^{-\eta t}A$$

$$\frac{360}{T^4b}\int_0^t e^{-\eta\tau}\sin b\tau\cdot(t-\tau)d\tau = \frac{360}{T^4b(\eta^2+b^2)}\{tb + \frac{\eta}{\eta^2+b^2}(b-e^{-\eta t}A) - \frac{b}{\eta^2+b^2}(+e^{-\eta t}B)\}$$

and,

$$\frac{360}{T^5b}\int_0^t e^{-\eta\tau}\sin b\tau\cdot(t-\tau)^2d\tau = \frac{360}{T^5b(\eta^2+b^2)}\{t^2b + \frac{2}{\eta^2+b^2}[te^{-\eta t}(2\eta A-bB) - 3b\eta t + \frac{2\eta b}{\eta^2+b^2}(\eta+e^{-\eta t}B) + (b-e^{-\eta t}A)]\}$$

where $A = \eta\sin bt + b\cos bt$

$B = b\sin bt - \eta\cos bt$

We may now add these terms to derive the solution to equation 3.3-15. The second half of the complete solution for $t > T$ may easily be written by substituting $(t-T)$ for t in the above three convolutions and changing the sign of the second.

The plot of the total solution to $i(t)*\frac{d}{dt}s(t)$ is seen in Figure 3.3(6).

Note that now there is a significant non-zero contribution to this curve between the two peaks corresponding to t = 0 and t = T. We shall see later that this property of this last source term has important ramifications when we begin to generate model accelerograms.

3.34 Comparison of the Source Terms

So far, as the various sources have been proposed, we have observed briefly their differences in the time domain. These differences are also meaningfully studied in the frequency domain.

If the same rise time is used for each source and if each is normalized so that all have an amplitude of one for $t \geq T$ we may evaluate their spectra and compare them. This is done graphically in Figure 3.3(7) for T - .25 second.

It may be seen immediately that the low frequency contribution of all the source terms falls off as 1/s with increasing frequency. Thus for frequencies in our model less than ~1/T the choice of source terms is unimportant. Indeed, for ground motions whose frequencies are below 1/T the simple Heaviside step function would serve as well as any of the more complex sources proposed. Thus, if we are attempting to match a displacement record where the dominant frequency content could very well be below 1/T for some reasonable rise time, any source here postulated will suffice.

However, as higher frequencies are approached the choice of source term becomes significant. Said another way, if we wish to distinguish between these various sources when modeling earthquake ground motion, we must look at motion with high enough frequency content relative to the

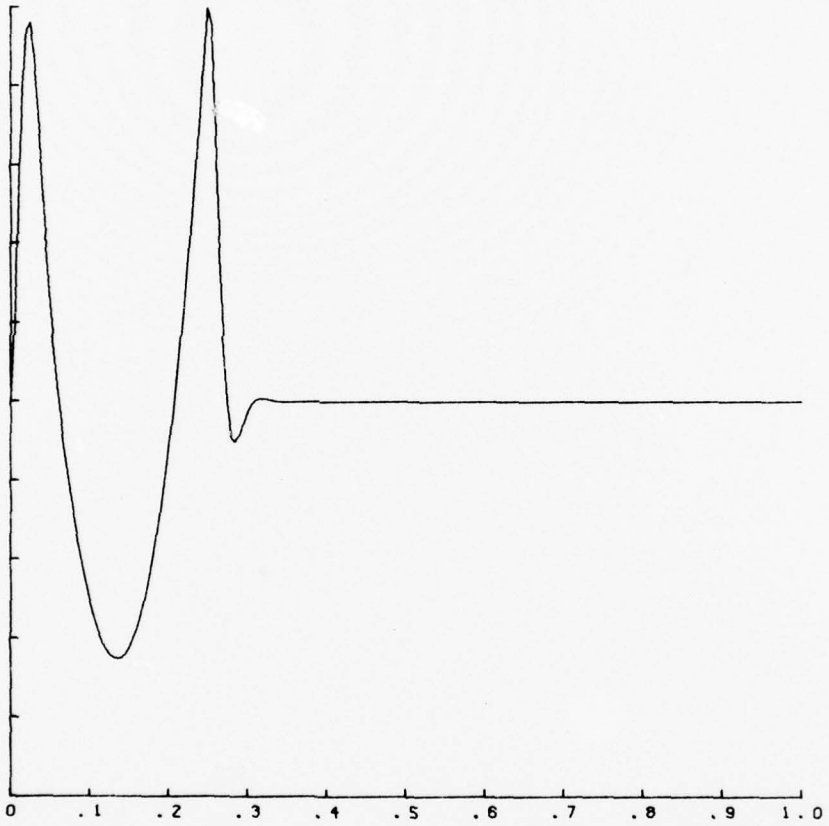


Fig. 3.3(6) $i(t)*\frac{d}{dt}s(t)$, T = .25 where s(t) is the source of Fig. 3.3(5)

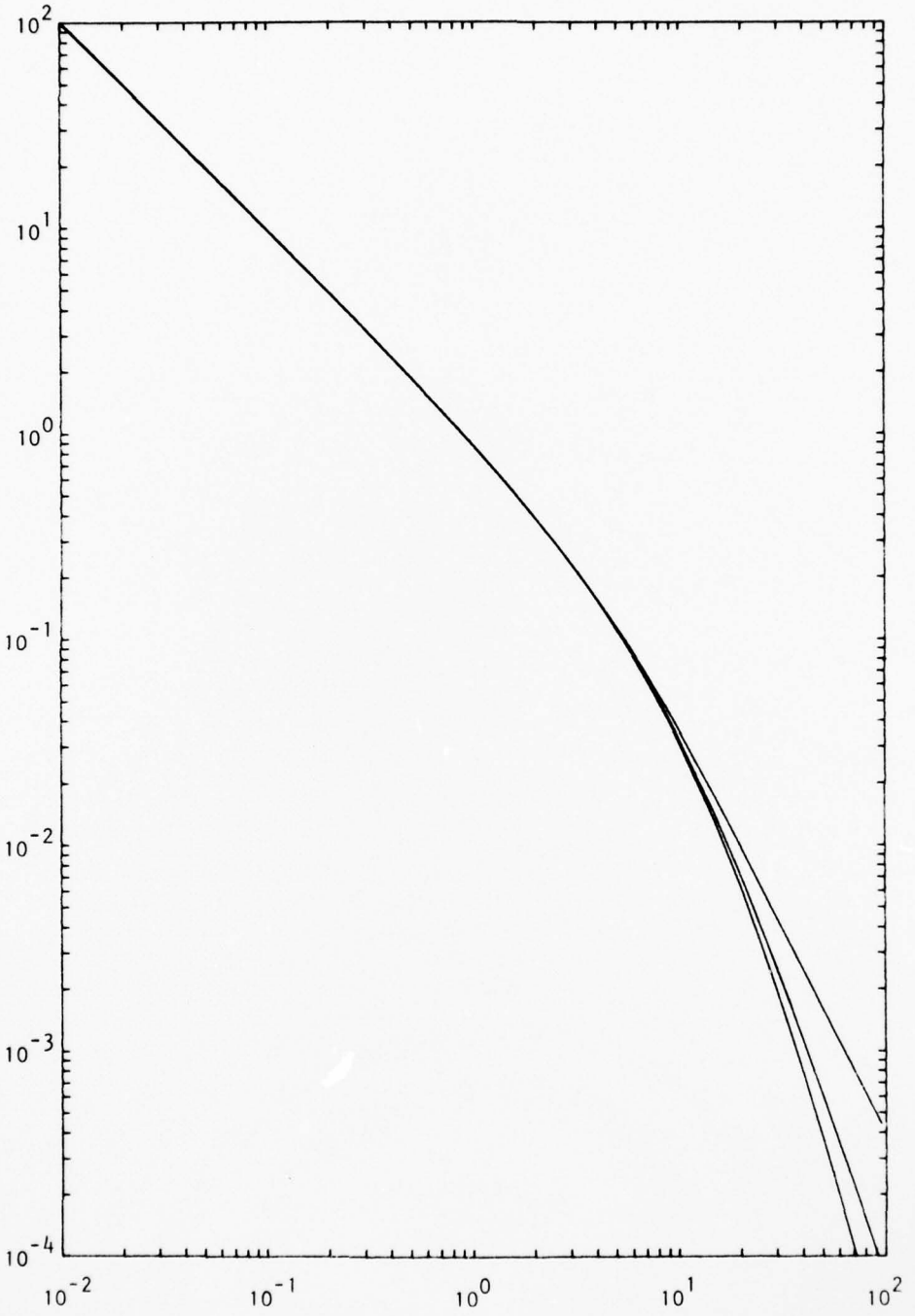


Fig. 3.3(7) Comparison of the spectra of the previous source terms. Again T = .25

rise time. Thus, if an accelerogram can be convincingly fitted, there is the additional benefit that the form of the source term may be more accurately determined. This could be important for problems such as determining theoretical near-field accelerations which are of great engineering significance.

3.4 Additional Parameters

There are three remaining parameters needed to define the model episode of faulting. As mentioned in the introduction to this chapter these are:

1) fault geometry,
2) fault propagation velocity, and
3) fault displacement amplitude.

All three of these parameters may be functions of position along the fault plane. The correct values of these variables are neither known, as are the constants of the Pacoima Dam accelerometer, nor amenable by arbitrary postulation to a small number of cases, as is the source time history term. However, we may see how each of these parameters of real faulting may be modeled by the use of line dislocation sources.

Suppose that we have selected appropriate P- and S-wave velocities in our half space. We wish to find the displacement at some surface point $\vec{u}(x,o,t)$ due to a point dislocation at (x',z',t'). The form of the Betti-Rayleigh representation theorum needed for the problem at hand is:

$$u_m(s,o,t) = \int_{-\infty}^{\infty} \int_{\Sigma} \nu_j \{[\sigma_{ij}](x',z',t')\, C_{ijpq}(x',z') \, G_{mp,q}(x,o,t;x',z',t')\, d\Sigma dt' \qquad 3.4\text{-}1$$

where Σ is the plane that will be identified with the fault surface, ν_j

is the unit vector perpendicular to Σ pointing from the positive to the negative side of the dislocation $[\xi_i]$ on Σ. Here $[\xi_i]$ is defined as:

$$[\xi_i] = \xi_i^+ - \xi_i^-$$

For the case of a thrust fault these quantities may be thought of as they appear in Figure 3.4(i).

From this figure we see that $\nu_2 = 0$. Let us further assume that the space in which the dislocation exists is homogeneous and isotropic. Then the elastic constants may be written as

$$C_{ijpq} = \lambda\delta_{ij}\,\delta_{pq} + \mu[\delta_{ip}\,\delta_{jq} + \delta_{iq}\,\delta_{jp}] \qquad 3.4\text{-}2$$

where λ and μ are Lamé's constants and the δ's are Kronecker delta functions as defined previously.

For m = 1 equation 3.4-2 then becomes:

$$\begin{aligned} u_1 = \int_{-\infty}^{\infty}\int_{\Sigma} \{&\nu_1([\xi_1]C_{11pq}G_{1p,q}) + \nu_3([\xi_1]C_{13pq}G_{1p,q}) \\ &+\nu_1([\xi_2]C_{21pq}G_{1p,q}) + \nu_3([\xi_2]C_{23pq}G_{1p,q}) \\ &+\nu_1([\xi_3]C_{31pq}G1p,q) + \nu_3([\xi_3]C_{33pq}G_{1p,q})\}d\Sigma dt' \end{aligned} \qquad 3.4\text{-}3$$

Where we have suppressed the functional notation and where, by the summation convention we have such identities as

$$\begin{aligned} \nu_1([\xi_1]C_{11pq}G_{1p,q}) = \nu_1[\xi_1]&C_{1111}G_{11,1} + C_{1112}G_{11,2} \\ &+ C_{1113}G_{11,3} + C_{1121}G_{12,1} + C_{1122}G_{12,2} \\ &+ C_{1123}G_{12,3} + C_{1131}G_{13,1} + C_{1132}G_{13,2} \\ &+ C_{1133}G_{13,3}) \end{aligned}$$

But for our problem $G_{11,2} = G_{12,1} = G_{12,2} = G_{12,3} = G_{13,2} = 0$ and from equation 3.4-2

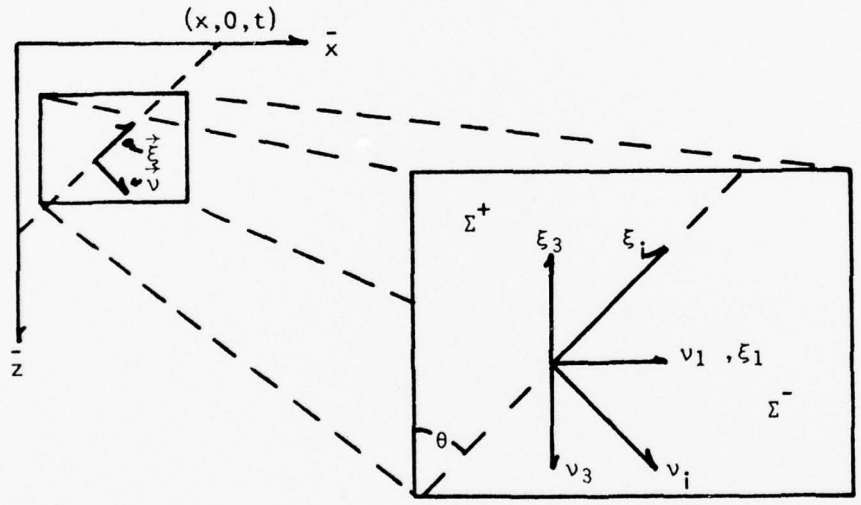


Fig. 3.4(1) Fault geometry parameters.

$$C_{1111} = \lambda + 2\mu$$

$$C_{1113} = C_{1131} = 0$$

$$C_{1133} = \lambda$$

Thus

$$\nu_1([\xi_1]C_{11pq}G_{1p,q}) = \nu_1[\xi_1]((\lambda+2\mu)G_{11,1} + \lambda G_{13,3})$$

and similarly

$$\nu_3([\xi_1]C_{13pq}G_{1p,q}) = \nu_1[\xi_1](\mu G_{11,3} + \mu G_{13,1})$$

$$\nu_1([\xi_3]C_{31pq}G_{1p,q}) = \nu_1[\xi_3](\mu G_{11,3} + \mu G_{13,1})$$

$$\nu_3([\xi_3]C_{33pq}G_{1p,q}) = \nu_3[\xi_3](\lambda G_{11,1} + (\lambda+2\mu)G_{13,3})$$

and since $[\xi_2] = 0$

$$\nu_1([\xi_2]C_{21pq}G_{1p,q}) = \nu_3([\xi_2]C_{23pq}G_{1p,q}) = 0$$

Substituting these relations into equation 3.4-3 and deriving similar expressions for u_3 we may write:

$$u_i(s,o,t) = \int_{-\infty}^{\infty} \int_{\Sigma} \{ \nu_1[\xi_1][(\lambda+2\mu)G_{i1,1} + \lambda G_{i3,3}]$$

$$+ \nu_3[\xi_1][\mu G_{i1,3} + \mu G_{i3,1})] + \nu_1[\xi_3][\mu G_{i1,3} + \mu G_{i3,1}]$$

$$+ \nu_3[\xi_3][\lambda G_{i1,1} + (\lambda+2\mu)G_{i3,3}]\} d\Sigma dt' \qquad 3.4\text{-}4$$

Now let us consider a point dislocation oriented in some direction $\hat{n}$. Then

$$[\xi_i] = \delta(x-x')\delta(z-z')\delta(t-t')\hat{n}$$

We will call $\hat{n}$ the direction of the fault plane at the point (x',z'). With θ as in Figure 3.4(1) we have:

$$\hat{n} = n_1\hat{x} + n_3\hat{z} = \sin\theta\hat{x} - \cos\theta\hat{z}$$

Now the expression for the point dislocation becomes

$$[\xi_i] = [\xi_1]\hat{x} + [\xi_3]\hat{z} =$$

$$\delta(x-x')\delta(z-z')\delta(t-t')\{\sin\theta\hat{x} - \cos\theta\hat{z}\}$$

Also from figure 3.4(1) we see that

$$\nu_1[\xi_1] = \frac{1}{2}\sin 2\theta[\delta(x-x')\delta(z-z')\delta(t-t')]$$

$$\nu_3[\xi_1] = \sin^2\theta[\delta(x-x')\delta(z-z')\delta(t-t')]$$

$$\nu_1[\xi_3] = -\cos^2\theta[\delta(x-x')\delta(z-z')\delta(t-t')]$$

$$\nu_3[\xi_3] = \frac{1}{2}\sin 2\theta[\delta(x-x')\delta(z-z')\delta(t-t')] = -\nu_1[\xi_1]$$

Substituting these expressions into equation 3.4-4 gives us the displacement at (x,o,t) due to a point dislocation of orientation $\hat{n}$ at (x',z',t'). We now have:

$$u_i(x,o,t) = \mu\{[\sin 2\theta G_{i1,1} - \cos 2\theta G_{i1,3}]$$

$$- [\sin 2\theta G_{i3,3} + \cos 2\theta G_{i3,1}]\} \qquad 3.4\text{-}5$$

where $G_{i1,3} = \frac{\partial}{\partial z'} G_{i1}(x,o,t;x',z',t')$

and similarly for the other terms. We have already calculated these quantities in Chapter 2.

The notation of equation 3.4-5 allows the remaining parameters of the model to be handled easily. That is, to represent a fault of whatever geometry we may string a series of point sources together. Under this scheme a simple planar fault would be represented by some number of point dislocation sources oriented so as to line up on the imaginary fault plane.

Once the fault geometry has been fixed the fault propagation velocity is easily modeled by delaying the origin time at each point in a prescribed manner. Thus, if uniform velocity is desired each successive point dislocation source would be made to rupture Δt seconds after

the one before. The smaller the velocity wished to be modeled the greater the Δt.

Finally, if we wish to model varying dislocation amplitude along the fault, it is a simple matter to scale individual point dislocations in a manner that will accomplish this.

The extreme flexibility of this method of modeling fault motion is at once apparent. Changes in various fault parameters are easily implemented. In the next chapter we will look at some model accelerograms based on various parameter values suggested by many other investigators.

Chapter 4

Comparison of Model and Actual Accelerograms

4.1 Introduction

In Chapter 1 were discussed several previous attempts to model the dynamic ground motion in the near-field of the San Fernando earthquake of February 9, 1971. It was noted that several improvements in the modeling procedure were now within reach. Primarily, an increase in the sophistication of the medium transfer function was deemed desireable and possible. All previous quantitative near-field dynamic studies have used the whole-space transfer function of Maruyama (1963) and Haskell (1969) to desribe the modification of the wave-form between the source and the point at which the ground motion was recorded. This mathematical idealization precludes the explicit consideration of waves whose existence depends upon more complex medium characteristics than those of a perfectly elastic, homogenerous, isotropic whole-space. It also makes analysis of model amplitudes uncertain. The development of a half-space medium transfer function was proposed as the most logical extension of this whole-space theory. Thus, in Chapter 2 the necessary ground work for such a formulation was carried out for the two-dimensional case using the method of Cagniard (1939) as modified by de Hoop (1960).

Secondly, as was seen in Chapter 3, several apparently minor modifications of the form of the source time history may have important ramifications to the high frequency content of the ground motion. Since the differences in these time histories become observable only at frequencies high relative to the inverse of the rise time, representations of ground motion that emphasize these high frequencies must be considered. The accelerograms written in the near field are ideal for this

purpose. In view of these considerations it was decided that the understanding of the seismic source could best be increased by the consideration of model accelerograms written in the near-field on the surface of a half-space.

The available records most ideally suited for a useful comparison of theoretical to observed near-field strong motion within the limitations imposed by the form of the mathematical development of Chapter 2 are those which were generated at Pacoima Dam during the San Fernando earthquake. In Section 4.2 we shall consider these records and the form into which they must be cast for the most direct comparison to the theoretical records to follow.

Having at last disposed of this preliminary work, generation of some actual model accelerograms may be done. This is undertaken in Section 4.3, first for single point dislocation sources by the proper combination of the separate elements considered in previous chapters, and then for a number of point dislocations taken together in such a way as to simulate propagating fault motions of various types. Accelerograms are generated using both a planar fault whose geometry relative to the Pacoima Dam station is essentially that of Canitez and Toksöz (1972) and a hinged fault similar to that of Turnbull and Battis (1973). A variety of fault rupture propagation velocities and source rise times are used in conjunction with the several forms of source time history explored in Chapter 3. Throughout Section 4.3 a discussion is presented of the implications of these model accelerograms as they are compared to each other and to the Pacoima Dam records.

Finally, in Section 4.4 is presented a fairly quantitative analysis of the uncertainties in the several model parameters chosen as best

achieving a satisfactory match between real and generated records within the limits of the method employed.

4.2 The Pacoima Dam Accelerograms

In this section we wish to consider the strong-motion record written at Pacoima Dam at the time of the San Fernando earthquake and how it may be modified to allow comparison to model accelerograms to be presented below. In Figure 4.2(1) these accelerograms are presented in their uncorrected form (Brady et al, 1971). As indicated in this figure the components shown are the correct ones of S15°W, N75°W, and Down and not S16°E, S74°W, and Down as originally reported (Trifunac, 1974). As will be the case whenever 15 seconds of time history are presented the abscissa scale is 0.5 sec/div. The ordinate scale, whose significance will vary from figure to figure, will be discussed in greater detail in Section 4.3. Here it is approximately 1.67 g/in.

As previously indicated, the mathematical development has been carried out only for a two-dimensional line source in a half-space. Such a formulation may naturally be expressed in terms of vertical displacements and displacements in the horizontal plane perpendicular to the line source. Since we wish to model the faulting history of the San Fernando earthquake by summing a series of such line sources lying in the plane of the idealized fault, theory dictates that the most straightforward horizontal direction to consider is that perpendicular to the strike of the fault. This strike is quite complicated in actuality but if generalized as the average trend of the fault zone it is approximately N70°W (Kahle, 1975). Thus, we wish to look at the S20°W component of horizontal ground motion at Pacoima Dam and since this does not conform to the actual disposition of the horizontal instruments some

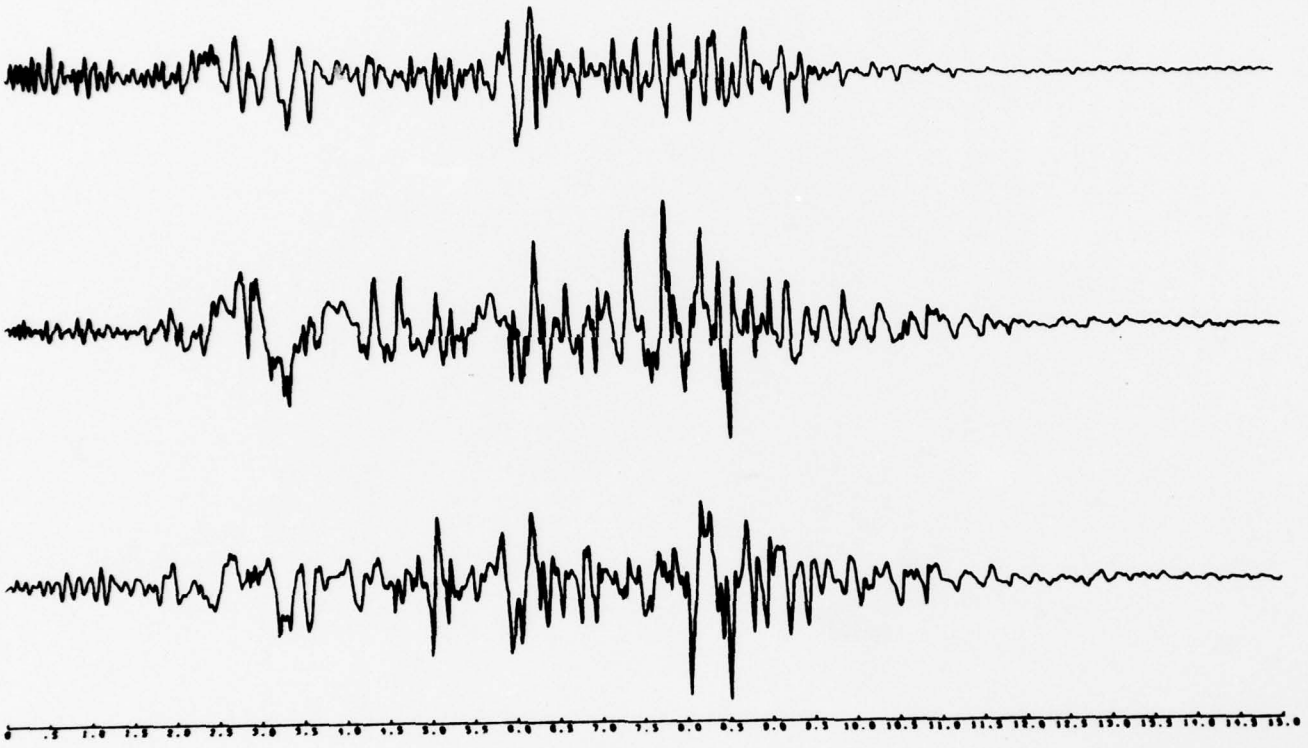


Fig. 4.2(1) Uncorrected Pacoima Dam accelerograms from the San Fernando earthquake of February 9, 1971. The ordinate scale is approximately 1.67 g/inch.

slight numerical resolution is necessary. The situation is summarized in Figure 4.2(2). Here the positive or up directions are shown for the horizontal components of the Pacoima Dam strong-motion instruments as well as for the horizontal component perpendicular to the general trend of the San Fernando earthquake fault zone. This is labeled U_1 in conformity with the theoretical development of previous chapters. As may be seen, U_1 and the S15°W Pacoima component are virtually the same, being separated by an angle, θ, of only 5°. Specifically

$$U_1(t) = S15°W(t)\cos\theta + N75°W(t)\sin\theta$$

To carry out the resolution implied by the above expression, it is necessary to interpolate the S15°W(t) and N75°W(t) time histories to their equal time interval equivalents or at least to interpolate one time history to the times of the other. Such a process inevitably has the effect of reducing the peak amplitudes. The magnitude of this reduction may be accurately estimated for approximately sinusoidal wave motions as a function of the ratio of the interpolation interval to the period of ground motion (Nigam and Jennings, 1968) but the problem becomes more complex when the ground motion is complex and the interpolation interval is not discreet but varies from point to point.

Since it was considered important not to degrade the peak acceleration value at Pacoima Dam it was decided to use the times of the S15°W component for the interpolation of the N75°W component. In this way, the peak value of 1.25 g that occurs on the S15°W component must survive the interpolation process without loss to round-off error. To estimate the error introduced by this procedure another interpolation using the N75°W times was carried out and a separate resolution done. The differences in the peak values of the components parallel and perpendicular to

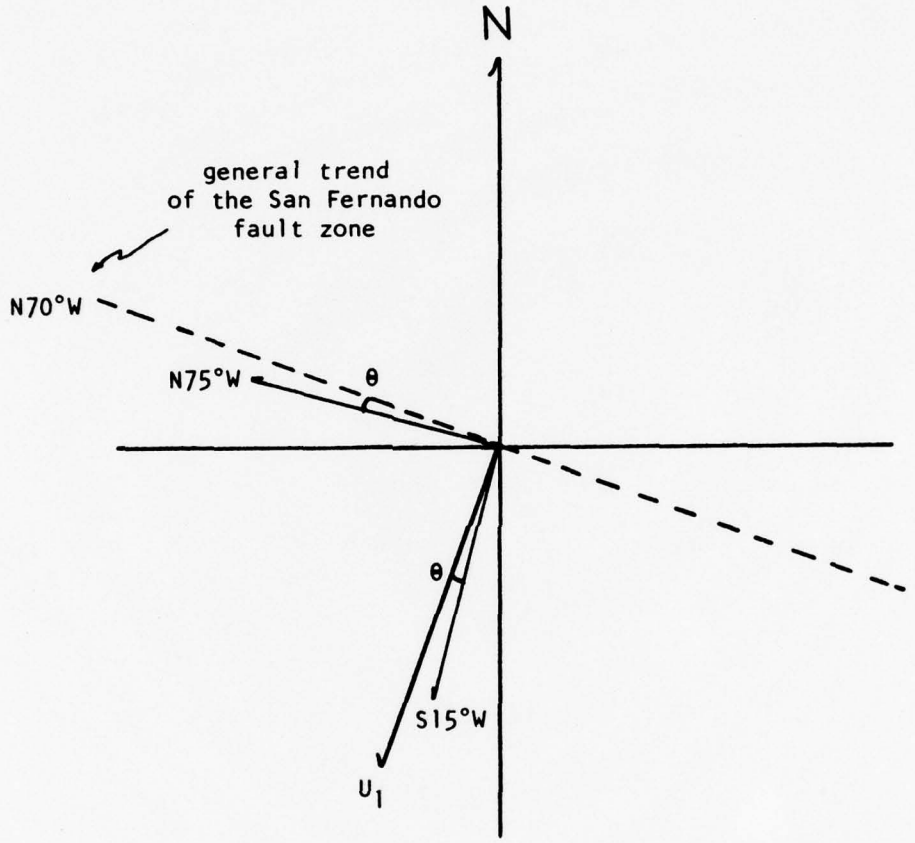


Fig. 4.2(2) Orientation of the general trend of the San Fernando fault zone relative to that of the Pacoima Dam horizontal strong-motion instruments.

the strike of the fault zone trend derived using these two methods indicate an introduction of error of less than 2 percent.

The three components--Down, U_1 and N70°W (parallel to and in the direction of the strike of the fault trend)--are shown in Figure 4.2(3). Interpolation using S15°W times was used in the generation of this figure. The abscissa and ordinate scales are the same as used in Figure 4.2(1). The positions of the horizontal traces on these plots have been interchanged. It is the top and bottom traces of Figure 4.2(3) that are to be reproduced by some faulting process model. They are hereinafter referred to as the Down and U_1 components of recorded acceleration at Pacoima Dam. These appear in Figure 4.2(4). The format of this figure will serve as the model for all subsequent figures in which the model equivalents of the Down and U_1 components are presented. The abscissa scale is 0.5 sec/div as in Figures 4.2(1) and 4.2(3). The ordinate scale is such that the maximum zero-to-peak acceleration is one linear inch in this figure. In this case, where the maximum acceleration is approximately 1.25 g, this implies an ordinate scale of 1.25 g/in.

Several useful pieces of information may be derived from a comparison of Figures 4.2(1) and 4.2(3). First, we may check the relative importance of resolution and interpolation since the center time history of 4.2(3) which is to be compared to the bottom time history of 4.2(1) has been properly resolved but has undergone no practical interpolation. The remaining horizontal record of Figure 4.2(3) has been both resolved and interpolated to significantly different times. As we would expect the effect of resolution over such a small rotation is very small. The effect of interpolation is somewhat greater but still is not important

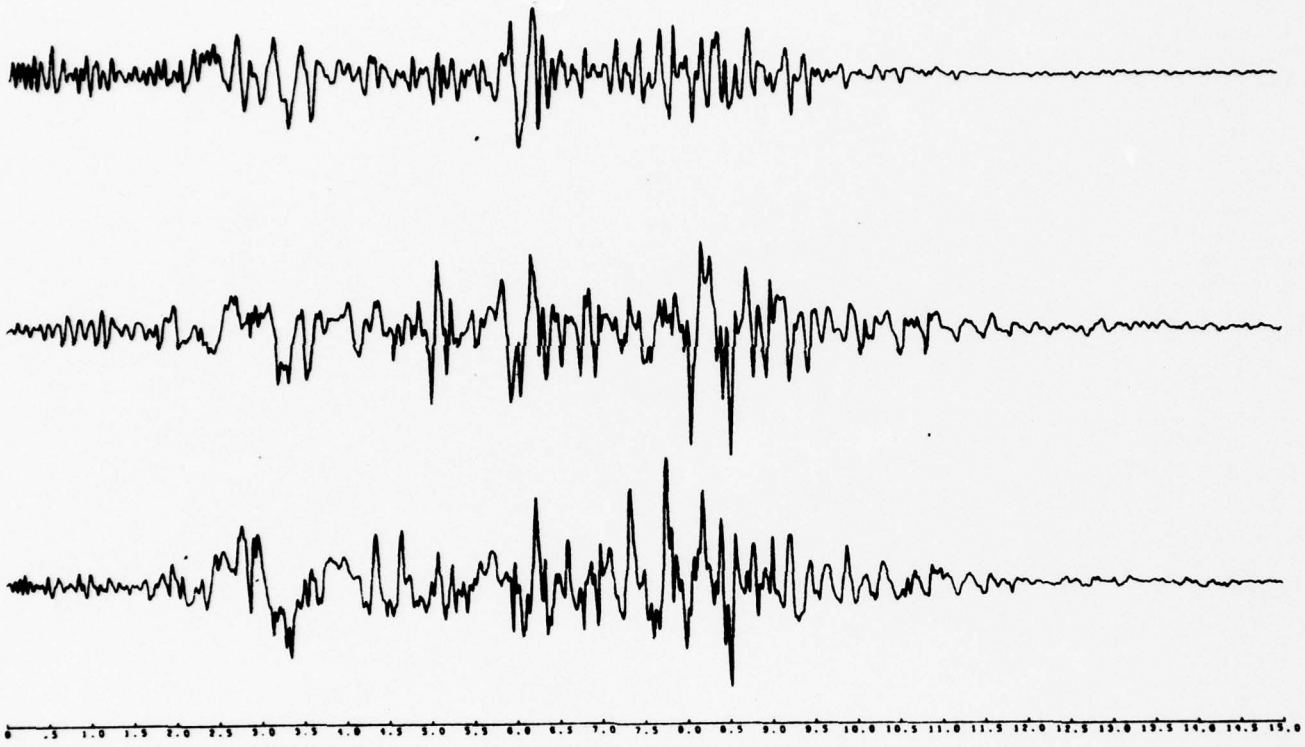


Fig. 4.2(3) Pacoima Dam accelerograms after directional resolution and temporal interpolation.

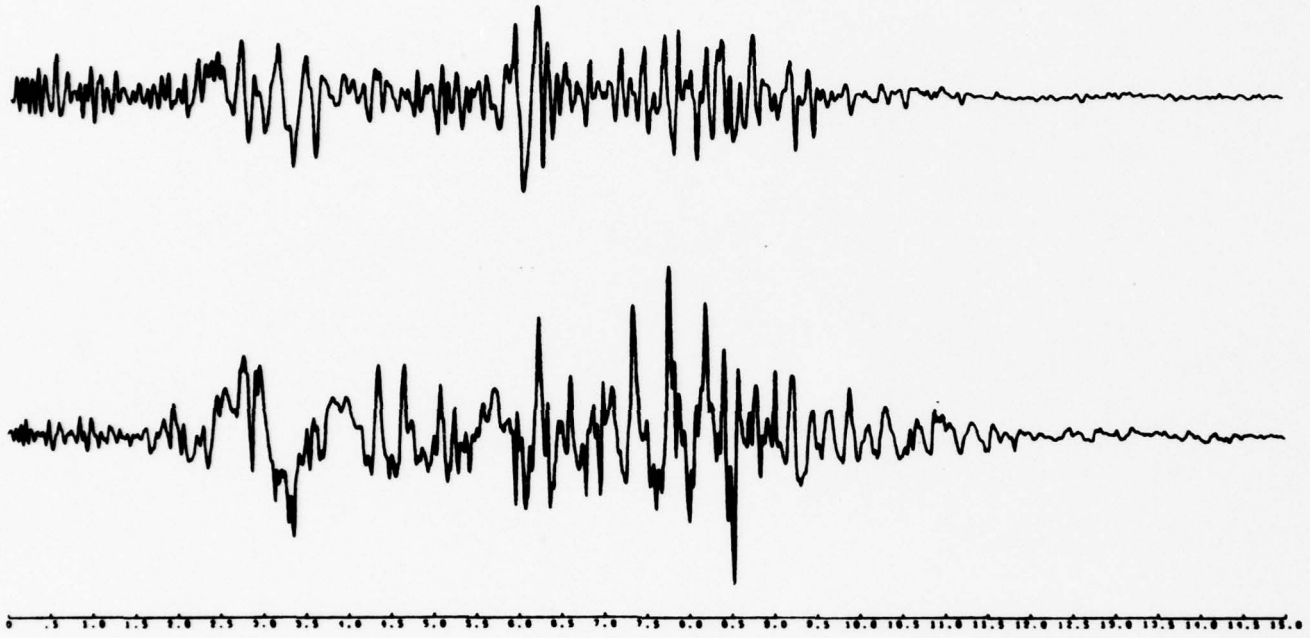


Fig. 4.2(4) Reproduction of the top and bottom traces of Fig. 4.2(3). These are the records with which all subsequent model accelerograms will be compared. The ordinate scale is approximately 1.25 g/inch.

for the purposes of this study. Secondly, there is significant ground motion in the direction parallel to the fault trace. The implication is that the faulting mechanism must have included a significant strike-slip component which we shall make no attempt to model in this study. This will have no effect on the model solution to the remaining two components presented in Figure 4.2(4). We may now generate some model accelerograms which may be directly compared to this figure.

4.3 Presentation of Model Accelerograms

All of the elements needed to construct a series of model accelerograms representative of those generated on the surface of a half-space due to a propagating fault have now been considered. It remains but to combine them in the proper way.

In Section 2.1 and, more specifically, in Section 3.4 we saw how to derive the surface motion due to a point dislocation of arbitrary orientation. The theory, which is developed for point forces whose time history is that of the Dirac delta function, $\delta(t)$, may be easily generalized to include other dislocation time histories as was shown in Section 3.3. Ultimately it is the combination of these point sources in quite elementary configurations that is to simulate the source of the desired record. Thus, it is worthwhile to begin by considering the record time history of a single point dislocation for a series of dislocation time histories. In this way those effects due primarily to the variation of source-time-history may be separated from those due to variation of fault geometry and fault propagation velocity.

In Figure 4.3(1) are presented the vertical and horizontal displacements $u_i(-1.38,0,t)$ due to a point dislocation at (0,2.5,0). The time history of this dislocation is that of the Heaviside unit step

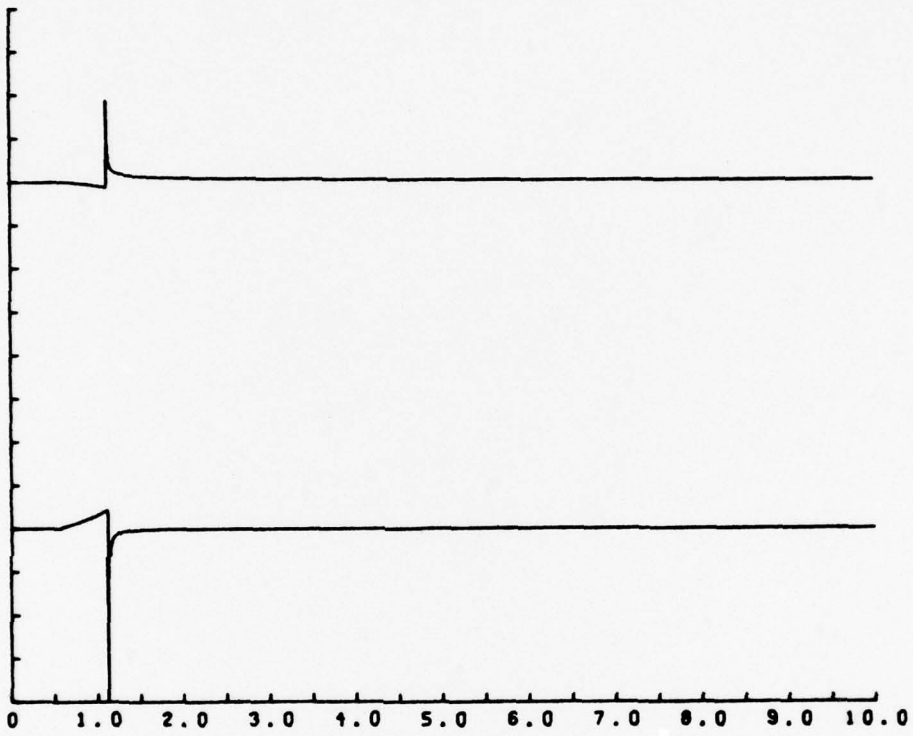


Fig. 4.3(1) Vertical and horizontal displacements at (-1.38,0,t) due to a point dislocation at (0,2.5,0). The time history of the dislocation is that of the Heaviside unit step function, H(t). For this figure the ordinate scale is 22.7 cm/division/m of dislocation/km of fault.

function, H(t). The seismic wave propagation velocities used are 5.58 km/sec and 2.90 km/sec for the compressional and shear waves, respectively. This compressional wave velocity is in substantial agreement with that employed in many previous studies such as Hanks, et al (1971), Hanks (1974), and Bolt and Gopalakrishnan (1975) to name but a few. The shear-wave velocity, however, is significantly lower than has been typically used. A more common value would be 3.2-3.3 km/sec as expected from the above P-wave velocity and the usual assumption that Poisson's ratio is 0.25. The lower S-wave velocity that has been used for this and all subsequent calculations is the result of a desire to consider a higher Poisson's ratio for shallow crustal rocks and to empirically better match the S-P interval of some early model fault rupture schemes relative to the observed S-P interval on the Pacoima records. A study of model accelerograms using shear-wave velocities of both 2.90 and 3.26 km/sec indicated that the shapes of the waveforms were not significantly affected by this velocity variation although S-phase arrival times obviously were affected.

There are several valid ways to present the ordinate. If we interpret the point nature of the source strictly so that the actual geometrical extent of the source is infinitesimal in the two-dimensional sense, the maximum displacement due to one meter of dislocation displacement at the source may be shown to be 9.10×10^{-4} cm at the above receiver location. This plot is constructed so that the maximum zero-to-peak amplitude is one inch or four scale divisions. In fact, all succeeding plots of ground, or more commonly, record amplitudes will follow this convention. Thus, on the interpretation that we wish the displacement of a geometrically infinitesimal source the ordinate scale

may be quoted as 2.27×10^{-4} cm/division/meter of source dislocation. This number is a little small for convenient quotation so another interpretation is worth considering. Let the source not be infinitesimal but extend over a finite width of dislocation surface of the same orientation. Then the effect of a dislocation of equal amplitude occurring over a strip of dislocation surface may be approximately modeled by multiplying the above amplitude by the width of the strip. Under this approximation, the ordinate scale of Figure 4.3(1) may be quoted as 2.27×10^{1} cm/division/meter of dislocation/km of fault width. We have referred to the width of a fault strip rather than to a unit fault area since this is a two-dimensional solution.

The most noteworthy aspect of the ground motion shown in Figure 4.3(1) is its unimpressive appearance. The only large amplitude arrival is that of the S-wave although the P-wave arrival is discernible. For this source-receiver geometry the Rayleigh-wave phase and any permanent ground offset are not significant relative to the body-phase amplitudes.

We are now in a position to investigate the effect of the convolution of this ground motion with various source-instrument terms. As previously shown, the source-instrument part of this convolution may be done analytically for a number of source time histories. Basically then, we shall be numerically convolving curves such as those shown in Figures 3.3(2), 3.3(4), and 3.3(6) with ground displacements such as those shown in Figure 4.3(1) to generate the instrumental records of an accelerometer with specified instrument constants at the specified receiver position due to a dislocation of specified time history and orientation at the specified source position. This is the only step in which a numerical rather than an analytical operation must be performed

to derive model accelerograms from a two-dimensional point source on the surface of an elastic half-space.

The source time histories considered are various forms of the finite ramp dislocation displacement function starting at zero amplitude at time t = 0 and stopping at unit amplitude at t = T, where T is the rise time. The differences between the three source time histories of Section 3.3 may be most meaningfully stated in terms of the smoothness with which they start and stop. The most elementary finite ramp is continuous for all time but has discontinuous first and second derivatives at t = 0 and t = T. The second finite ramp source is continuous for all time through its first derivative but has discontinuities in its second derivative at the usual points, t = 0 and t = T. Extending this progression logically, the final finite ramp source is continuous for all time through its second derivatives. For brevity, these source time histories will be referred to hereinafter as sources one, two, and three, respectively.

The instrument constants used are those of an accelerometer with $\eta = 68.49$ and $\omega_n = 120.86$ radians/sec, where η is the damping coefficient and ω_n the natural, undamped angular frequency. The static magnification used is 113.2 which corresponds to an acceleration sensitivity of 7.59 cm/g for the above value of ω_n. All these constants correspond to the average value of the equivalent constants of the three Pacoima Dam strong-motion instruments.

Experience has shown that a meaningfully complete set of record time histories may be generated by considering rise times of 0.1, 0.25, and 0.5 seconds for each of the three source time histories considered above. Thus, nine plots are necessary to adequately investigate the

effect of source time history variation on the accelerometer records pertinent to a given source-receiver geometry and dislocation orientation. For the specific source-receiver geometry and orientation of the ground motion of Figure 4.3(1) these nine accelerograms are presented in Figures 4.3(2) through 4.3(10). Figures 4.3(2) through 4.3(4) are the accelerograms using source one, Figures 4.3(5) through 4.3(7) are the accelerograms using source two, and Figures 4.3(8) through 4.3(10) are those using source three.

Several important observations may now be made from a comparison of these three sets of figures. The single ground displacement pulses at $t = r/\beta$ and, to a lesser extent, at $t = r/\alpha$ in Figure 4.3(1) have become double pulses separated by times equivalent to the appropriate source rise time. These two pulses may be thought of as the starting and stopping phases associated with the dislocation process at the source point. This pulse interval is obviously a sensitive barometer of source time history rise time for all sources considered.

In contrast, the general shapes of the individual pulses are greatly different for different source terms. The frequency content of the starting and stopping phases of source one is apparently unaffected by the rise time. For source two the impulsive nature of these two phases is still apparent but more rise time dependent motion is seen to occur between $t = r/c$ and $t = r/c + T$, where c is either the compressional or shear wave velocity. For source three the pulse width, as well as the pulse separation, is closely related to the rise time.

Finally, as shown in Figure 3.3(7), the less continuous the source the more high-frequency energy it contains. Therefore, we would expect higher amplitude accelerations to be associated with the less continuous

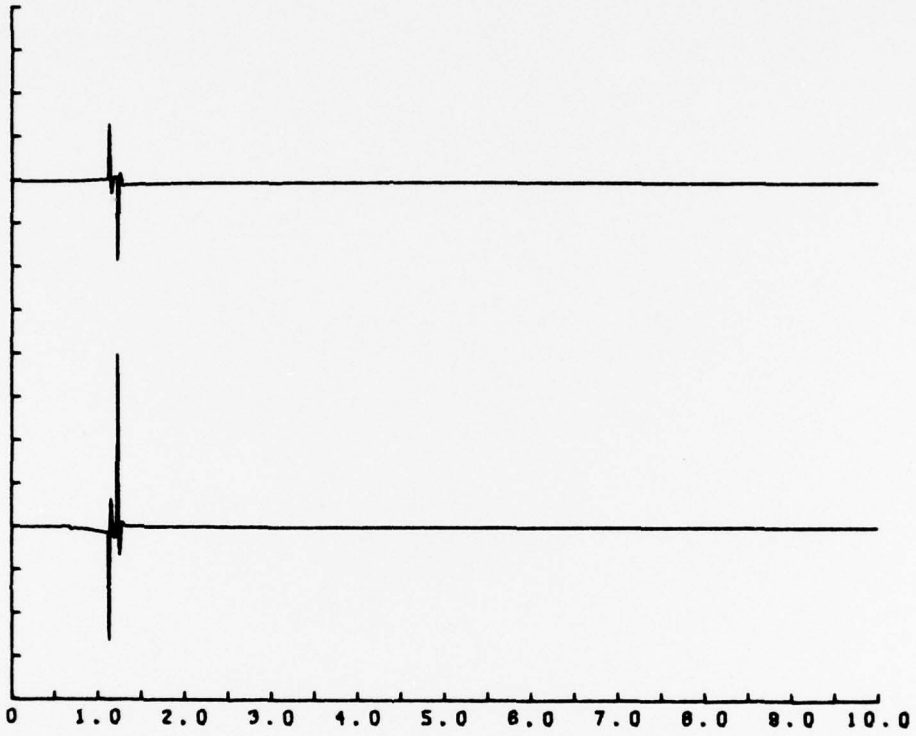


Fig. 4.3(2) Model accelerogram at (-1.38,0,t) due to a point dislocation at (0,2.5,0). The time history of the dislocation is that of a finite ramp (source one) with a rise time of 0.1 sec. The ordinate scale is 18.53 g/division/m of dislocation/km of fault.

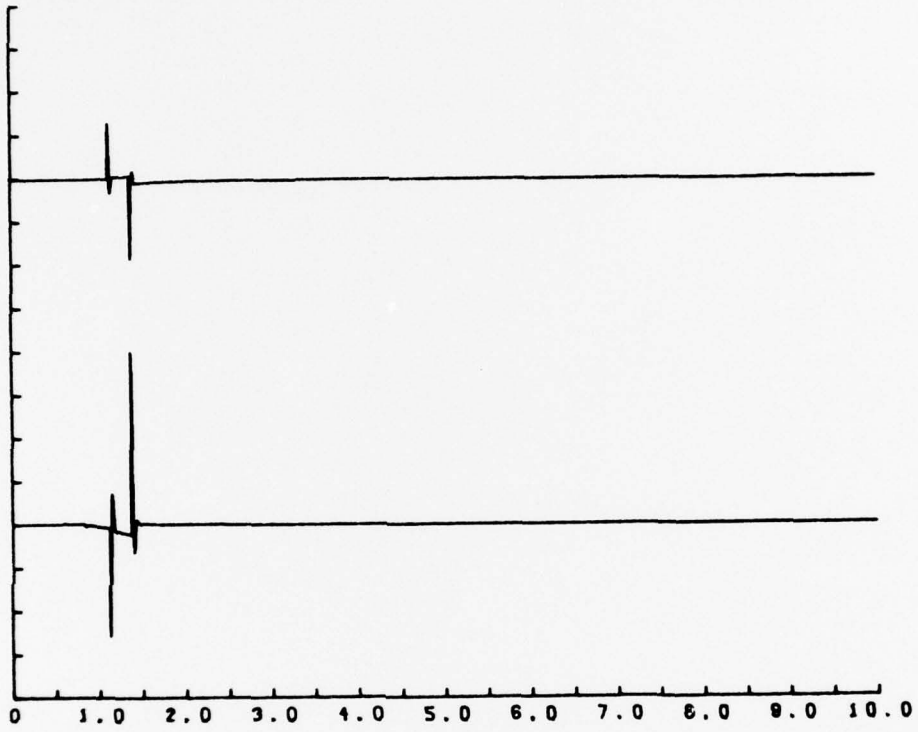


Fig. 4.3(3) Model accelerogram generated under conditions identical to those of Fig. 4.3(2) except now the rise time is 0.25 sec. The ordinate scale is 7.36 g/division/m of dislocation/km of fault.

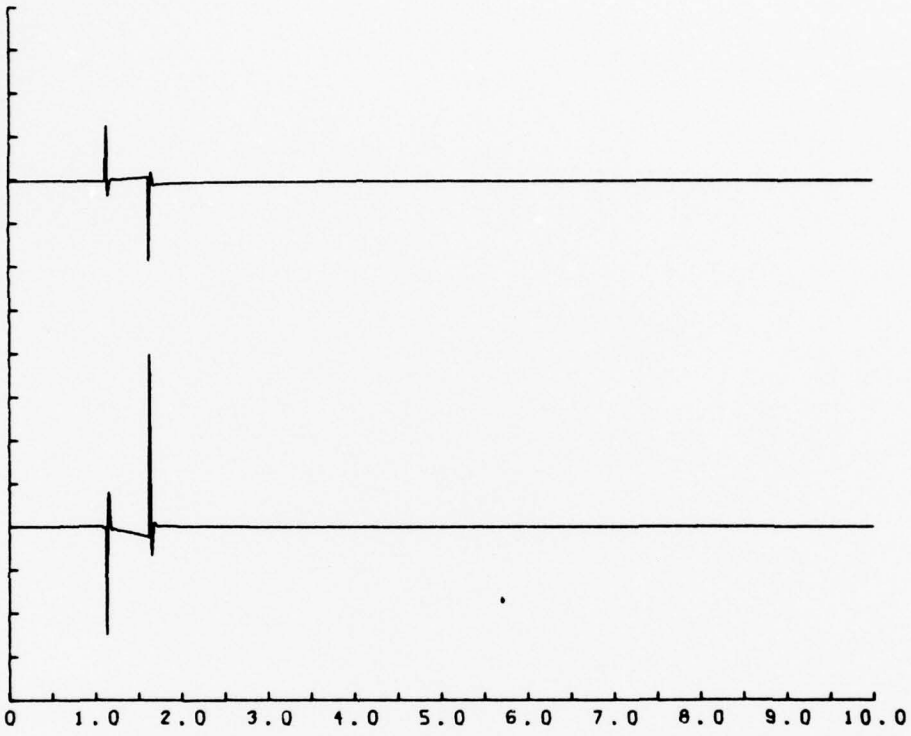


Fig. 4.3(4) Model accelerogram generated under conditions identical to those of Fig. 4.3(2) except now the rise time is 0.5 sec. The ordinate scale is 3.68 g/division/m of dislocation/km of fault.

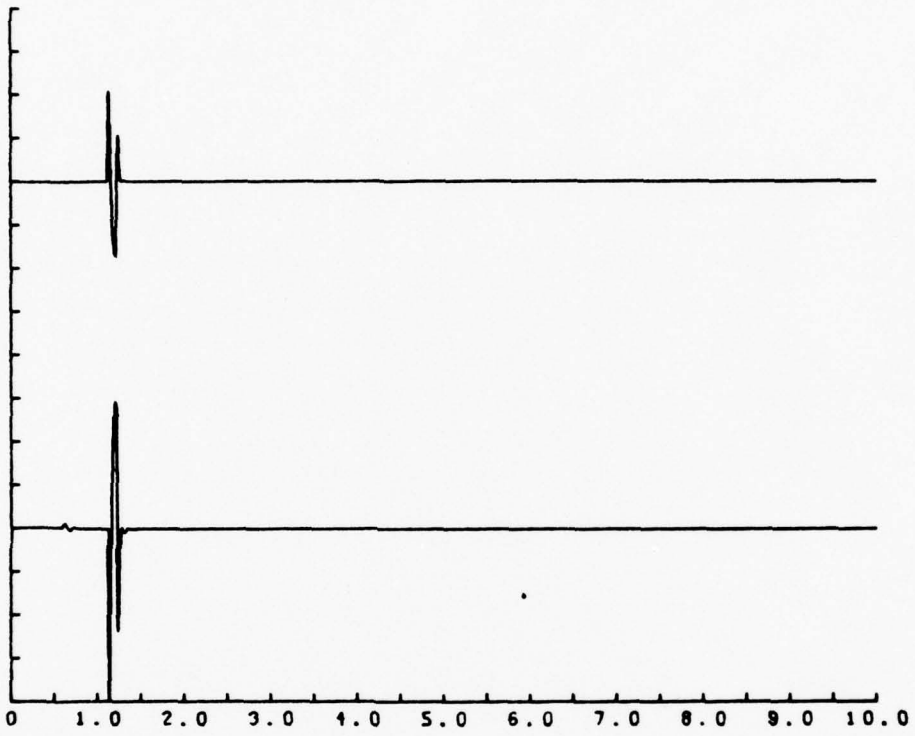


Fig. 4.3(5) Model accelerogram at (-1.38,0,t) due to a point dislocation at (0,2.5,0). The time history of the dislocation is that of a finite ramp with continuous first derivatives (source two). The rise time is 0.1 sec and the ordinate scale is 7.40 g/division/m of dislocation/km of fault.

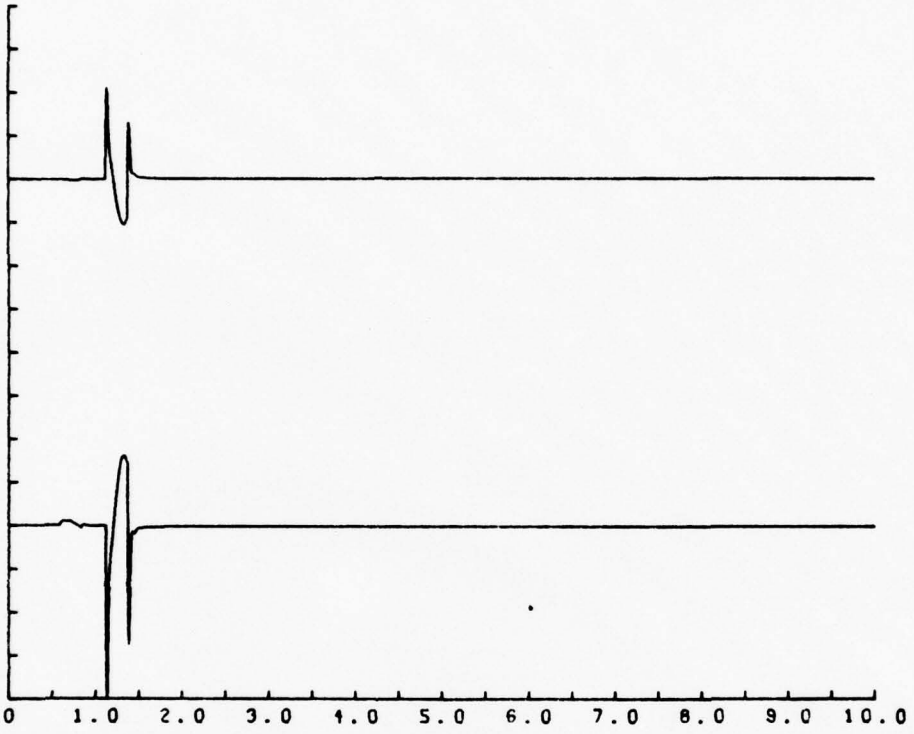


Fig. 4.3(6) Model accelerogram generated under conditions identical to those of Fig. 4.3(5) except now the rise time is 0.25 sec. The ordinate scale is 1.23 g/division/m of dislocation/km of fault.

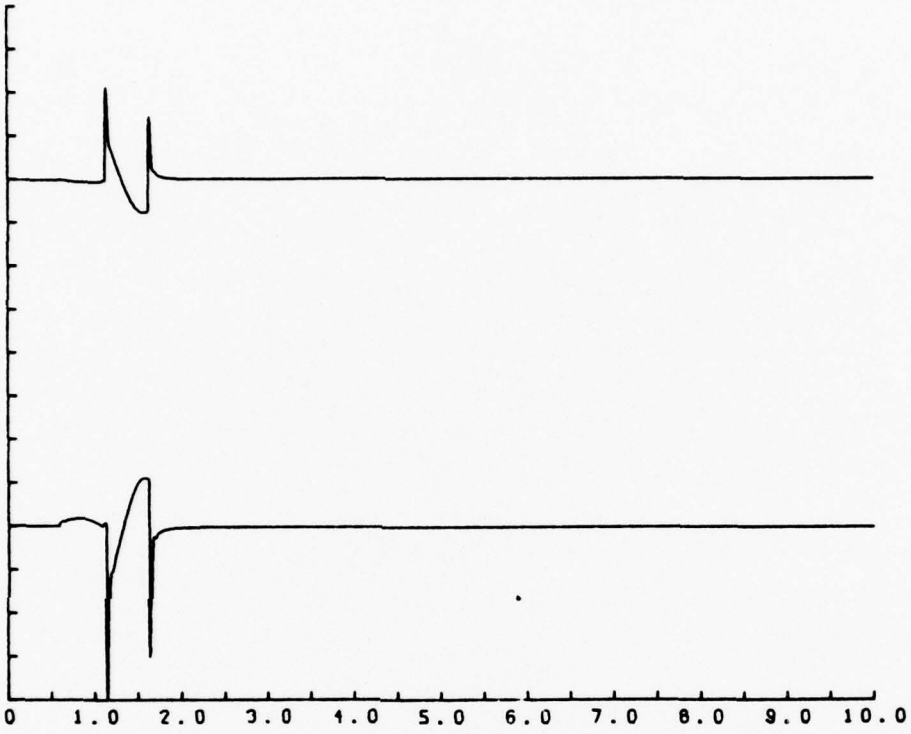


Fig. 4.3(7) Model accelerogram generated under conditions identical to those of Fig. 4.3(5) except now the rise time is 0.5 sec. The ordinante scale is 0.30 g/division/m of dislocation/km of fault.

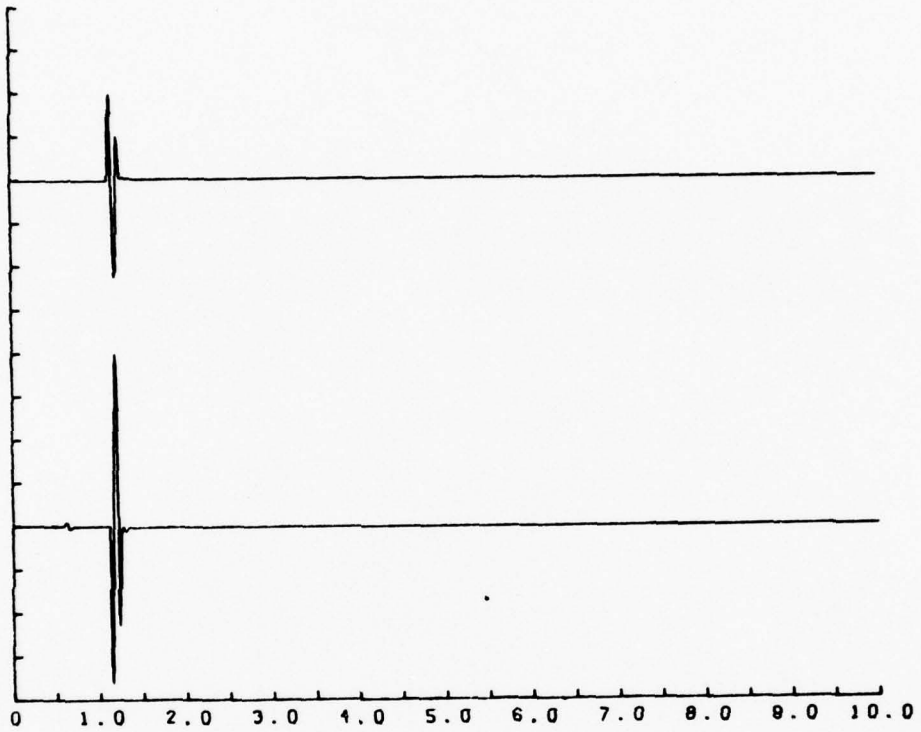


Fig. 4.3(8) Model accelerogram at (-1.38,0,t) due to a point dislocation at (0,2.5,0). The time history of the dislocation is that of a finite ramp with continuous first and second derivatives (source three). The rise time is 0.1 sec and the ordinate scale is 9.68 g/division/m of dislocation/km of fault.

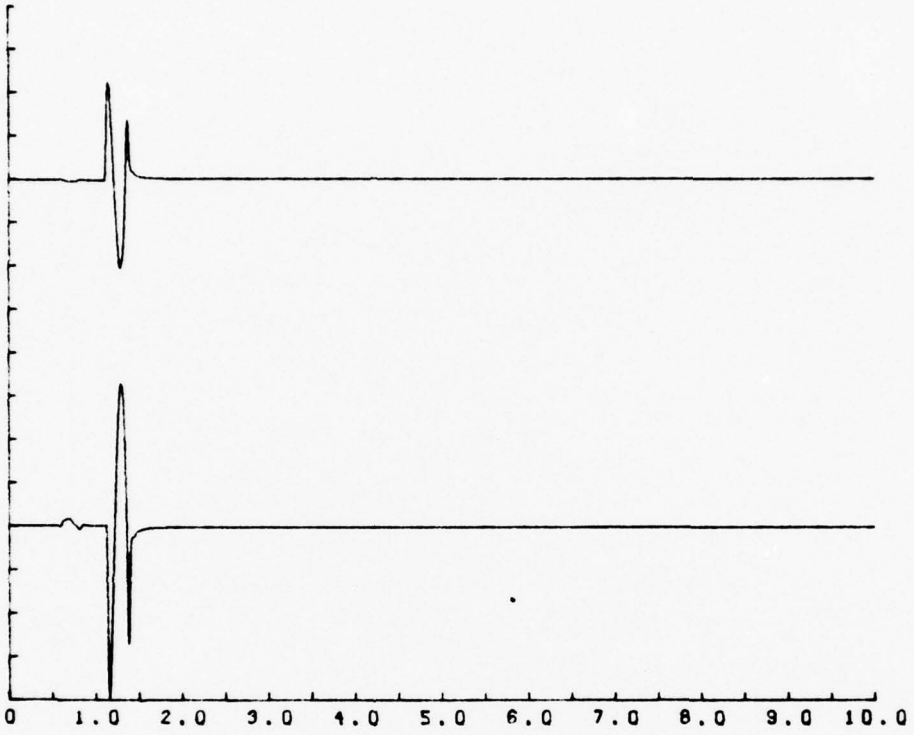


Fig. 4.3(9) Model accelerogram generated under conditions identical to those of Fig. 4.3(8) except now the rise time is 0.25 sec. The ordinate scale is 1.08 g/division/m of dislocation/km of fault.

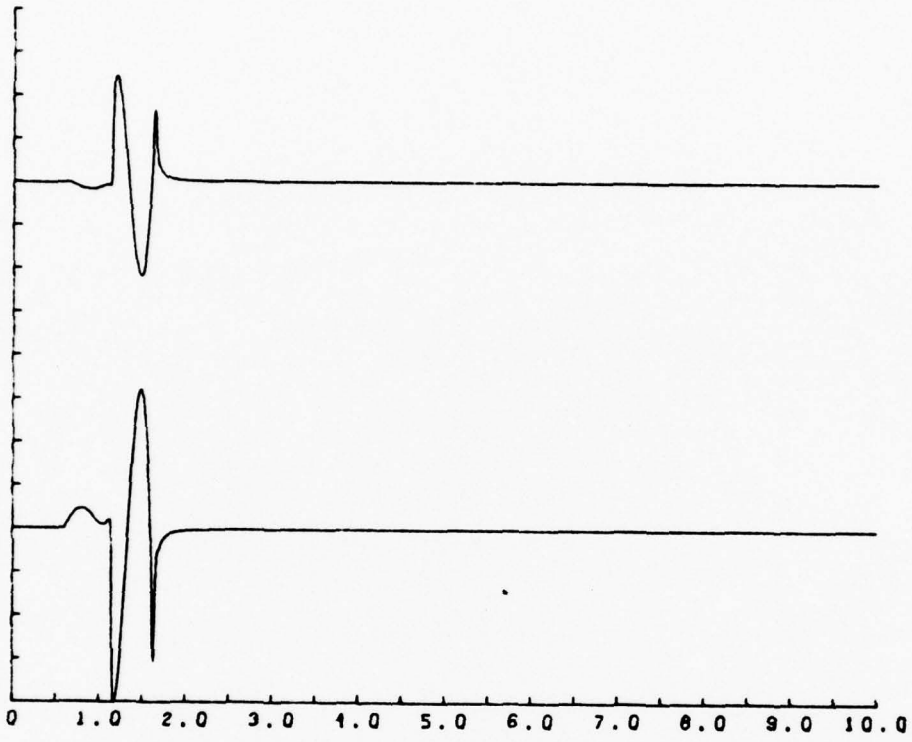


Fig. 4.3(10) Model accelerogram generated under conditions identical to those of Fig. 4.3(8) except now the rise time is 0.5 sec. The ordinate scale is 0.19 g/division/m of dislocation/km of fault.

sources, all other things being equal such as rise time and absolute dislocation amplitude. Similarly, since the corner frequency is inversely proportional to the rise time, T, for a given source, as was seen in Chapter 3, more high-frequency energy is present at smaller rise times. Both of these rather obvious contentions are amply supported by the maximum accelerations given in Figures 4.3(2) through 4.3(10). Again normalizing to those accelerograms given for one meter of dislocation over a one kilometer strip of fault we find peak accelerations of 14.7 g, 1.2 g, and .75 g for sources one, two, and three, respectively, using a rise time of T = 0.5 sec. And, normalizing in an identical way, we find peak accelerations of 38.6 g, 4.3 g, and again .75 g for source three using rise times of 0.1 sec, 0.25 sec, and 0.5 sec, respectively. It is clear from these figures that very large peak accelerations are deterministically obtainable from the formulation of the problem employed here if no mechanical constraint imposed by the allowable behavior of real elastic material is appealed to. It is also clear that, since the waveforms and their amplitudes may be derived independently by this method, peak acceleration amplitude will furnish a valuable cross check on the validity of any final solution. A model accelerogram that matches the Pacoima Dam resolved records of Figure 4.2(4) with respect to general appearance of the time history must also give reasonable peak acceleration values for reasonable dislocation amplitudes on the model fault surface.

We may now summarize the effect of varying the source dislocation time history. More continuous sources of greater rise time lead to accelerograms of lower frequency content and lower amplitude assuming that the dislocation amplitude and source-receiver geometry remain fixed.

As will be shown in the following sections these conclusions are also applicable to the sum of a series of such point sources combined in such a manner as to simulate propagation of a dislocation over a fault surface of arbitrary configuration.

4.31 Model Accelerograms from a Planar Fault

With three source functions, each specified for three rise times, it is easy to see that a completely unmanagable number of model accelerograms may be generated from a relatively few dislocation schemes. Practically, we can consider only a very few fault model geometries since the source-receiver geometry is the most fundamental parameter that must be considered. The evaluation of equation 3.4-5 for both components of ground displacement at two thousand time points requires approximately 12 seconds on the CDC 6400 computer. This number of time points allows generation of 10 seconds of ground motion time history at a time increment of 0.005 seconds. For the two basic fault models to be considered below two hundred line sources will be properly arrayed to simulate a continuous fault of the specified geometry. Thus, the computation of what may be termed the geometrical part of the solution involves computer evaluation of equation 3.4-5 eight hundred thousand times at an expenditure of almost forty minutes of CDC 6400 computer time. By contrast, computation that allows numerical convolution of this geometrical term with a given source-time-history/instrument term and which simulates fault propagation velocity variation requires generally less than one minute. It is clear that fault geometry is not well suited to solution by random experimentation.

Fortunately, fault geometry may be inferred from many types of data and consequently is one of the better determined of the problem

parameters. As was seen in Chapter 1 most early studies found that the data was adequately explained by a planar fault dipping at about 50°. Specifically, by analysis of the polarity of teleseismic P- and S-waves, of the spectra of surface waves, and of the static displacements, strains, and tilts in the source region, Canitez and Toksöz (1972) derived a model fault geometry similar in all essentials to that shown in Figure 4.3(11). Also shown is the position of the surface point at which acceleration records are to be calculated. Since this point is to represent the position of Pacoima Dam relative to the real fault surface it is so labeled in the figure. The distance between the zone of surface faulting of the San Fernando earthquake and the strong-motion instrument site at Pacoima Dam is an easily determinable quantity since it may be measured directly. From Kamb, et al (1971) this distance is slightly in excess of 5 kilometers. The equivalent distance in Figure 4.3(11) is a little greater than this because it was originally defined to be one-half the distance between the epicenter and surface fault rupture of a planar fault originating at a depth of 14 kilometers and dipping at 52° to the horizontal. Defined in this way the pertinent distance becomes 5.47 kilometers.

To model the ground motion at Pacoima Dam due to a motion along the entire fault, the ground motion from individual sources along the fault plane are calculated and summed. Thus, the next step is to carry out these calculations and store them for later summation. As mentioned above it was decided somewhat arbitrarily to model the fault using two hundred two-dimensional point sources evenly distributed over its surface because it was found empirically that this spacing of individual sources allowed the generation of model accelerograms whose appearance

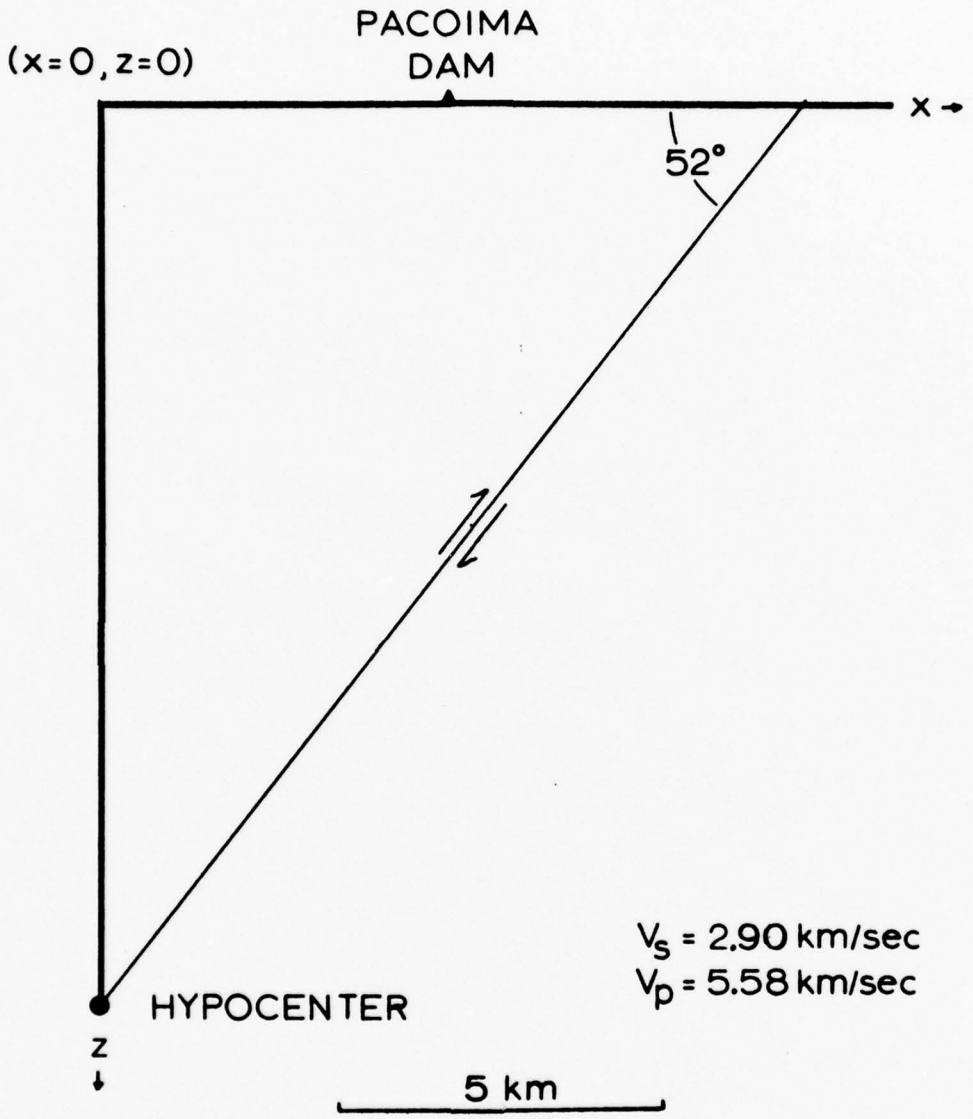


Fig. 4.3(11) Planar model of the fault associated with the San Fernando earthquake of February 9, 1971 (after Canitez and Toksöz, 1972). The hypocenter of the earthquake is at the lower end of the fault. The sense of fault motion, the relative position of Pacoima Dam, and the seismic velocities used in subsequent accelerograms are also shown.

did not depend upon any reasonable change in the interval between sources. These accelerograms could, thus, be considered more a property of the fault model than of the particular method of evaluation. The ground motion at the receiver is then stored on magnetic tape for each source point and for both components so that the numerical equivalent of two hundred figures similar to Figure 4.3(1) are now available.

The summation of these two hundred ground motions is now desired in such a way as to simulate propagation of the dislocation episode along the fault. It is obvious that this may be done quite simply for certain discrete values of fault propagation velocity. For example, let the fault length be L and the incremental length between point sources along the fault be $\Delta\ell$. From the above requirement that there be two hundred of these point sources we see that $\Delta\ell = L/200$. Further, let the displacement at Pacoima Dam at time t due to source j be $U_j(t)$ where U may be either the horizontal or vertical component of ground motion. Now assume that the $(j+1)^{th}$ source begins at Δt seconds later where Δt is the time increment at which ground and record motions have been calculated. From above $\Delta t = 0.005$ seconds. The combined ground motion at the receiver is then $U_j(t+\Delta t) = U_{j+1}(t)$. This process effectively models a fault propagation velocity of $\Delta\ell/\Delta t$ or, for the geometry of Figure 4.3(11), a velocity of 17.77 km/sec. This is the largest finite velocity obtainable from the above incremental process which may be represented by the following series of equations:

$$U(0) = U_1(0)$$

$$U(\Delta t) = U_1(\Delta t) + U_2(0)$$

$$U(2\Delta t) = U_1(2\Delta t) + U_2(\Delta t) + U_3(0)$$

$$U(3\Delta t) = U_1(3\Delta t) + U_2(2\Delta t) + U_3(\Delta t) + U_4(0) \qquad 4.3\text{-}1$$

In these expressions the time incremental nature of the evaluation of displacement time history has been made explicit. Slower fault propagation velocities may be modeled by allowing multiple values of the time increment between source points. In this case the fault propagation velocity is $\Delta\ell/n\Delta t$, n = 2,3,4.... For example, with n = 2 we have a propagation velocity of 8.88 km/sec and, in analogy to equation set 4.3-1

$$U(0) = U_1(0)$$

$$U(\Delta t) = U_1(\Delta t)$$

$$U(2\Delta t) = U_1(2\Delta t) + U_2(0)$$

$$U(3\Delta t) = U_1(3\Delta t) + U_2(\Delta t)$$

$$U(4\Delta t) = U_1(4\Delta t) + U_2(2\Delta t) + U_3(0) \qquad 4.3\text{-}2$$

The method now is to retrieve the individual source time histories from the magnetic tape and sum them as indicated in equation sets 4.3-1 or 4.3-2 or their equivalent for some other value of n. This sum now represents the ground displacement at Pacoima Dam due to two hundred point sources of infinitesimal geometric extent evenly distributed over the fault surface of Figure 4.3(11) and whose time history of dislocation is that of a Heaviside unit step function propagating over the fault surface at a velocity of $\Delta\ell/n\Delta t$. It remains but to convolve this summed ground motion with the various source-time-history/instrument terms discussed in Chapter 3 and used to generate accelerograms 4.3(2) through 4.3(10). Since convolution of the sum of a series of functions is distributive we need only convolve the above sum with an appropriate source-instrument term to derive an accelerogram identical to that generated by the summation of individual point source accelerograms. This, of course,

saves a great deal of time and expense.

Previous dynamic studies (Mikumo, 1973; Trifunac, 1974; Bolt, 1972; Hanks, 1974; Turnbull and Battis, 1973) have generally indicated fault rupture propagation velocities of between 2.0 and 3.0 km/sec. Therefore, it was decided to put most emphasis on this range of values. In fact, preliminary efforts of this study were suggestive of velocities in the lower half of this range. Thus, three values were used. These were 2.538 km/sec, 2.221 km/sec, and 1.974 km/sec as dictated by the incremental considerations above.

An exhaustive use of all the variables considered would entail the generation of twenty-seven model accelerograms for each model fault geometry. This was, in fact, not necessary since it was discovered quite early that the effect of fault propagation velocity was not significant in altering those features of an accelerogram which might be characterized as general frequency content. Thus, if a model accelerogram did not "look like" the Pacoima record because of a difference in predominant period of significant phases the alteration of the propagation velocity would, in general, not improve or degrade the match. This will become clear when later figures are compared representing model accelerograms whose sources differ only in propagation velocity.

We are now in a position to present some model accelerograms. Beginning with the most simple cases in Figures 4.3(12) through 4.3(14) are presented the model accelerograms for the Canitez-Toksöz fault geometry, a truncated ramp source-instrument term (type one source) and a fault rupture propagation velocity of 1.974 km/sec. The source rise times are 0.1, 0.25, and 0.5 seconds, respectively. The significance of the ordinate scale is similar to that of Figures 4.3(2) through

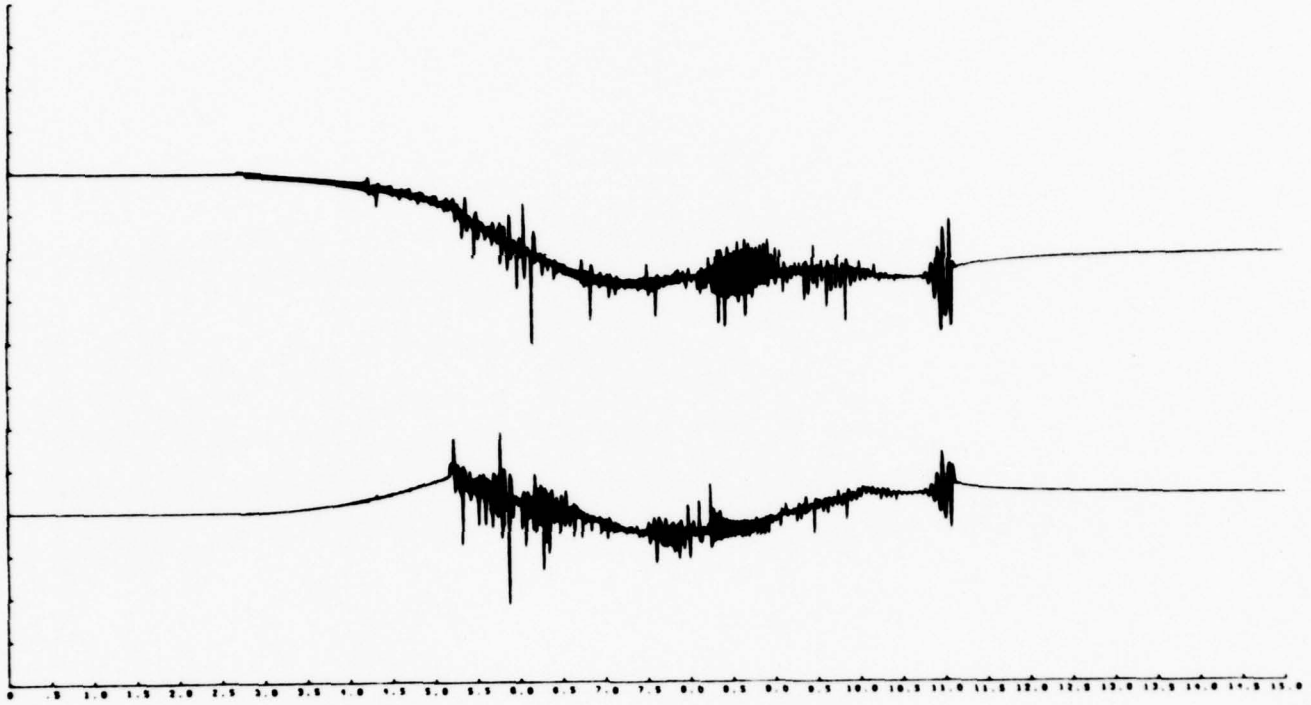


Fig. 4.3(12) Model accelerogram generated using the fault geometry of Fig. 4.3(11) and the source-instrument term of Fig. 3.3(2) (source one) with a rise time of 0.1 sec. Fault rupture begins at the hypocenter and propagates along the fault at 1.974 km/sec. The ordinate scale is 8.81 g/division/m of dislocation.

BEST AVAILABLE COPY

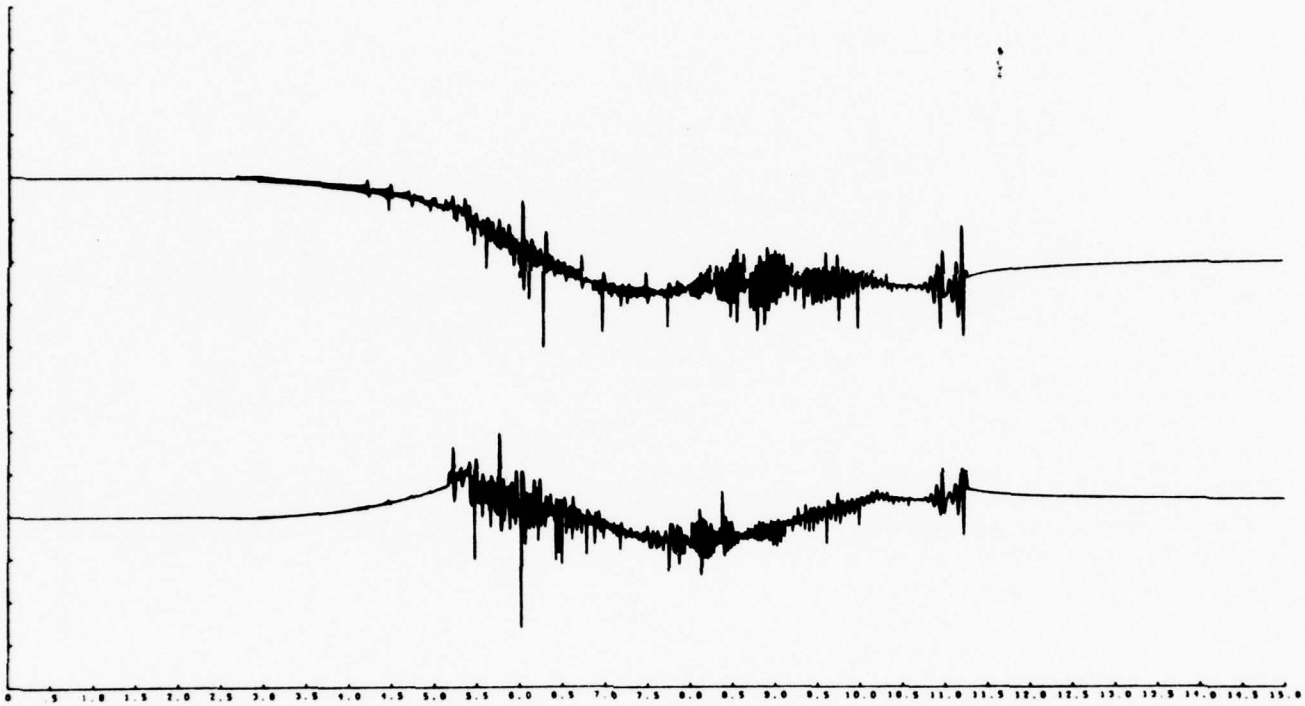


Fig. 4.3(13) Model accelerogram generated under conditions identical to those of Fig. 4.3(12) except now the rise time is 0.25 sec. The ordinate scale is 3.42 g/division/m of dislocation.

BEST AVAILABLE COPY

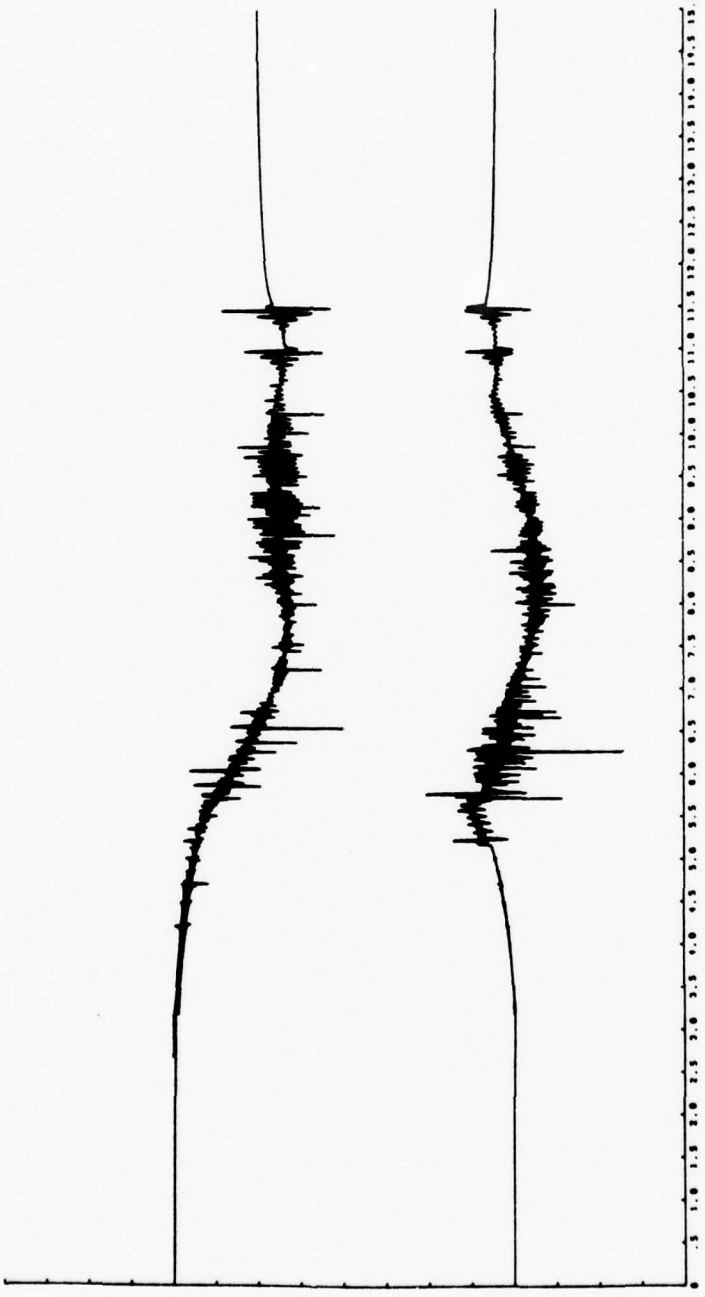


Fig. 4.3(14) Model accelerogram generated under conditions identical to those of Fig. 4.3(12) except now the rise time is 0.5 sec. The ordinate scale is 1.73 g/division/m of dislocation.

BEST AVAILABLE COPY

4.3(10). Each point source is thought of as acting over a segment of the fault whose width is $\Delta\ell$. With this assumption we may quote the ordinate scale in terms of centimeters of record displacement/division/meter of dislocation along the entire fault. We have, of course, as yet not considered the effect of allowing dislocation amplitude to vary with position on the fault. Alternatively, since the static magnification of the instrument used to derive expressions for the source-instrument term is such that the acceleration sensitivity is 7.59 centimeters of record displacement/g of ground acceleration (where g is, as usual, the acceleration of gravity) we may express the ordinate scale in terms of g's/division/meter of dislocation along the fault. It is this second convention that will be followed throughout the remainder of this study. Thus, the ordinate scales of Figures 4.3(12) through 4.3(14) are 8.81, 3.42, and 1.73 g's/division/meter of fault displacement, respectively.

The similarity of these first three model accelerograms to the Pacoima records as presented in Figure 4.2(4) is disappointing in many respects. First as might have been anticipated from the single point source accelerograms of Figures 4.3(2) through 4.3(4) which employed the same source-instrument term, the frequency content of these model accelerograms is much too high compared to that of the Pacoima records. The pulse width of each individual spike of acceleration is simply not adequate to allow constructive or destructive interference to be noticeable when the motions of two hundred sources are superposed in the prescribed manner. Secondly, the constraint imposed on the magnitude of fault dislocation by these accelerograms is unacceptable. If these peak values of acceleration are to match the approximately 1.25 g value of the Pacoima maximum acceleration, fault dislocations over the entire

dislocation surface of 0.04, 0.09, and 0.18 meters are implied for rise times of 0.1, 0.25, and 0.5 sec, respectively. These derived values of average dislocation amplitude are far too small as may be seen from previously derived estimates for this quantity as presented in Table 1-1. Finally, it is obvious that some long period noise has entered the calculation during the numerical convolution of the source-instrument term with the ground displacement term. It is intuitively unacceptable to have a model accelerogram with a final constant step in acceleration. After the last wave from the faulting process has passed the receiver position all acceleration must return to zero.

In spite of these shortcomings the accelerograms of Figures 4.3(12) through 4.3(14) are not completely devoid of interest. It can be seen, for example, that using the 1.974 km/sec fault propagation velocity of these particular model accelerograms a total record of approximately 8.5 sec is written between the arrival of the first P-wave at 2.7 sec and that of the last surface wave at about 11.2 sec. Thus using similar fault propagation velocities and fault model geometries we may have reasonable hopes of modeling about 8 sec of the actual Pacoima record without recourse to more complicated medium transfer functions or dislocation time history. It may also be seen that surface waves are quite apparent on all records and that their peak amplitudes are about as large as those of earlier body-wave phases. The importance of surface waves to near-field accelerograms has often been discounted since their prominence at teleseismic distances is due to their less rapid geometric attenuation relative to body waves. Here we see, however, that where the fault rupture actually approaches the surface of the earth these surface waves are likely to play an important role in near-field ground

motions. One other feature of these very preliminary accelerograms is worthy of note. That is, the duplication of pulses at t = r/c and t = r/c + T observed before in connection with the single point source accelerograms has survived the superposition process. This is particularly evident for the surface wave train near the end of these records but may also be seen for earlier body-wave pulse pairs. This phenomenon may be very useful in determining the proper rise time to use if suitable distinct pulse pairs may be observed in the real record.

We have yet to explore the effect of variation of the propagation velocity of the dislocation along the fault. In view of the disagreeable aspects of the accelerograms in Figures 4.3(12) through 4.3(14) we will defer this more complete exploration of all the parameters available to a given geometry until a more satisfactory source-instrument term is employed. We now undertake this task using source two.

Figures 4.3(15) through 4.3(23) represent all possible combinations of the three rise times T = 0.1, 0.25, and 0.5 sec with the three fault rupture propagation velocities 2.538, 2.221, and 1.974 km/sec using source two and the planar fault geometry of Figure 4.3(11). These particular velocities are dictated by the discrete nature of the problem formulation as we have already seen. Let us begin by considering the three model accelerograms associated with the fastest propagation velocity--2.538 km/sec. These appear in Figures 4.3(15) through 4.3(17) for rise times of 0.1, 0.25, and 0.5 sec, respectively.

Many of the features evident in these accelerograms are the logical extensions of their source one counterparts as presented in the previous three figures. For example, the S-P interval of approximately 2.5 sec has not changed since this is a function only of the hypocenter-

BEST AVAILABLE COPY

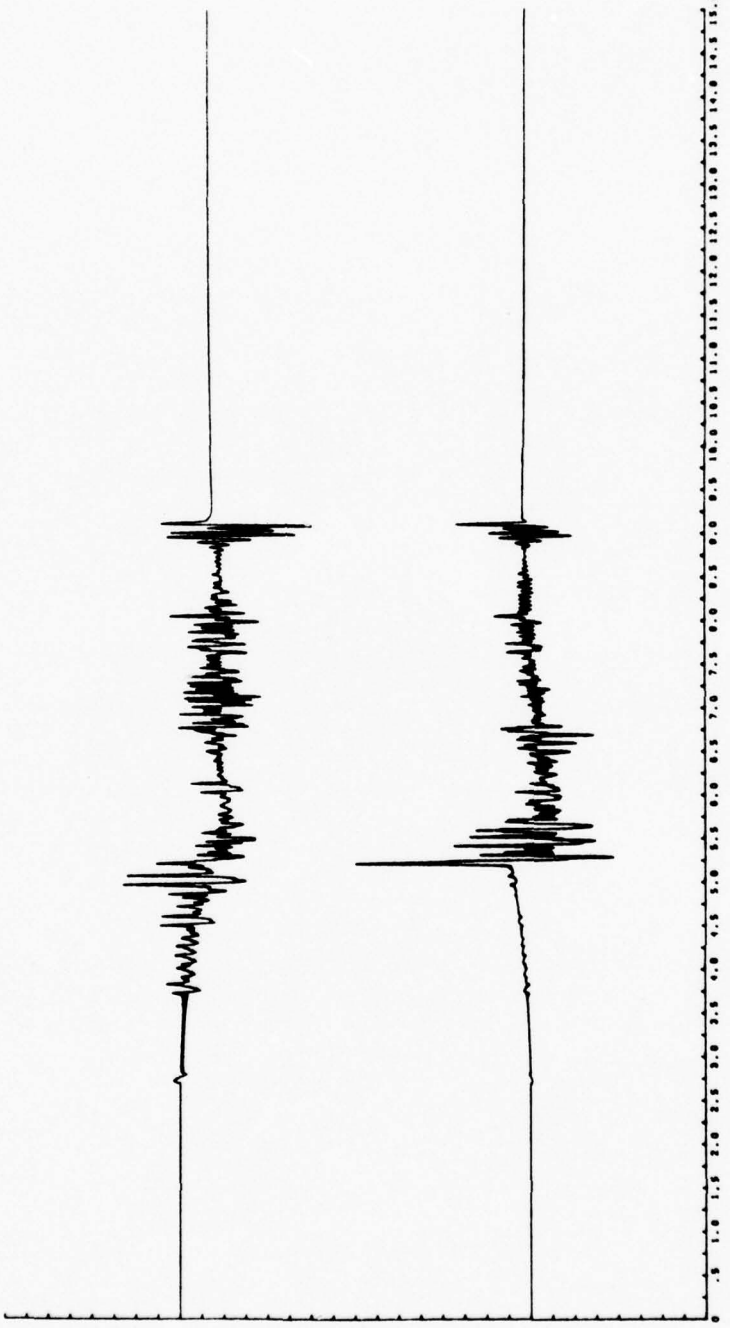


Fig. 4.3(15) Model accelerogram generated using the fault geometry of Fig. 4.3(11) and the source-instrument term of Fig. 3.3(4) (source two) with a rise time of 0.1 sec. Fault rupture begins at the hypocenter and propagates along the fault at 2.538 km/sec. The ordinate scale is 2.23 g/division/m of dislocation.

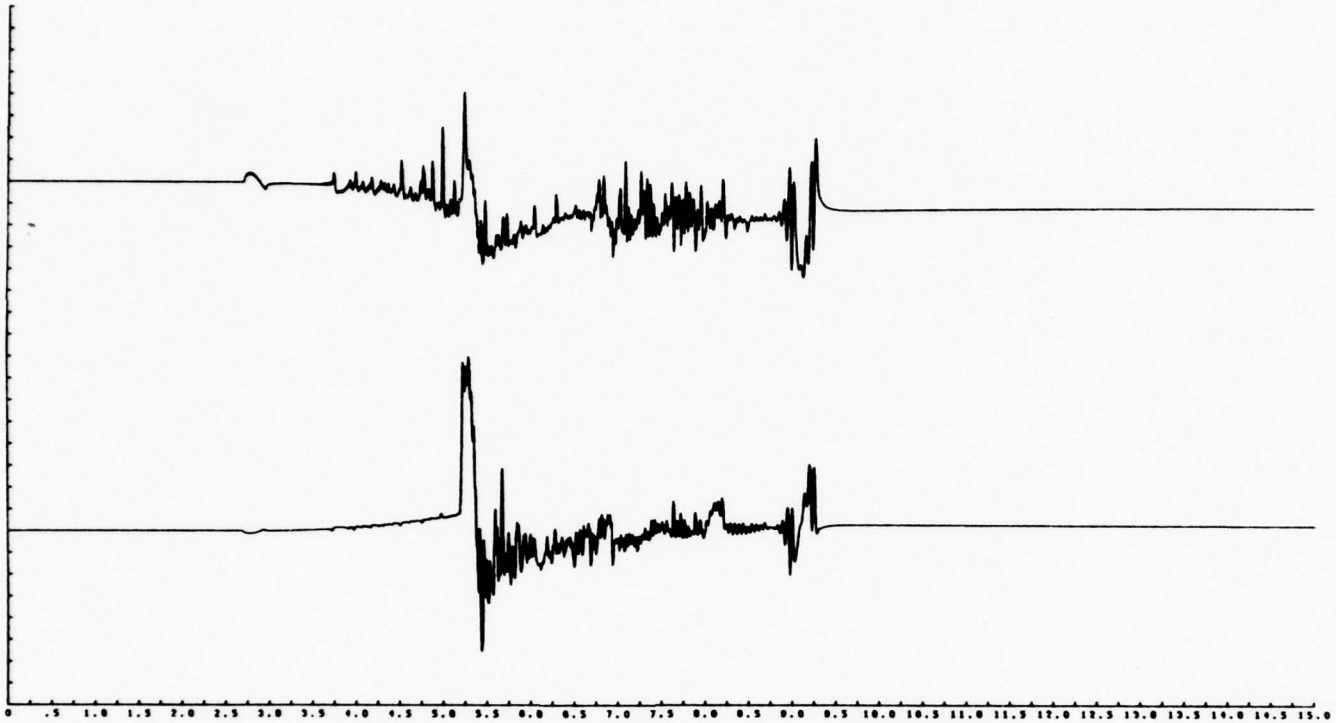


Fig. 4.3(16) Model accelerogram generated under conditions identical to those of Fig. 4.3(15) except now the rise time is 0.25 sec. The ordinate scale is 0.39 g/division/m of dislocation.

BEST AVAILABLE COPY

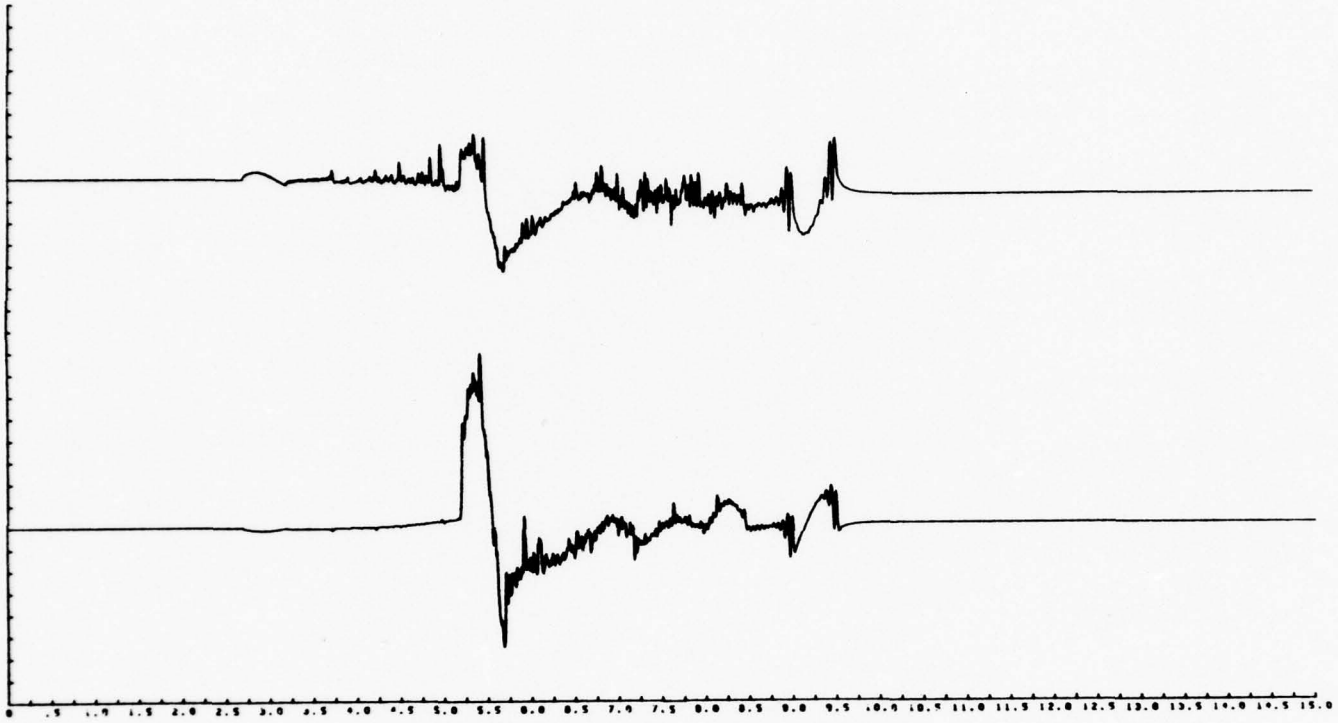


Fig. 4.3(17) Model accelerogram generated under conditions identical to those of Fig. 4.3(15) except now the rise time is 0.5 sec. The ordinate scale is 0.14 g/division/m of dislocation.

BEST AVAILABLE COPY

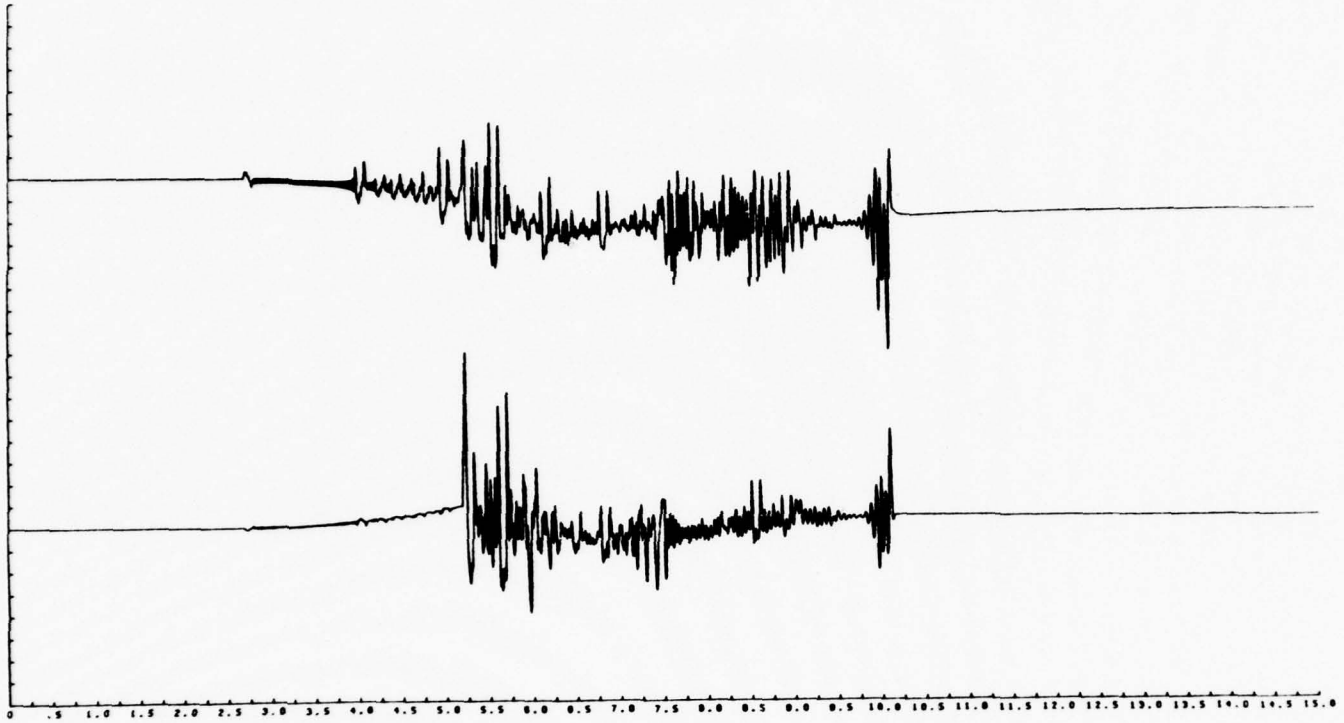


Fig. 4.3(18) Model accelerogram generated using the fault geometry of Fig. 4.3(11) and the source-instrument term of Fig. 3.3(4)(source two) with a rise time of 0.1 sec. Fault rupture begins at the hypocenter and propagates along the fault at 2.221 km/sec. The ordinate scale is 1.71 g/division/m of dislocation.

BEST AVAILABLE COPY

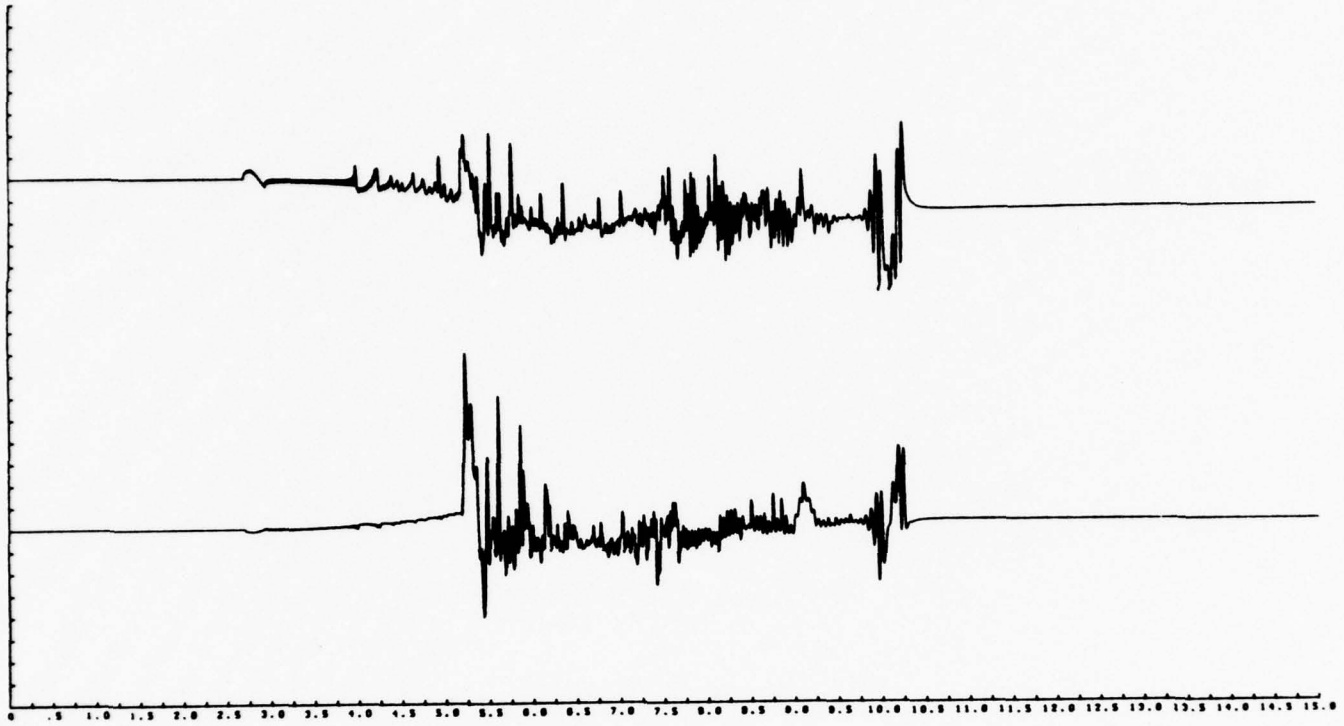


Fig. 4.3(19) Model accelerogram generated under conditions identical to those of Fig. 4.3(18) except now the rise time is 0.25 sec. The ordinate scale is 0.32 g/division/m of dislocation.

BEST AVAILABLE COPY

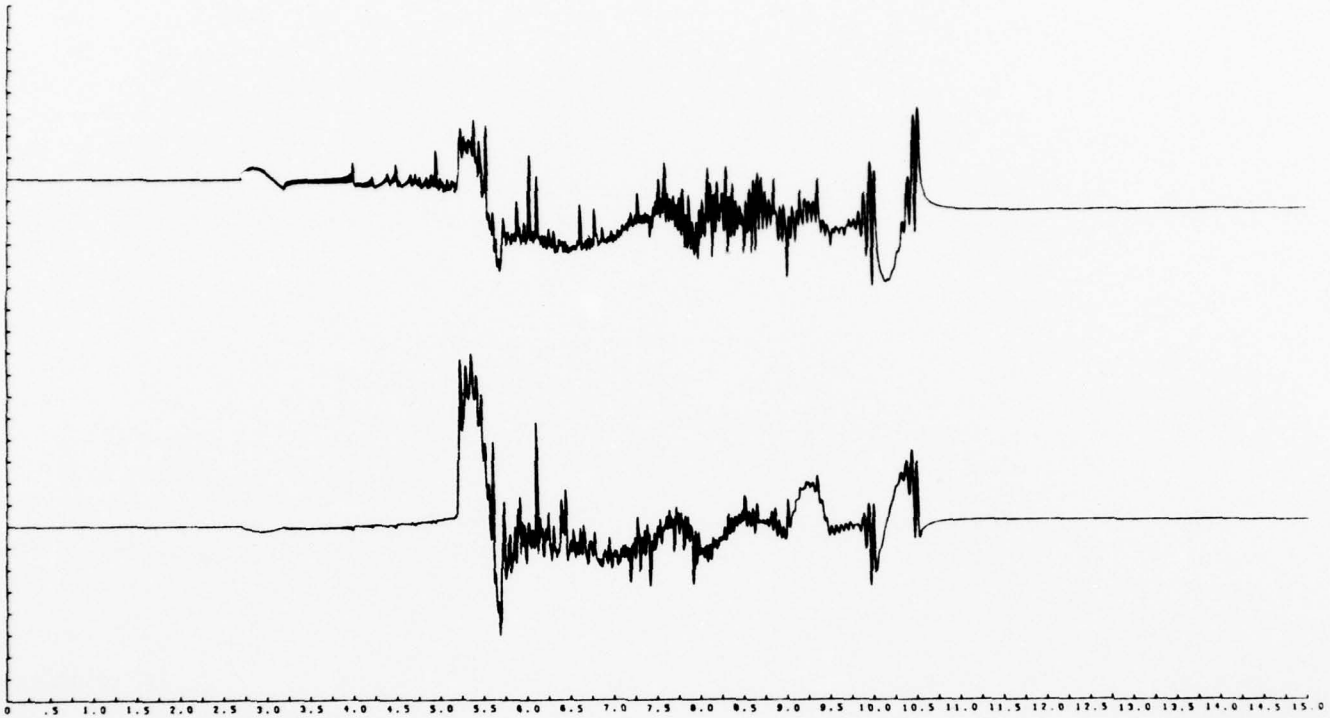


Fig. 4.3(20) Model accelerogram generated under conditions identical to those of Fig. 4.3(18) except now the rise time is 0.5 sec. The ordinate scale is 0.08 g/division/m of dislocation.

BEST AVAILABLE COPY

BEST AVAILABLE COPY

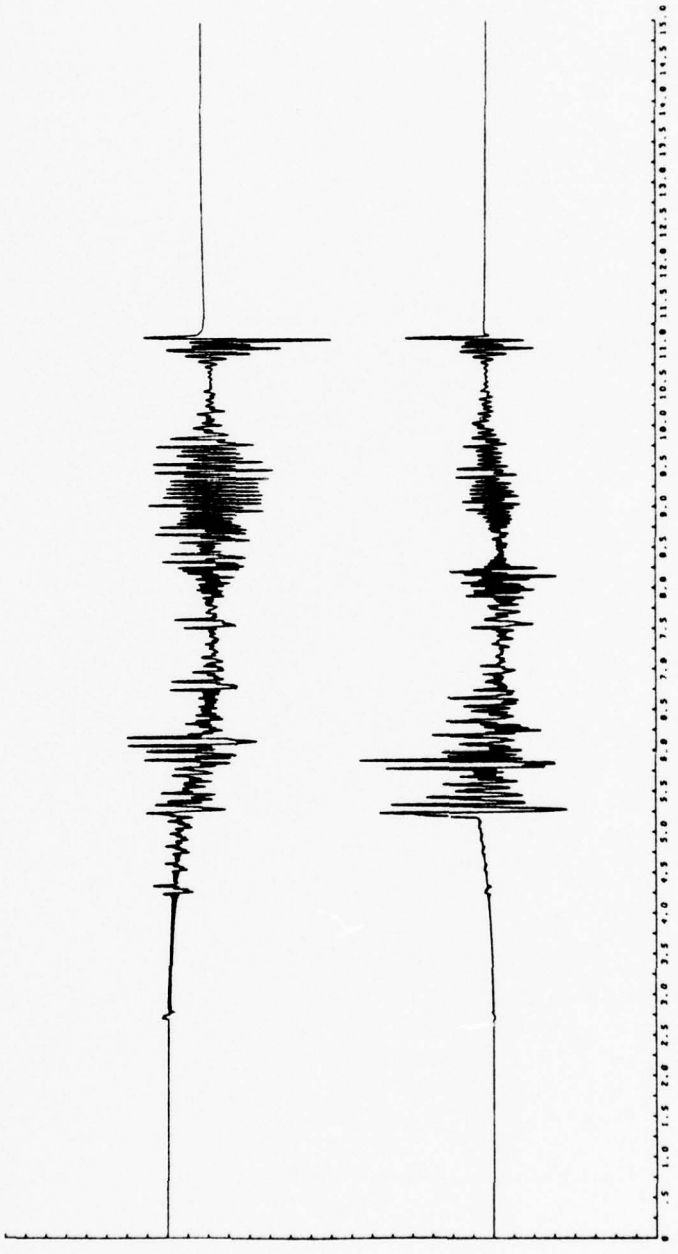


Fig. 4.3(21) Model accelerogram generated using the fault geometry of Fig. 4.3(11) and the source-instrument term of Fig. 3.3(4)(source two) with a rise time of 0.1 sec. Fault rupture begins at the hypocenter and propagates along the fault at 1.974 km/sec. The ordinate scale is 1.73 g/division/m of dislocation.

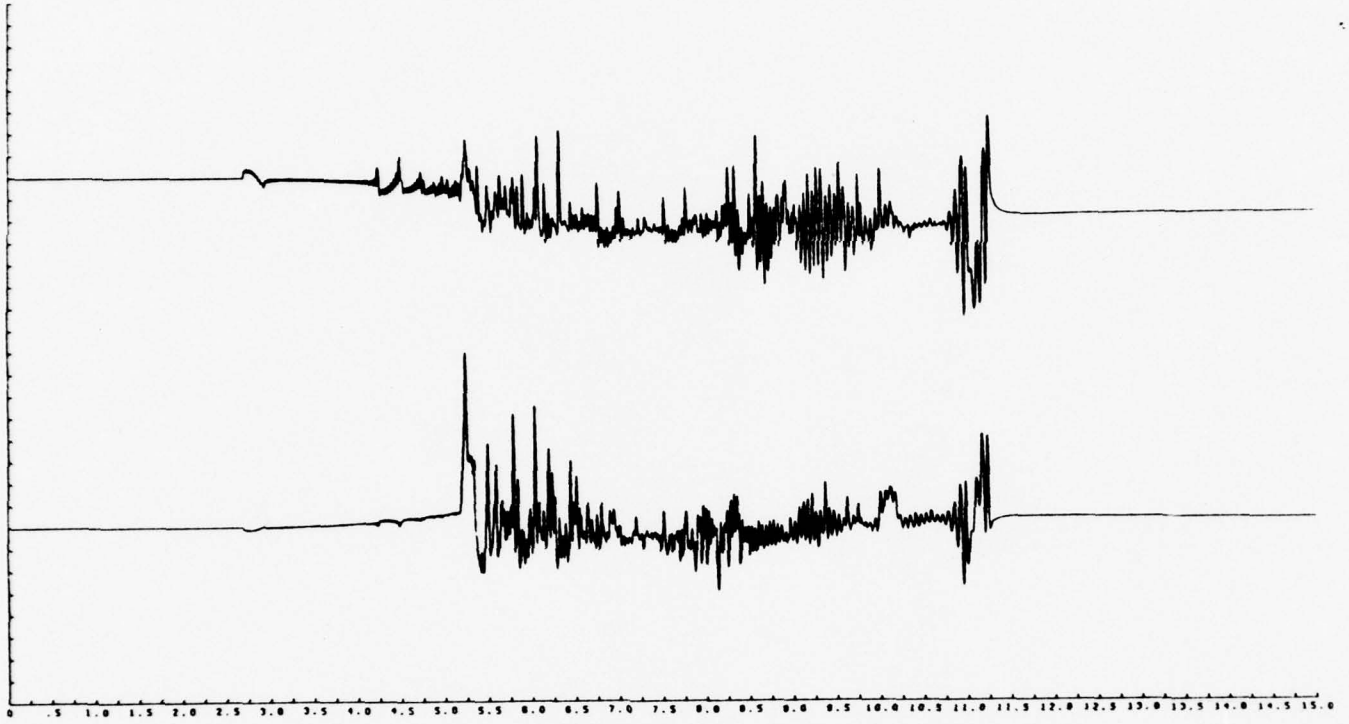


Fig. 4.3(22) Model accelerogram generated under conditions identical to those of Fig. 4.3(21) except now the rise time is 0.25 sec. The ordinate scale is 0.27 g/division/m of dislocation.

BEST AVAILABLE COPY

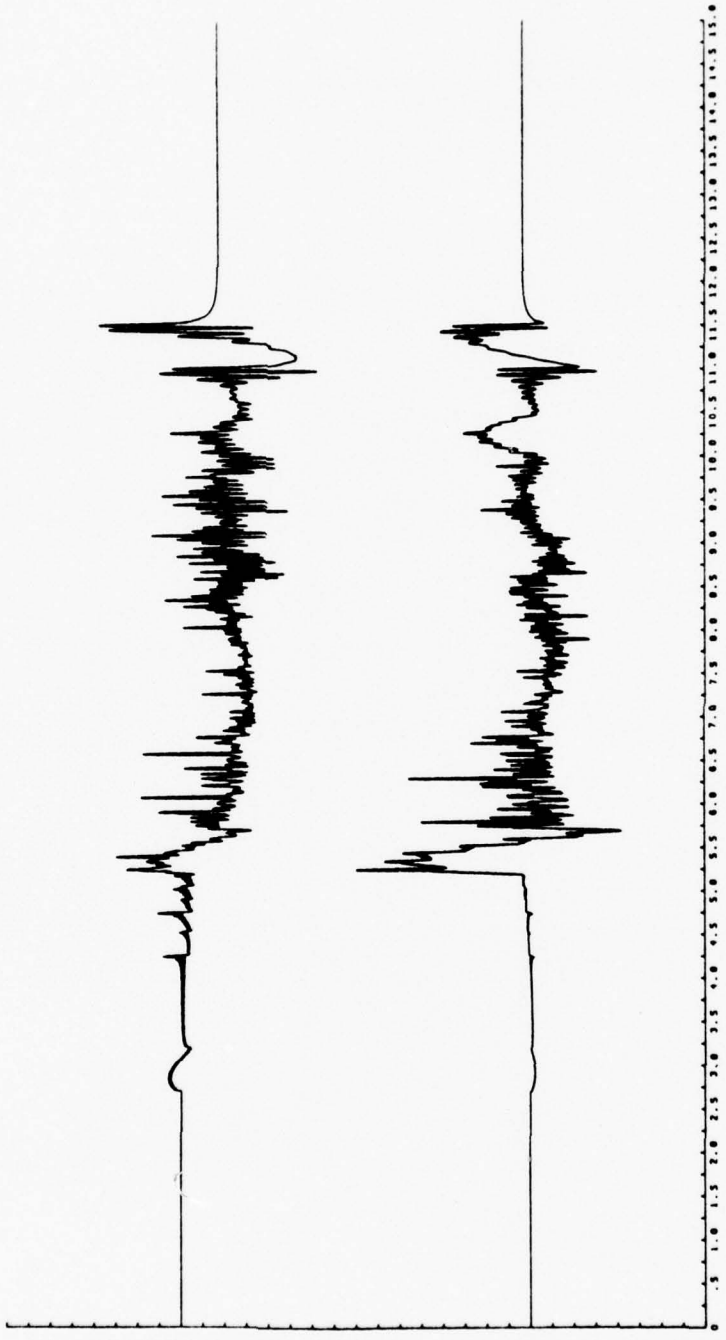


Fig. 4.3(23) Model accelerogram generated under conditions identical to those of Fig. 4.3(21) except now the rise time is 0.5 sec. The ordinate scale is 0.07 g/division/m of dislocation.

receiver geometry and the medium seismic velocities both of which remain the same. Conversely, the total length of the record of ground motion appearing on these model accelerograms is much shorter since this is very definitely a function of fault rupture propagation velocity as well as of fault geometry and seismic wave velocities. The interval between the arrival of the first or hypocentral P-wave at 2.7 sec and the last Rayleigh wave at approximately 9.5 sec is now 6.8 sec. This is the maximum record length we may hope to match to the Pacoima Dam records using the transfer function of a homogeneous half-space, the geometry of Figure 4.3(11), and a fault rupture velocity of 2.538 km/sec. The pulse duplication that we have seen to occur under favorable circumstances in Figures 4.3(12) through 4.3(15) at $t = r/c$ and $t = r/c + T$ is also evident in these source two accelerograms, again especially in the surface wave coda near the end of the records. Finally, the importance of the surface wave is again clearly distinguishable.

As might have been anticipated from the single source point records of source one and source two significant differences exist between their respective two hundred source point equivalents. Most notably, some constructive interference of the accelerations of individual sources is evident in Figures 4.3(15) through 4.3(17) especially in association with P- and S-wave arrivals from the hypocentral region. The durations of these P and S pulses are obviously related to the rise time of the dislocation source function since in each case the period of the pulse is equal to the pertinent rise time. Indeed, a comparison of the initial S-wave motions of these model accelerograms with those of the Pacoima Dam records of Figure 4.2(4) indicates a marked similarity for the longer model rise times. We have for the first time in this study

made a model acceleration to look something like a small part of a real record. However there remain many points of dissimilarity. The over-all frequency content of the model records is still too high in that individual record peaks are more impulsive than their observed counterparts. We have not matched the general appearance of the actual Pacoima Dam accelerograms. Nor have any significant phases after the initial S-wave been satisfactorily duplicated.

Any contention of minimal success for any of the model accelerograms appearing in Figures 4.3(5) through 4.3(17) depends wholly on the similarity between the observed and generated horizontal S-wave arrival. This similarity is best attained by Figure 4.3(17) where a rise time of 0.5 sec is used. Indeed, it appears that a somewhat better fit in this regard could be obtained by using a somewhat longer rise time. In view of the over-all failure of the model in other respects we shall not attempt the use of a longer rise time but shall instead continue our exploration of the effect of the variation of propagation velocity of fault rupture. Before leaving the records of Figures 4.3(15) through 4.3(17) several other of their features are worth mentioning. First, some long period noise is present in the form of final acceleration steps. This is again caused by numerical imperfections in the numerical convolution of source-instrument with geometric term that was seen with respect to Figures 4.3(12) through 4.3(14). This final non-zero value for acceleration is as intuitively unacceptable now as before. Secondly, the model peak accelerations again impose somewhat prohibitive limits on allowed fault dislocation amplitude. Following previous convention the ordinate scales of Figures 4.3(15) through 4.3(17) may be quoted as 2.23, 0.39, and 0.14 g/division/m of dislocation, respectively. For the

peak accelerations of these models to be in accord with the 1.25 g observed peak acceleration, fault dislocation amplitudes of 0.14, 0.80, and 2.23 m, respectively, are required. These are in more reasonable agreement with observation but are still rather small. Thus, the improvements in model and observed accelerogram fit made by consideration of source two rather than source one may be summaried as a better initial S-wave match and more realistic peak accelerations.

The opportunity to fit later segments of the Pacoima Dam record has been degraded by employing the faster fault rupture propagation velocity, however, since the model records are now significantly shorter than their observed counterpart. It is certainly not clear whether this is due to inadequacies in the medium transfer function of Chapter 2 upon which this study is based or to inappropriate fault geometry or even to errors in the seismic velocities employed. What is clear is that longer model accelerograms will be written by faulting schemes employing slower rupture propagation velocities. Will these slower velocities also improve model fit in ways other than merely increasing model record length? As we shall now see the answer to this question is generally "no".

In Figures 4.3(18) through 4.3(20) are presented accelerograms identical to those immediately preceeding except now a fault rupture propagation velocity of 2.221 km/sec is used as part of the model faulting process. To best see the effect of varying this velocity let us compare two model accelerograms differing only in this respect. In particular Figures 4.3(15) and 4.3(18) both employ source two dislocation time histories with a rise time of 0.1 sec and are otherwise identical except the first is associated with a fault rupturing at 2.538 km/sec and the second with one rupturing at 2.221 km/sec. The single most

important point to be made from such a comparison is at once evident. Other than with respect to record length, these two accelerograms look remarkably similar. It is almost as if we had merely expanded the time scale since the relative shapes, positions, and amplitudes of all important phase arrivals have remained unchanged. This phenomenon, which will turn out to be more or less generally observed in all succeeding similar model pairs, may be called conservation of accelerogram character under a general transformation of uniform fault rupture propagation velocity.

To the extent that this observation is univerally applicable it appears that once a given source-instrument term and rise time have been selected the remaining distinctive character of a model accelerogram is determined almost exclusively by the source-receiver geometry. Nor must we look far for the cause of this phenomenon. It is, perhaps, inevitable since so little constructive or destructive interference is taking place between the phase arrivals of individual point sources. Thus, it is in the character of the initial S-wave pulse where we have already seen constructive interference to be in operation that this conservation principle is weakest and where the variation of rupture propagation velocity has its greatest effect. This is better seen in comparisons between Figures 4.3(16) and 4.3(19) and again between Figures 4.3(17) and 4.3(20) where some roughness in the initial S pulse is introduced at the slower rupture velocity. Even here the principle of conservation of character is not seriously violated.

It might be contended that this phenomenon makes the modeling of accelerograms subtly superior to the modeling of ground motion representations with lower frequency content. This argument is premature

here but a more elaborate discussion of this point will be undertaken at the conclusion of this study.

The ordinate scales of Figures 4.3(18) through 4.3(20) may be quoted as 1.71, 0.32, and 0.08 g/division/m of dislocation. Under the usual constraint of the observed Pacoima Dam accelerogram's peak acceleration this implies fault dislocations of 0.18, 0.98, and 3.91 meters, respectively. These values are in essential agreement with those determined for the previous three model accelerograms again demonstrating the power of the conservation of character principle. The longer rise time models are obviously approaching realistic fault dislocation values.

The final three model accelerograms of this series are presented in Figures 4.3(21) through 4.3(23). These represent the model records generated under conditions identical to those of the previous six except now a fault rupture propagation velocity of 1.974 km/sec is used. The ordinate scales of these figures are 1.73, 0.27, and 0.07 g/division/m of dislocation. Again under the constraint of the observed peak acceleration this implies fault dislocations of 0.18, 1.16, and 4.58 meters, respectively. There is little in these records to alter or add to the conclusions reached from a study of their six predecessors.

Thus far our attempts to model the Pacoima Dam records with a model faulting process must be regarded as essential failures. The effort has been far from wasted, however, since very definite gains have been made in an understanding of the effects of model parameter variation upon the accelerogram ultimately generated. Therefore, let us briefly ignore the pertinence of Figures 4.3(15) through 4.3(23) to the actual faulting process at San Fernando on February 9, 1971 and recapitulate observed model accelerogram changes expected in connection with

variation of those parameters at our disposal as evidenced by these last nine figures.

The three major model determinants, in order of increasing importance, are fault rupture propagation velocity, source-instrument term time history, and fault-receiver geometry. The first of these has little effect on the character of the model accelerogram but merely contracts or expands the total record along the time axis in such a way that the frequency content remains unaltered. Because a small amount of interference among phase arrivals from individual point sources does occur (most notably in the source two accelerograms) variation of rupture propagation velocity has some effect on the character of the record. This effect is very small, however, for all cases so far studied. The principal features of a model accelerogram determined by the rupture velocity are total record duration and separation of significant phases for a given fault-receiver geometry.

The primary effect of the source-instrument term is to specify the shape and frequency content of each individual peak of the model accelerogram. This point has been adequately explored previously and is well demonstrated in Figures 4.3(2) through 4.3(10). It will not be belabored here. Again, due to the essential lack of interference between arrivals from individual point sources conclusions reached with regard to single and composite source records are the same.

Finally, the effect of the source-receiver geometry is to determine the relative amplitude and position of distinctive phase arrivals. To a lesser extent their shapes are also affected especially where interference is taking place. The geometry controls the most important and recognizable features of a model record.

In this context we may expect to improve the models thus far produced by considering both a better source term and a better fault geometry relative to the receiving location. If the summarization just presented is valid, neither alteration will be sufficient in itself to achieve a good match to the observed Pacoima records but more realistic formulation of either parameters should cause a notable improvement in fit independent of the other. Therefore, let us consider a number of models generated using source-instrument term three in conjunction with the familiar fault geometry and rupture propagation velocities. These are presented in Figures 4.3(24) through 4.3(29).

In Figures 4.3(24) through 4.3(26) a fault rupture propagation velocity of 2.538 km/sec is used. The source three rise times are 0.1, 0.25, and 0.5 sec, respectively, and the corresponding ordinate scales are 2.32, 0.43, and 0.16 g/division/m of dislocation implying fault dislocations of 0.13, 0.73, and 1.95 meters if the peak record acceleration is to be 1.25 g as the Pacoima records imply it should be. In Figures 4.3(27) through 4.3(29) are presented similar accelerograms derived using a rupture velocity of 1.974 km/sec. The three source rise times are again 0.1, 0.25, and 0.5 sec, respectively, and the corresponding ordinate scales are 1.63, 0.23, and 0.06 g/division/m of dislocation implying fault dislocations of 0.19, 1.36, and 5.21 meters under the usual constraint.

A comparison of these records with their source two equivalents indicates that in all cases we have succeeded in generating somewhat smoother versions of these model accelerograms. Several longer period features (in the range of two to four Hertz) have become accentuated and most of the shorter period features (in the range of ten to twenty

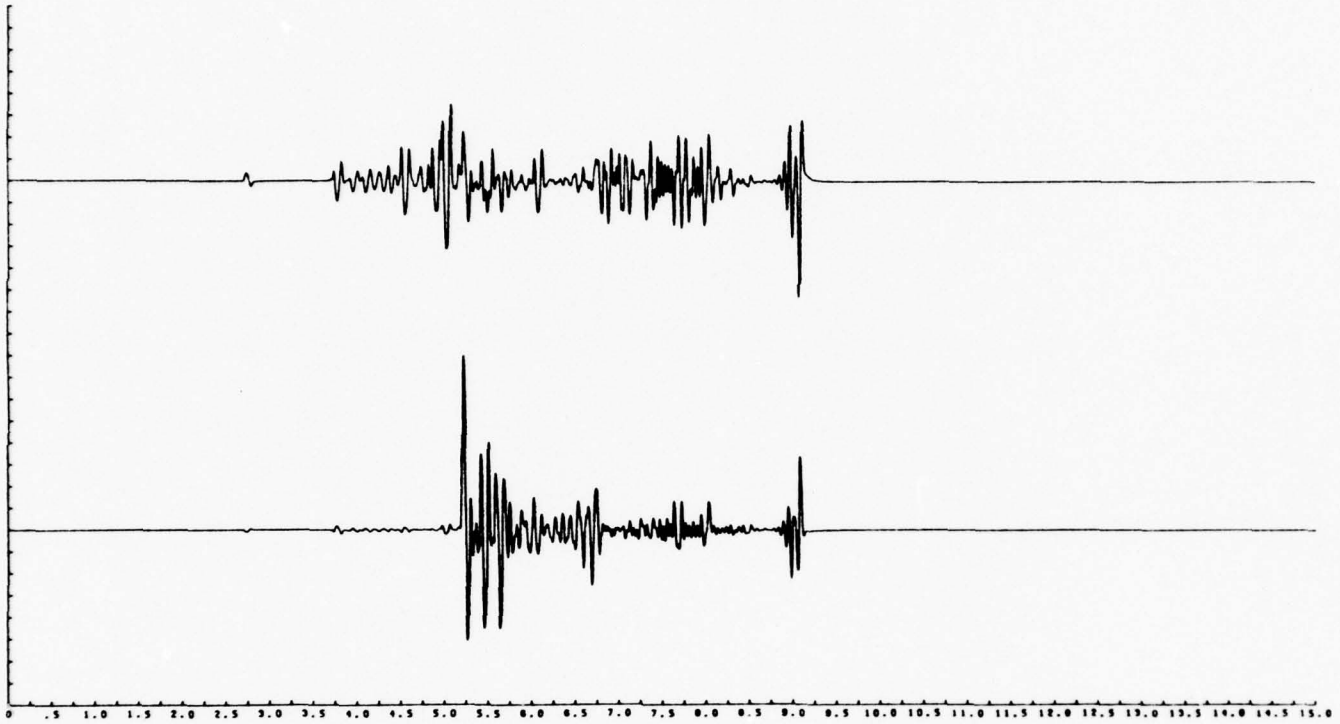


Fig. 4.3(24) Model accelerogram generated using the fault geometry of Fig. 4.3(11) and the source-instrument term of Fig. 3.3(6)(source three) with a rise time of 0.1 sec. Fault rupture begins at the hypocenter and propagates along the fault at 2.538 km/sec. The ordinate scale is 2.32 g/division/m of dislocation.

BEST AVAILABLE COPY

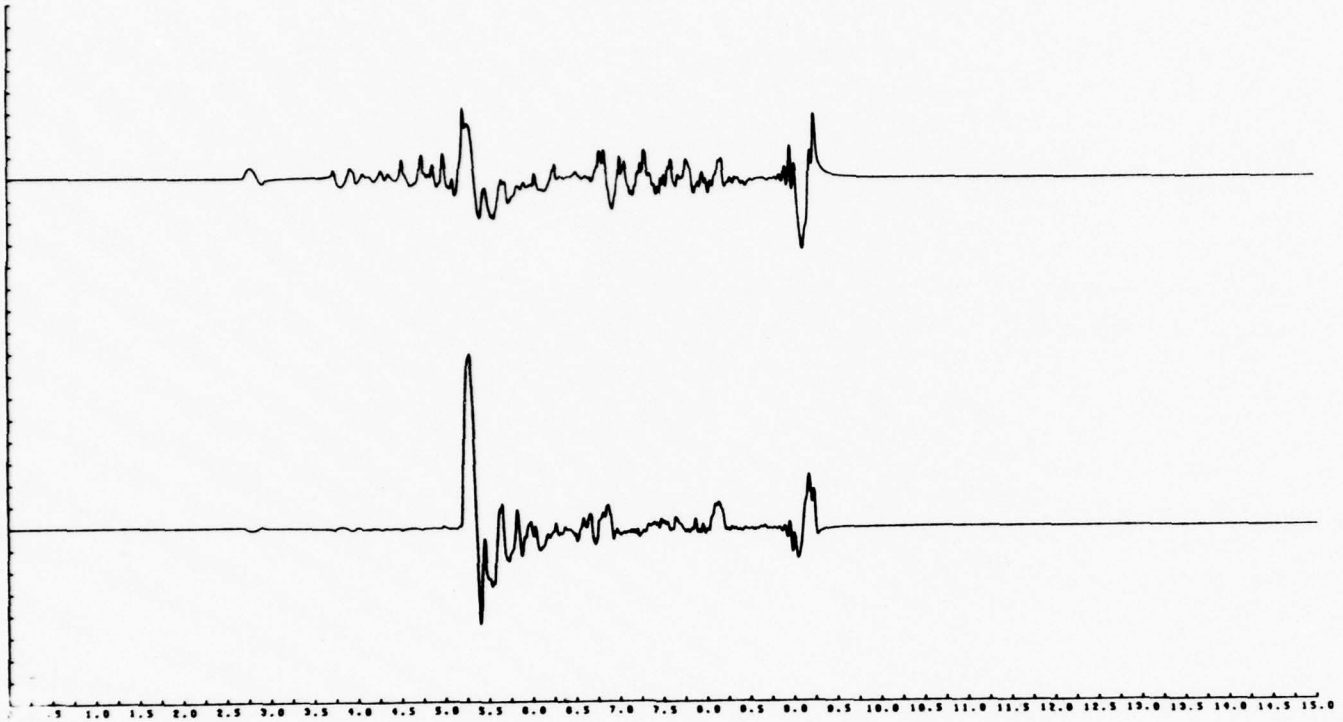


Fig. 4.3(25) Model accelerogram generated under conditions identical to those of Fig. 4.3(24) except now the rise time is 0.25 sec. The ordinate scale is 0.43 g/division/m of dislocation.

BEST AVAILABLE COPY

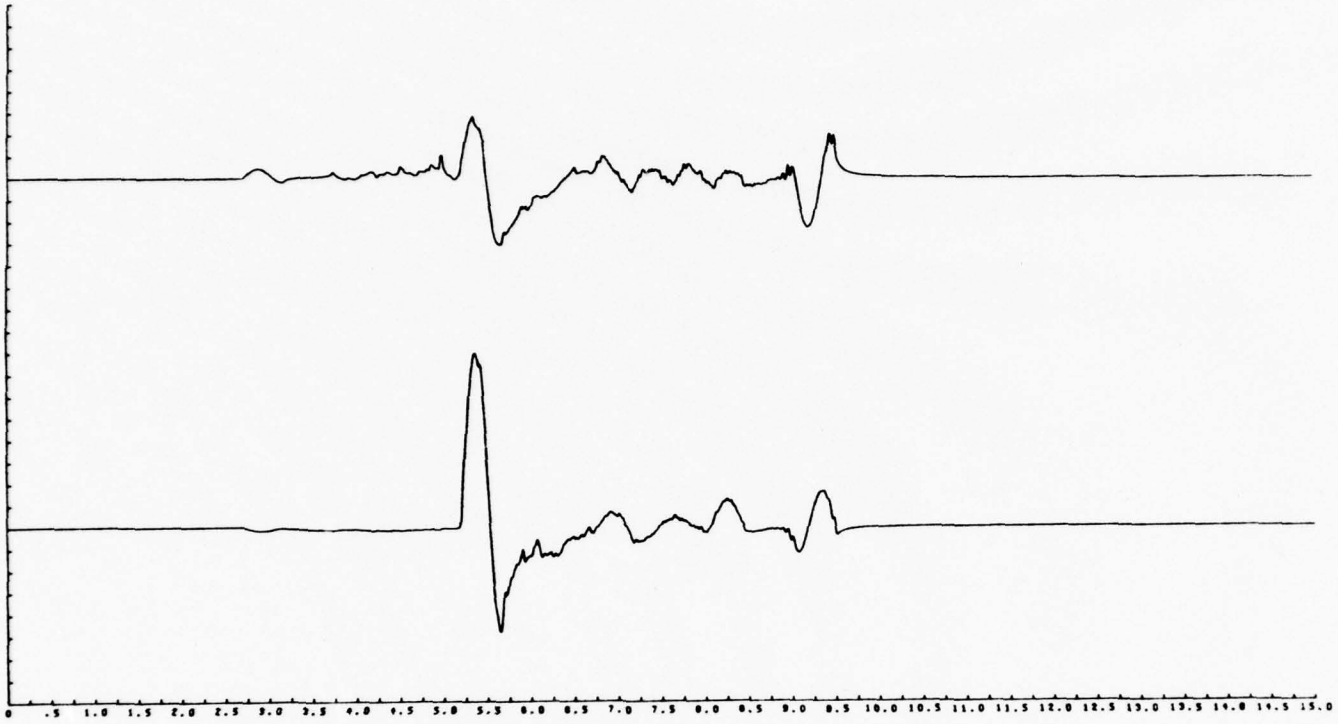


Fig. 4.3(26) Model accelerogram generated under conditions identical to those of Fig. 4.3(24) except now the rise time is 0.5 sec. The ordinate scale is 0.16 g/division/m of dislocation.

BEST AVAILABLE COPY

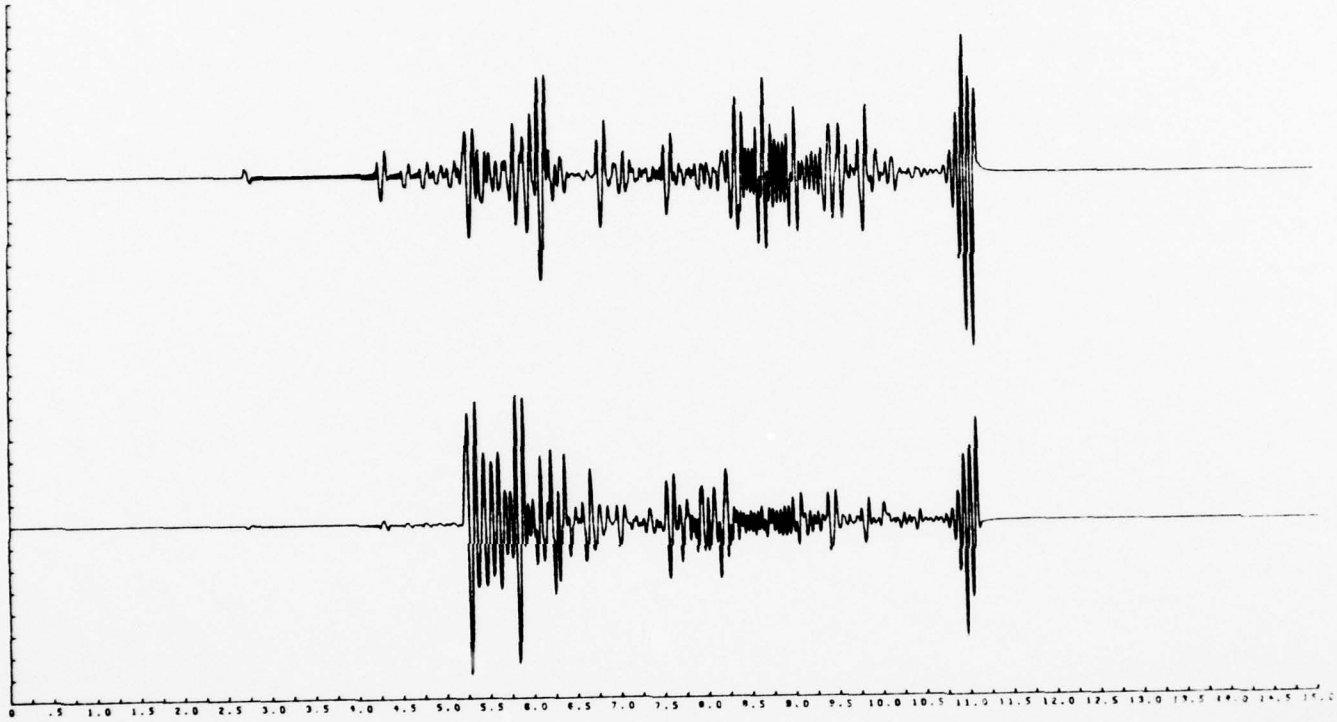


Fig. 4.3(27) Model accelerogram generated using the fault geometry of Fig. 4.3(11) and the source-instrument term of Fig. 3.3(6)(source three) with a rise time of 0.1 sec. Fault rupture begins at the hypocenter and propagates along the fault at 1.974 km/sec. The ordinate scale is 1.63 g/division/m of dislocation.

BEST AVAILABLE COPY

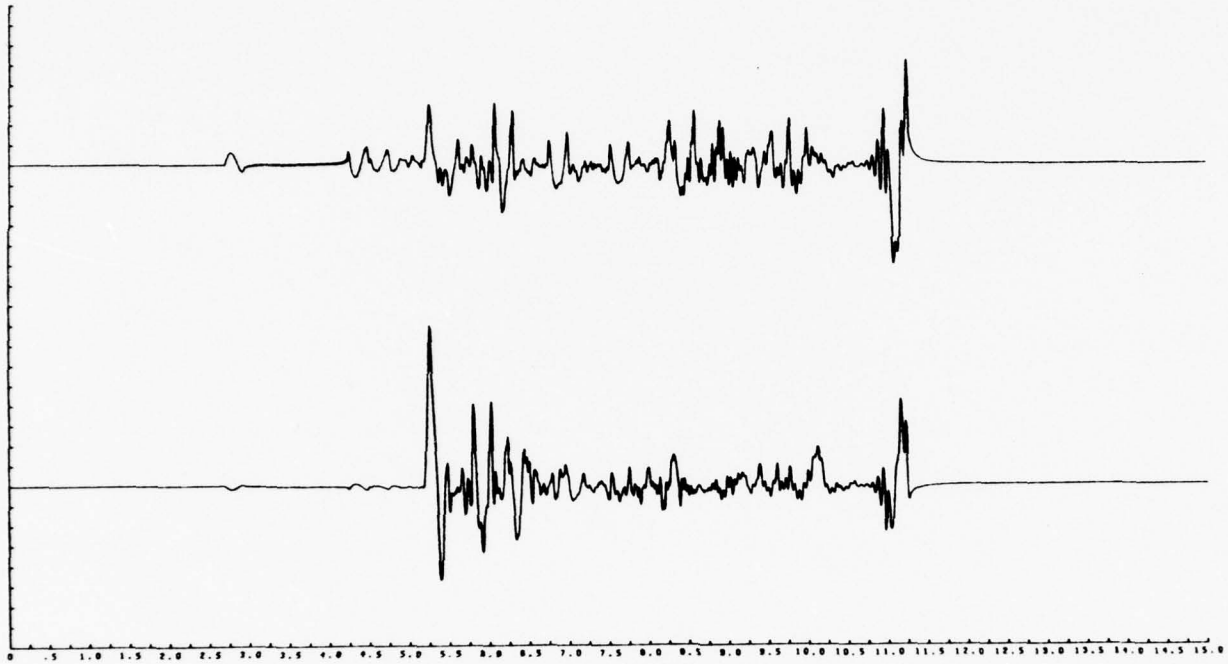


Fig. 4.3(28) Model accelerogram generated under conditions identical to those of Fig. 4.3(27) except now the rise time is 0.25 sec. The ordinate scale is 0.23 g/division/m of dislocation.

BEST AVAILABLE COPY

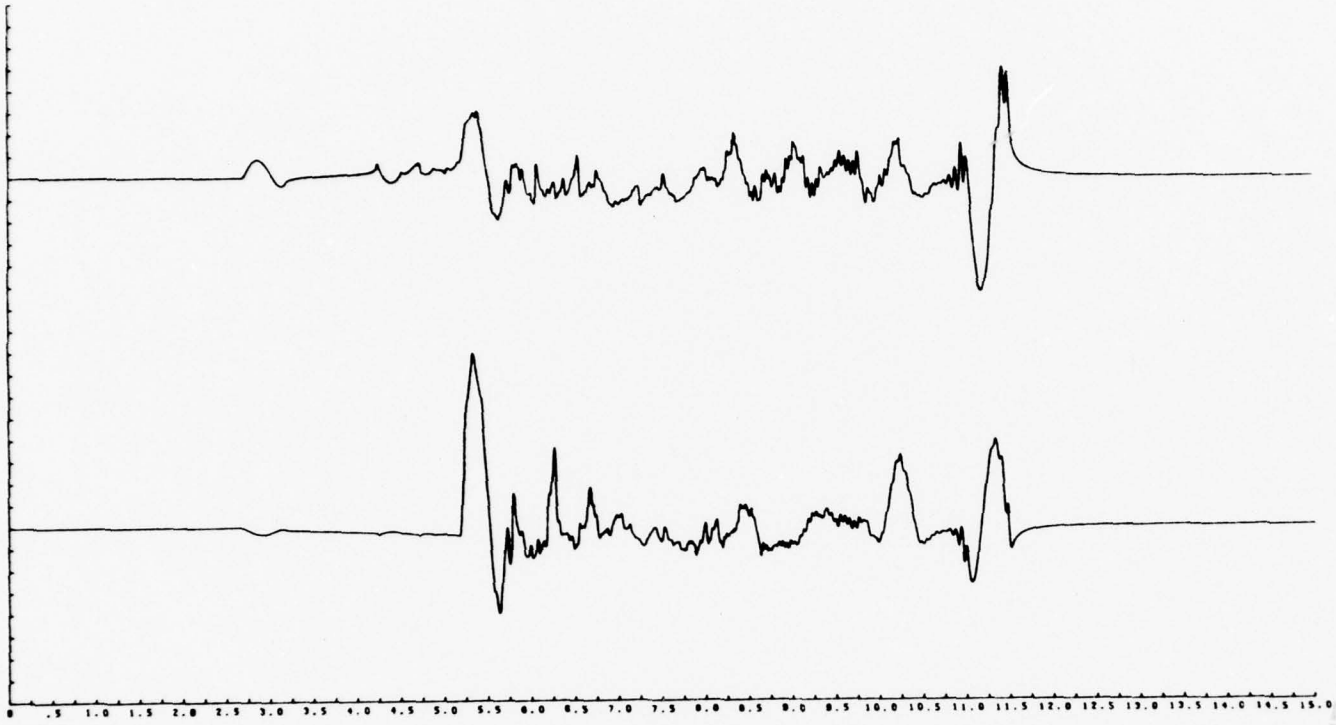


Fig. 4.3(29) Model accelerogram generated under conditions identical to those of Fig. 4.3(27) except now the rise time is 0.5 sec. The ordinate scale is 0.06 g/division/m of dislocation.

BEST AVAILABLE COPY

Hertz) have been de-emphasized. The final acceleration values which have proved annoying before have now been reduced to essentially zero. Otherwise, remarkable similarity exists between all source two-source three model pairs.

A comparison of the accelerograms of Figures 4.3(24) through 4.3(29) with the resolved Pacoima Dam records of Figure 4.2(4) indicates that these last models are apparently capable of matching the frequency character of the observed accelerograms at least in gross detail. Thus, one of the features of previous models that was found objectionable has been seemingly overcome. As was the case with all previous accelerograms, however, a true match of significant arrivals is lacking. Again, if the summary of the effect of parameter variation given above is valid, as these last six records would seem to substantiate, this situation will be improved by a consideration of a more accurate fault geometry. This is attempted in the next section.

4.32 Model Accelerograms from a Hinged Fault

As discussed in Chapter 1 the planar fault model employed by Canitez and Toksöz (1972), Mikumo (1973), and Trifunac (1974) to explain various static and dynamic consequencies of the faulting process associated with the San Fernando earthquake of February 9, 1971 is unsatisfactory in several respects. As has been shown by Turnbull and Battis (1973) and by Hanks (1974) some of these deficiencies may be qualitatively and quantitatively reduced by considering a fault surface that is hinged in some manner so that, generally, the dip of the fault plane increases with depth. We now wish to see whether model strong-motion records may also be improved by the use of such a fault model.

Any proposed fault must conform to certain constraints. Thus, the

hypocentral position, or point of initial rupture, must lie on the fault surface, the dip of the fault surface must be near 52° at the hypocenter and must conform to observed surface faulting, and the geometry of the surface fault rupture relative to the epicenter (and to Pacoima Dam) must be maintained. A model incorporating all of these constraints is shown in Figure 4.3(30). This fault model is a somewhat simplified version of the one derived by Alewine and Jordan (1973) using the closed form analytic expressions for displacement in an elastic half-space due to an inclined rectangular fault given by Mansinha and Smylie (1971). These displacements are calculated for each of forty-seven appropriately oriented fault elements constrained to conform to other observed geophysical properties of the fault as outlined above and then summed to give the final displacements for the model. Not considered here, but included in the model of Alewine and Jordan are a system of splay faults near the surface and a component of normal fault motion on the San Gabriel fault. The first feature is an unnecessary complication at this level of the study since it can only affect the very end of any model accelerogram generated in the manner of those we have previously considered where rupture starts at the hypocenter and propagates to the surface. The second feature is omitted since it is not clear whether any motion on the San Gabriel fault is better associated with regional stress adjustments after the main earthquake or with the main earthquake itself. The part of the model used in this study is in general agreement with that employed by Hanks (1974).

We now proceed much as before. That is, to model the ground motion at Pacoima Dam due to motion along the entire fault, the ground motions from two hundred individual sources evenly distributed over the fault

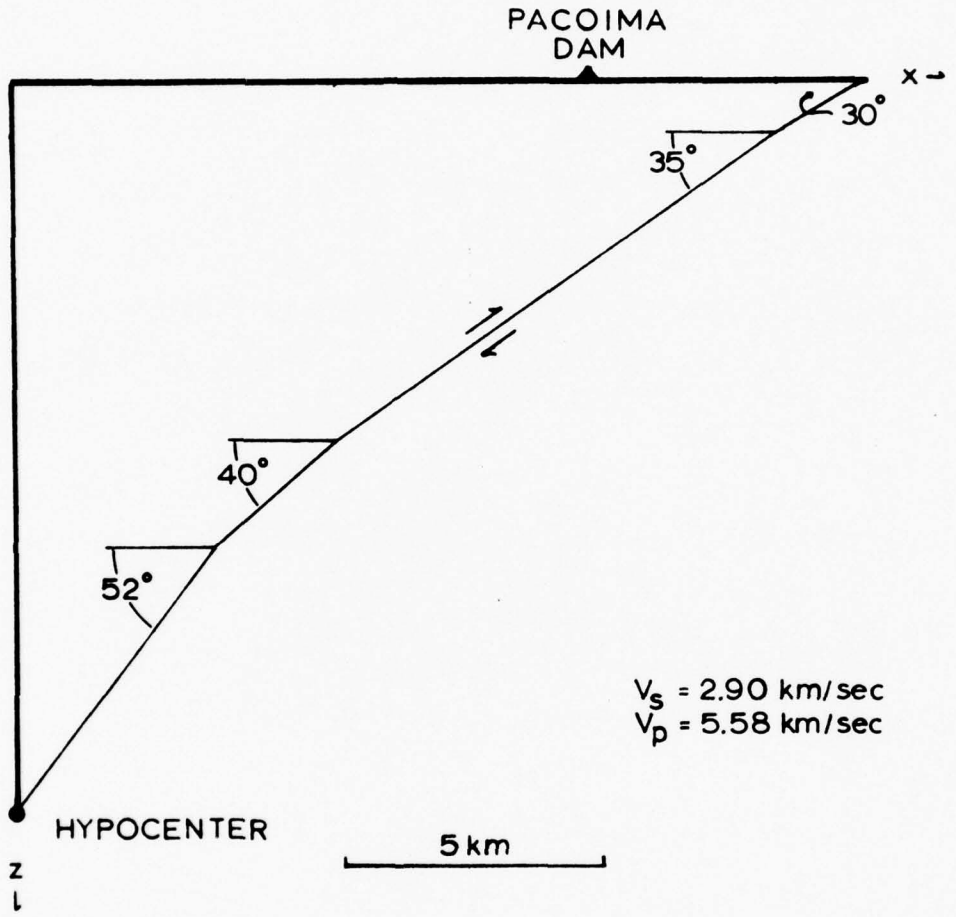


Fig. 4.3(30) Hinged model of the fault associated with the San Fernando earthquake of February 9, 1971 (after Alewine and Jordan, 1973). The hypocenter of the earthquake is at the lower end of the fault. The sense of fault motion, the relative position of Pacoima Dam, and the seismic velocities used in subsequent calculations are also shown.

surface are calculated and stored on magnetic tape. The summation of these ground motions is then done in such a way as to simulate propagation of the dislocation episode along the fault at some fault rupture velocity. Only discrete values of this velocity are possible if additional interpolation between points is to be avoided and since the total fault length is somewhat greater in this case while the number of point sources has remained the same these discrete velocity values will now be somewhat different. From Figure 4.3(30) we see that the total fault length is now 21.66 km. The allowable rupture propagation velocities within the range of interest are now 1.969, 2.166, and 2.407 km/sec corresponding to time steps between points of 0.055, 0.050, and 0.045 sec, respectively. It remains but to convolve this summed ground motion with the various source-instrument terms of Chapter 3 in the familiar manner.

Using this new fault model let us begin by considering the simplest source. Model accelerograms employing the source-instrument term one, the model geometry of Figure 4.3(30), and a fault rupture propagation velocity of 1.969 km/sec are presented in Figures 4.3(31) through 4.3(33) for rise times of 0.1, 0.25, and 0.5 sec, respectively. The ordinate scales are 15.36, 6.11, and 2.91 g/division/m of dislocation implying fault displacements of 0.02, 0.05, and 0.11 meters under the constraint imposed by the observed Pacoima peak acceleration.

These model accelerograms are disappointing in that they do not match the observed records of Figure 4.2(4) much, if any, better than their planar fault counterparts. Their frequency content is too high and the constraints imposed on the amplitude of fault dislocation are unacceptable. Also, with the re-introduction of source-instrument term

BEST AVAILABLE COPY

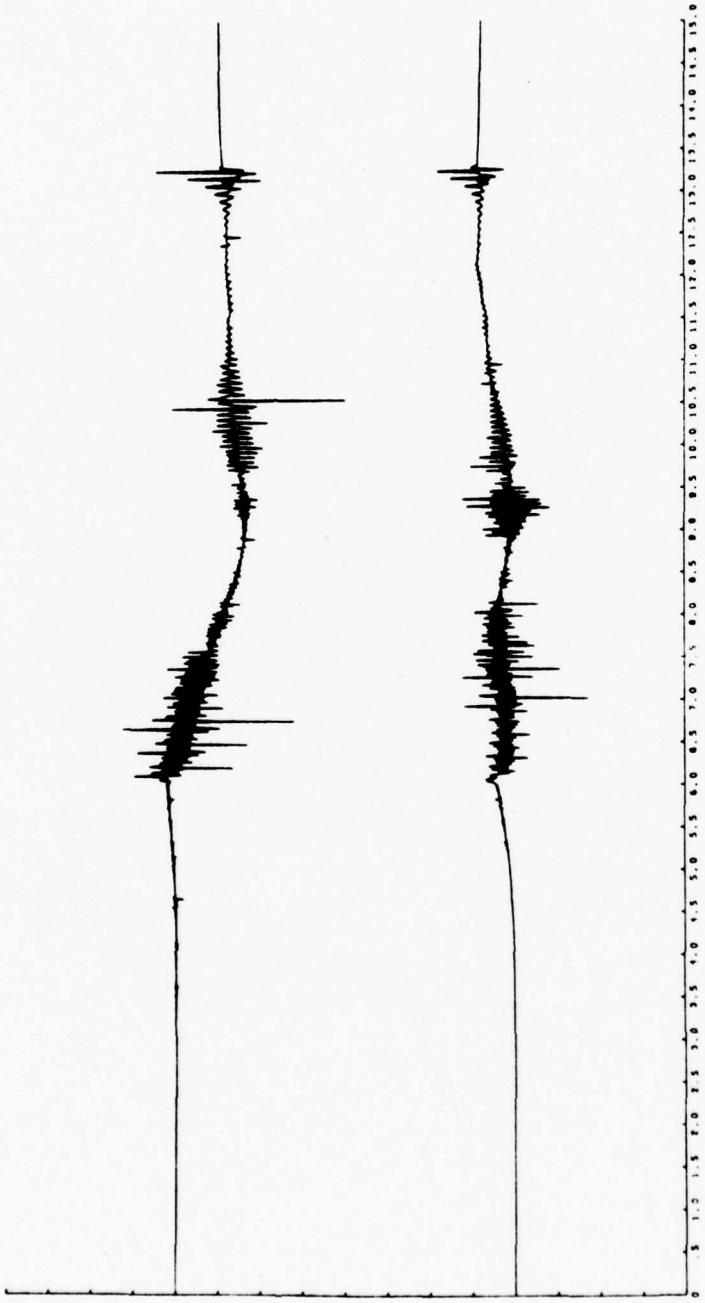


Fig. 4.3(31) Model accelerogram generated using the fault geometry of Fig. 4.3(30) and the source-instrument term of Fig. 3.3(2) (source one) with a rise time of 0.1 sec. Fault rupture begins at the hypocenter and propagates along the fault at 1.969 km/sec. The ordinate scale is 15.36 g/division/m of dislocation.

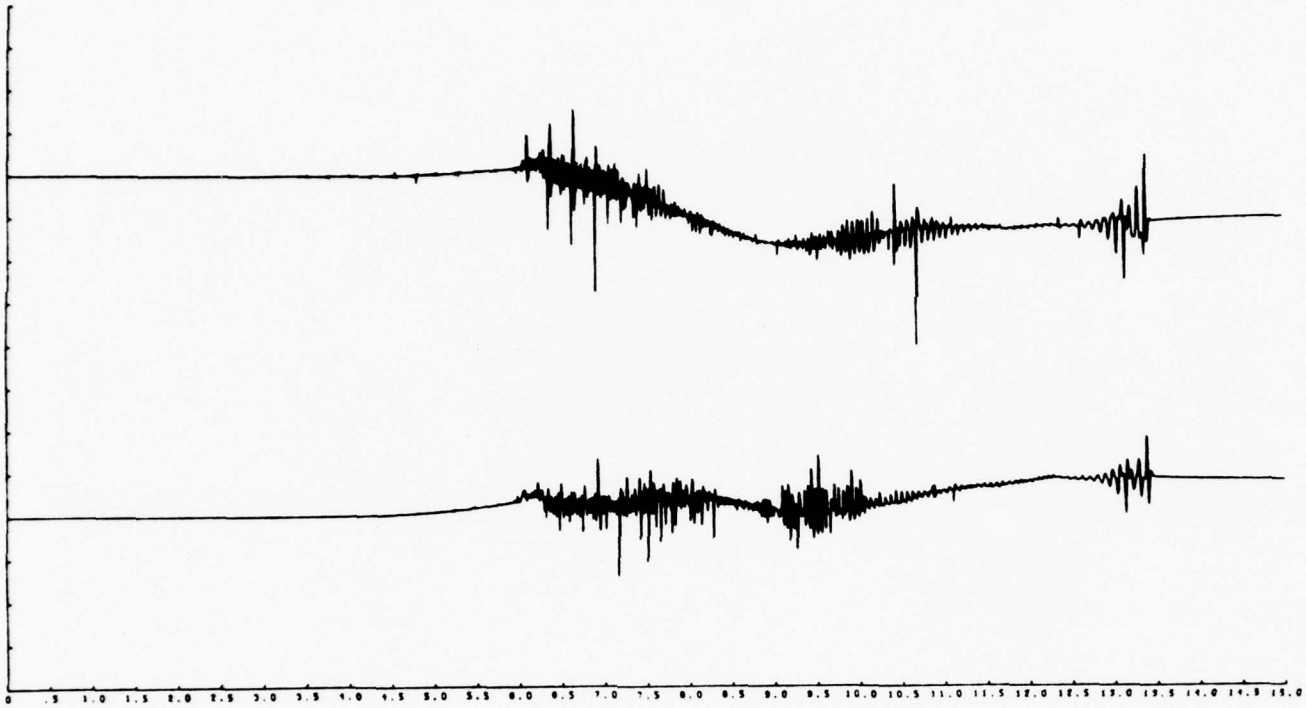


Fig. 4.3(32) Model accelerogram generated under conditions identical to those of Fig. 4.3(31) except now the rise time is 0.25 sec. The ordinate scale is 6.11 g/division/m of dislocation.

BEST AVAILABLE COPY

BEST AVAILABLE COPY

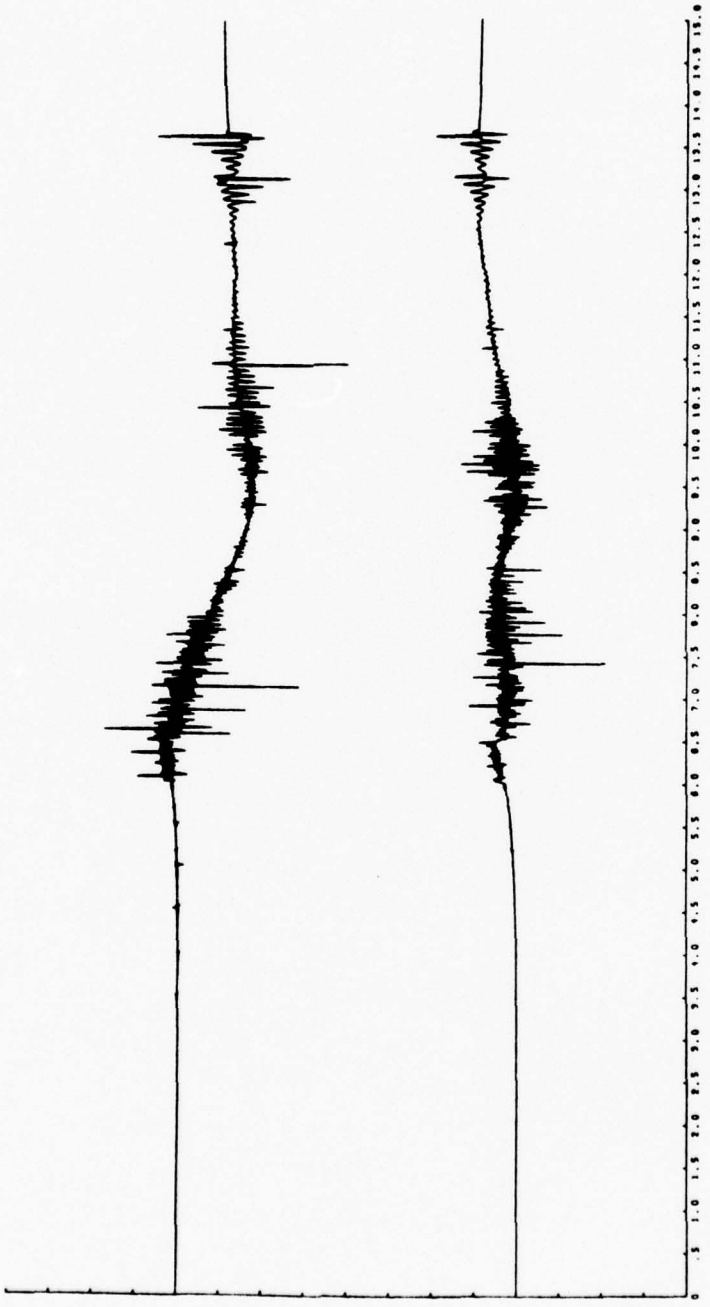


Fig. 4.3(33) Model accelerogram generated under conditions identical to those of Fig. 4.3(31) except now the rise time is 0.5 sec. The ordinate scale is 2.91 g/division/m of dislocation.

one, numerical noise is again present in the form of a step offset in acceleration remaining after all elastic energy has arrived from the source. Differences do exist, however, arising from the different geometry. Several could easily have been anticipated such as the lengthening of the S-P wave interval from the point of initial rupture resulting from the increased hypocenter-station distance and the increased total record length due to the longer fault surface of Figure 4.3(30). Perhaps also to be expected is the increase in peak acceleration since the closest approach of fault to receiver is reduced for the geometry here employed. Other changes might not have been so easily anticipated, however, such as the appearance of an important phase arrival near the middle of the vertical component time history which was not previously apparent. The distinct features of this geometry will be considered in greater detail later when a more satisfactory source-instrument term will be used.

Although Figures 4.3(31) through 4.3(33) have not obviously advanced the search for a fruitful model of the faulting process associated with the San Fernando earthquake in any significant manner, they have admirably fulfilled their principal aim which was to demonstrate the invariance of what has been termed the conservation of character under a transformation of model geometry. These three figures are similar to their planar predecessors exactly as we would expect and are also dissimilar in precisely the expected manner.

Let us now go on to consider one final series of model accelerograms. That is, we wish to generate those three sets of records with fault rupture propagation velocities of 2.407, 2.166, and 1.969 km/sec using the fault geometry after Alewine and Jordan (1973) as shown in

Figure 4.3(30) and source-instrument term three. Since each source-instrument term is evaluated for three rise times a complete series of this type consists of nine model accelerograms. Actually, the record of this set employing a rupture propagation velocity of 2.407 km/sec and a rise time of 0.1 sec was inadvertently omitted. The remaining eight accelerograms are shown in Figures 4.3(34) through 4.3(41). Since the procedure by which these model records are presented is somewhat unavoidably repetitious, we shall list their fundamental properties here in a very straightforward way and defer more elaborate considerations until all eight records have been treated.

In Figures 4.3(34) and 4.3(35) are shown the two models of this series evaluated for a rupture velocity of 2.407 km/sec. The source function rise times are 0.25 and 0.5 sec, respectively, and the ordinate scales, again respectively, are 0.43 and 0.14 g/division/m of dislocation implying total fault dislocation amplitudes of 0.72 and 2.19 meters if the maximum model accelerations are to agree with the 1.25 g value observed at Pacoima Dam.

Model accelerograms employing the source-instrument term three, the model geometry of Figure 4.3(30), and a fault rupture propagation velocity of 2.166 km/sec are presented in Figures 4.3(36) through 4.3(38) for rise times of 0.1, 0.25, and 0.5 sec, respectively. The ordinate scales are 4.18, 0.27, and 0.09 g/division/m of dislocation implying fault displacements of 0.07, 1.14, and 3.64 meters under the constraint imposed by the observed Pacoima Dam peak acceleration.

Finally, model accelerograms of this series employing a fault rupture propagation velocity of 1.969 km/sec are presented in Figures 4.3(39) through 4.3(41) for rise times of 0.1, 0.25, and 0.5 sec,

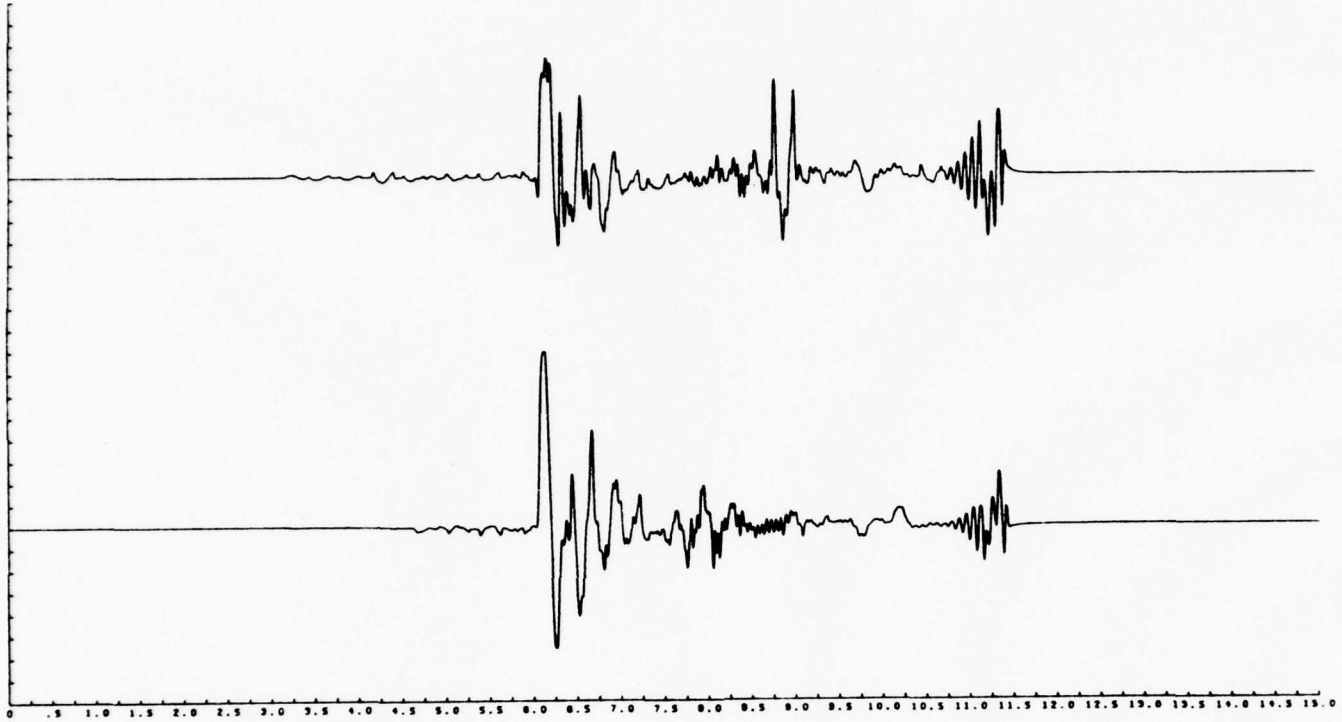


Fig. 4.3(34) Model accelerogram generated using the fault geometry of Fig. 4.3(30) and the source-instrument term of Fig. 3.3(6) (source three) with a rise time of 0.25 sec. Fault rupture begins at the hypocenter and propagates along the fault at 2.407 km/sec. The ordinate scale is 0.43 g/division/m of dislocation.

BEST AVAILABLE COPY

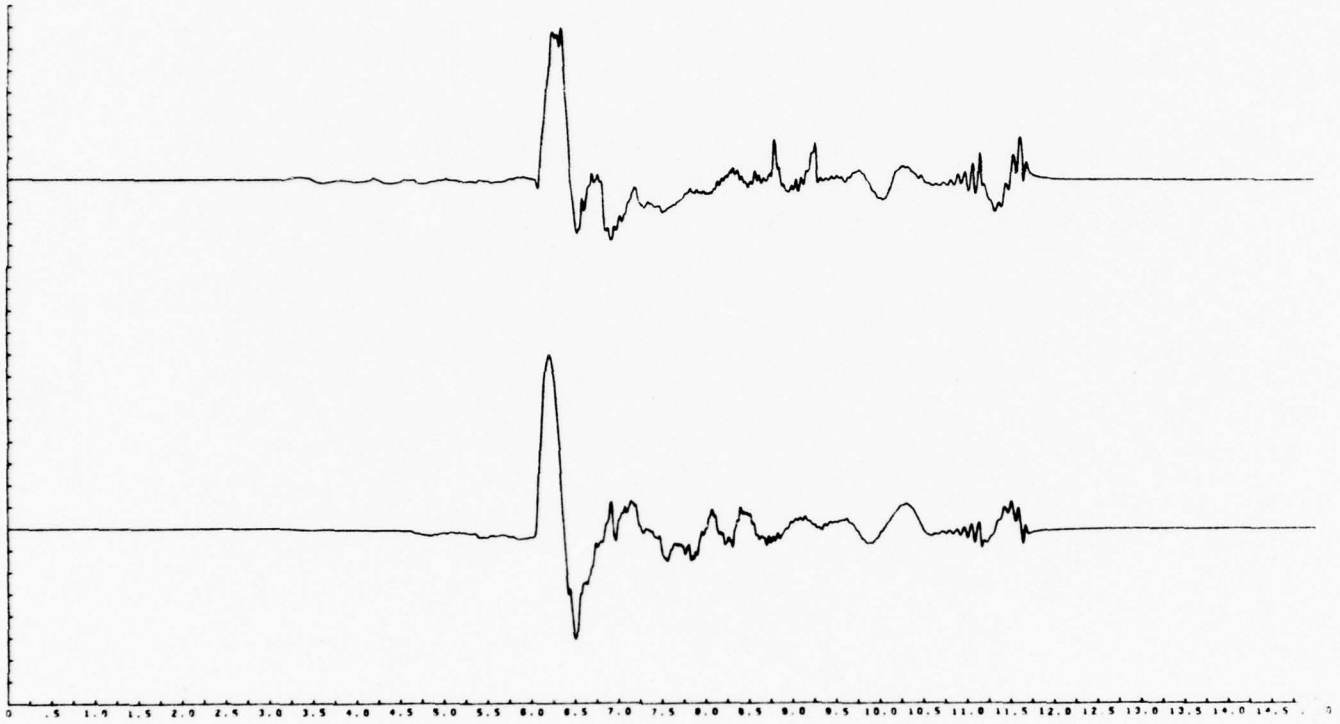


Fig. 4.3(35) Model accelerogram generated under conditions identical to those of Fig. 4.3(34) except now the rise time is 0.5 sec. The ordinate scale is 0.14 g/division/m of dislocation.

BEST AVAILABLE COPY

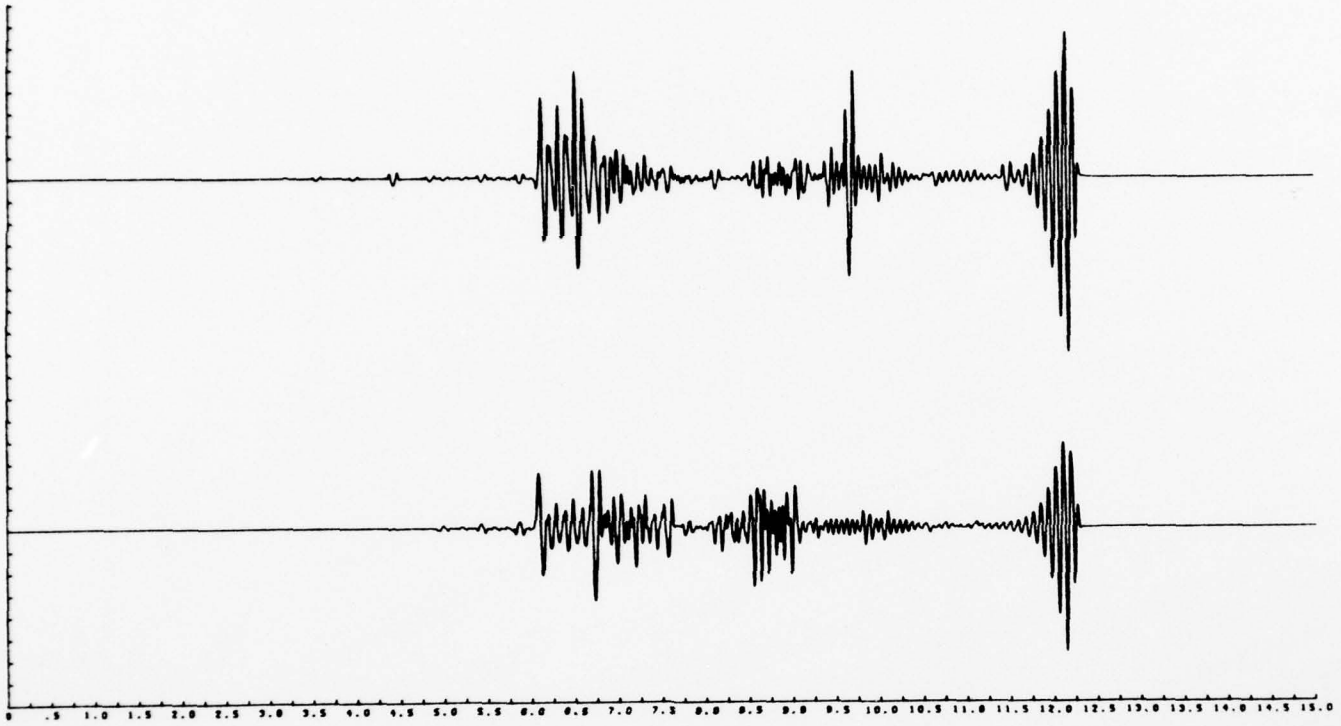


Fig. 4.3(36) Model accelerogram generated using the fault geometry of Fig. 4.3(30) and the source-instrument term of Fig. 3.3(6) (source three) with a rise time of 0.1 sec. Fault rupture begins at the hypocenter and propagates along the fault at 2.166 km/sec. The ordinate scale is 4.18 g/division/m of dislocation.

BEST AVAILABLE COPY

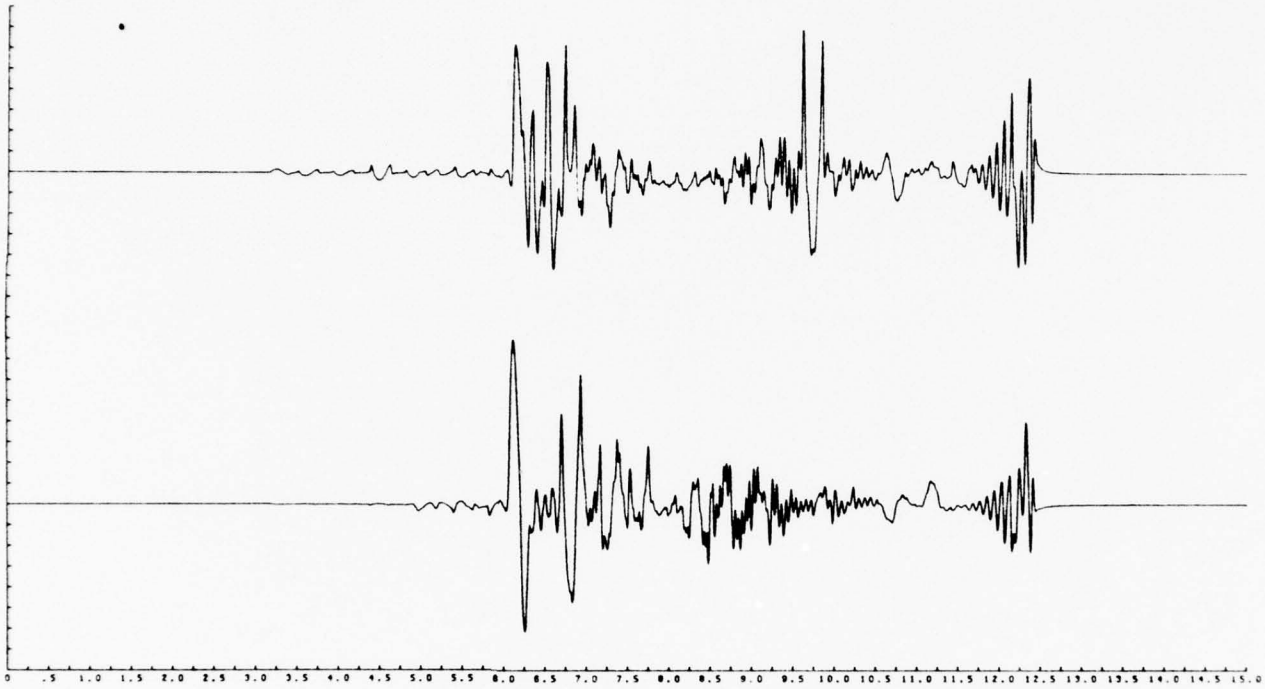


Fig. 4.3(37) Model accelerogram generated under conditions identical to those of Fig. 4.3(36) except now the rise time is 0.25 sec. The ordinate scale is 0.27 g/division/m of dislocation.

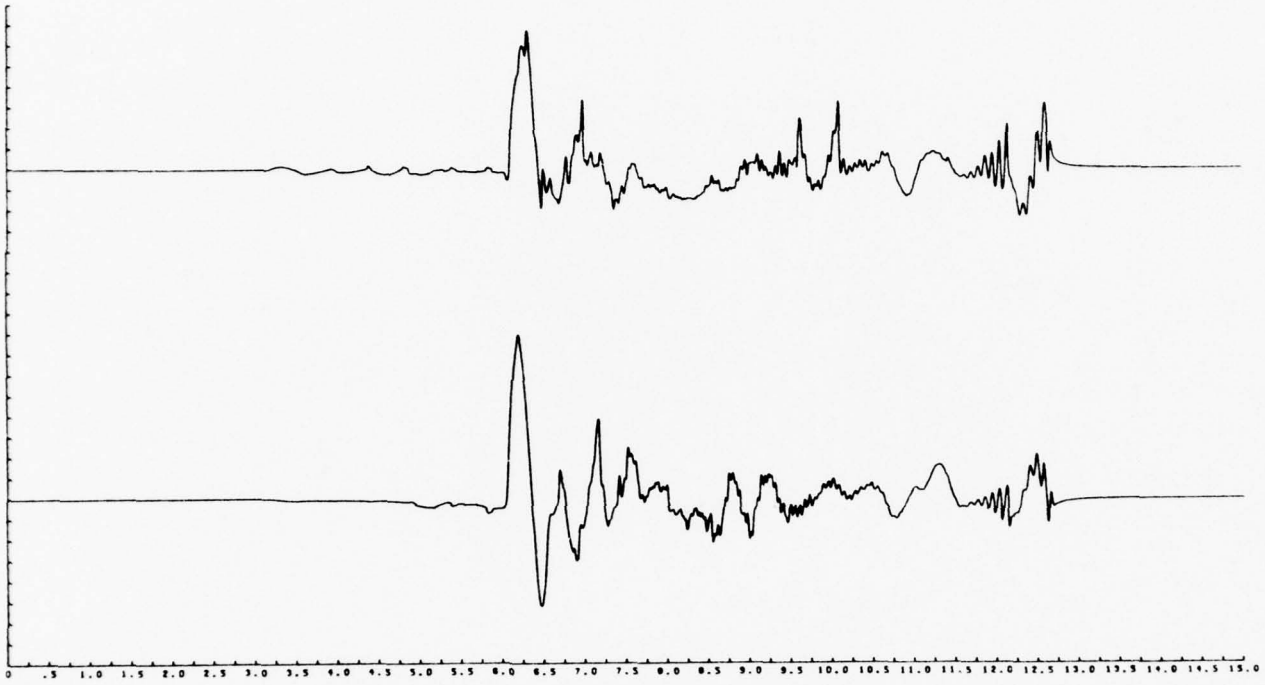


Fig. 4.3(38) Model accelerogram generated under conditions identical to those of Fig. 4.3(36) except now the rise time is 0.5 sec. The ordinate scale is 0.09 g/division/m of dislocation.

BEST AVAILABLE COPY

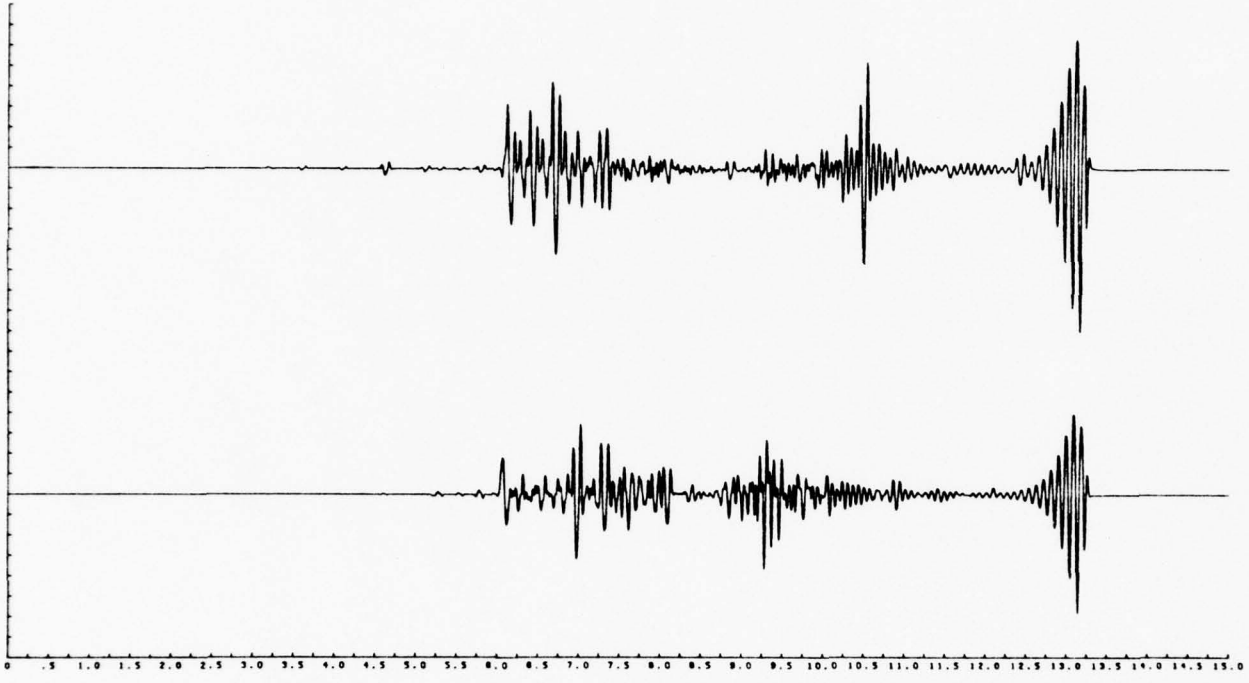


Fig. 4.3(39) Model accelerogram generated using the fault geometry of Fig. 4.3(30) and the source-instrument term of Fig. 3.3(6) (source three) with a rise time of 0.1 sec. Fault rupture begins at the hypocenter and propagates along the fault at 1.969 km/sec. The ordinate scale is 4.05 g/division/m of dislocation.

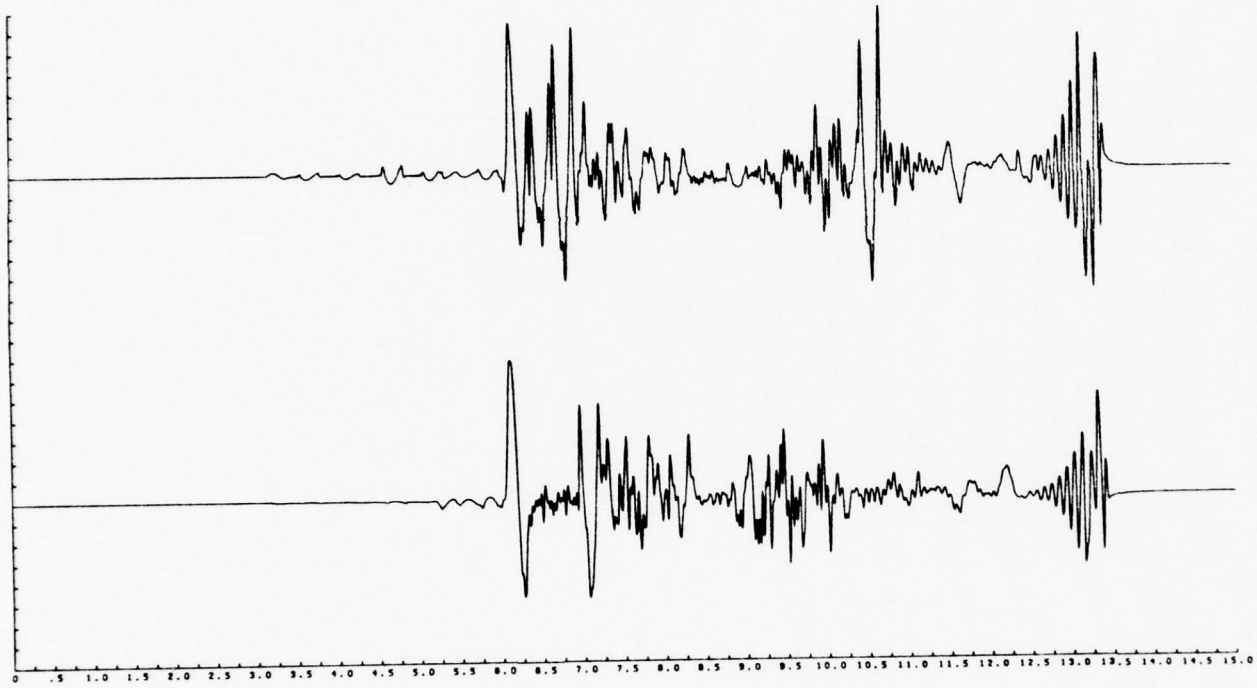


Fig. 4.3(40) Model accelerogram generated under conditions identical to those of Fig. 4.3(39) except now the rise time is 0.25 sec. The ordinate scale is 0.22 g/division/m of dislocation.

BEST AVAILABLE COPY

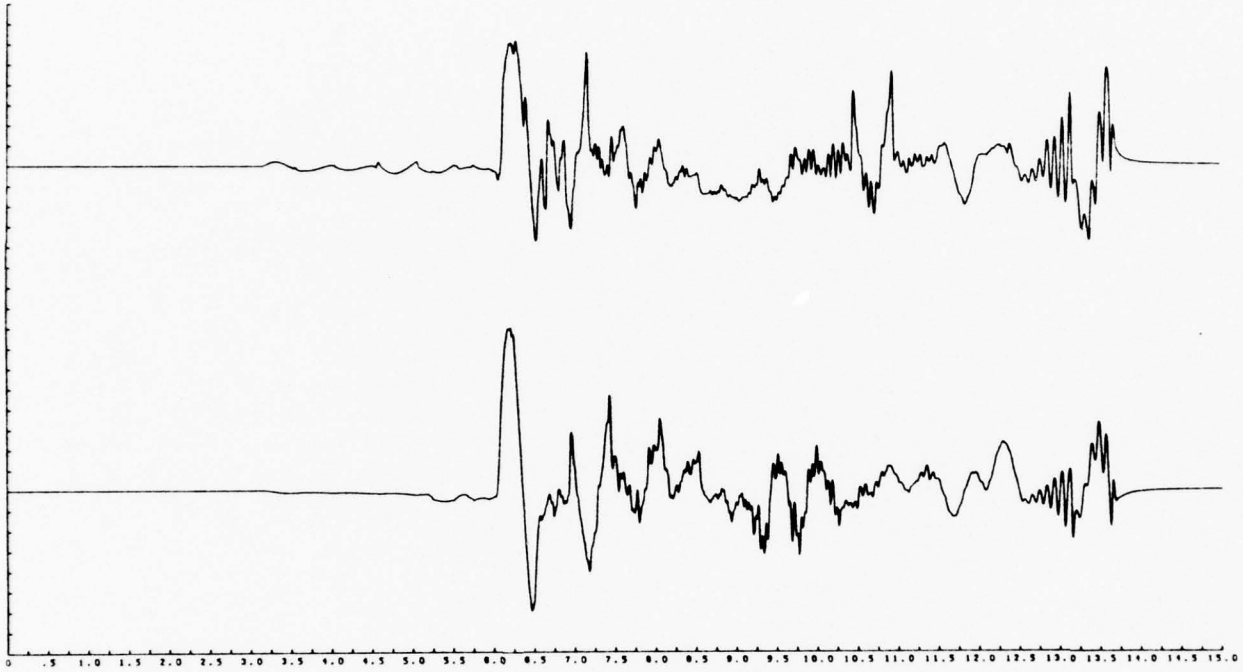


Fig. 4.3(41) Model accelerogram generated under conditions identical to those of Fig. 4.3(39) except now the rise time is 0.5 sec. The ordinate scale is 0.06 g/division/m of dislocation.

BEST AVAILABLE COPY

respectively. The ordinate scales are 4.05, 0.22, and 0.06 g/division/m of dislocation implying fault displacements of 0.08, 1.40, and 5.58 meters under the usual constrain imposed by the observed Pacoima Dam peak acceleration.

The first and most significant contention that may be made about the records of this series is that they look rather like the resolved Pacoima Dam records we wish to match. Since the fundamental difference between the input parameters of these models and all previous efforts is in the fault geometry used, it is obvious that the current fault geometry is more in accord with the actual faulting that took place during the San Fernando earthquake. This is hardly surprising in view of the wealth of independent evidence of previous studies. What, perhaps, is surprising is the support by high-frequency model motions of inferences derived from much longer period data. This is a result of far-reaching import.

Let us begin by compiling a list of features of the model records which are believed to be in substantial agreement with the resolved Pacoima Dam records of Figure 4.2(4). Most striking is the manner in which the relative amplitudes of the model accelerograms match their observed counterparts. The term relative amplitudes is used here to describe both the variation of amplitude with time of either component and the ratio at any given time of the amplitude of one component to that of the other. Specifically the record amplitudes between the arrival of the first P-wave and the first S-wave are quite small, the horizontal component motion being somewhat smaller than the vertical in agreement with observation. Analysis of all the eight records of this series shows that this conclusion is generally valid although details

differ somewhat from record to record. The arrival of the S-wave energy precipitates a 1 to 1.5 second packet of much greater amplitude motion which is somewhat more prolonged and energetic on the horizontal component. Again, the feature of the model records which is quite general is in general agreement with observation. Following the arrival of the shear energy from the hypocentral region, an interval of several seconds during which a marked decrease in record amplitude occurs is seen. This decrease is more noticeable on the vertical record. After this interval another energetic arrival is found on the vertical component while the horizontal component remains quiet. At this point the match between model and observed records becomes much less satisfactory. However, as we shall shortly see the model time histories between the first P-wave arrival and the first prominent arrival after the hypocentral region S-wave are generated by motions along the fault from the hypocenter to a point less than two kilometers below the ground surface. Thus, considerations of relative amplitudes alone would indicate that over the initial 80 percent of its length the model fault of Figure 4.3(30) is adequate to explain the observed Pacoima Dam records. This, in turn, leads to several important conclusions. Since the amplitude configuration described above is generally true for a variety of fault rupture propagation velocities and source rise times, it must be approximately independent of both, at least over the ranges of these parameters that have been investigated. This is, of course, completely equivalent to stating that the relative amplitudes of model accelerograms are powerfully dependent on the source-receiver geometry. The same is presumably true of real accelerograms.

Since all the model records of this series were generated assuming

a constant fault rupture propagation velocity and a constant dislocation amplitude over the entire fault surface, it is clear that rapid or large variations of these parameters are not necessary to explain the first six-to-seven seconds of the Pacoima record. This is certainly a pleasing result from a modeling standpoint. More importantly, it specifically argues against the conceptulization of strong high-frequency motions as the result of an essentially random process, at least in the particular case of the San Fernando earthquake.

At this point we must consider a problem that has been previously ignored primarily because model accelerograms generated had not achieved a fit to the observed data of a degree to warrant its consideration. As mentioned above, even the best models thus far generated are successful only in matching the first 6.5 seconds of observed record motion. However, the actual peak acceleration of 1.25 g, which has been used to calculate the implications of any given model to average fault dislocation ampltiude, occurs after this time. The peak acceleration in that part of the actual Pacoima Dam records for which a good model fit is obtained is much less than this value being approximately 0.6 g. It is this value which should, more properly, be used to calculate the average fault dislocation amplitudes. This observation only strengthens the conclusion of the general unacceptability of early model motions. The implication of this refinement to the average fault dislocation amplitudes to be inferred from any model is to approximately halve previously quoted values.

Are there other features of the observed records that may be duplicated by some model? The answer is apparently yes. For several model accelerograms, most notably for that employing a fault rupture

propagation velocity of 1.969 km/sec and a source rise time of 0.25 sec, the character of the vertical component initial shear wave arrival on the Pacoima Dam records is rather well duplicated. This motion is a distinctive series of approximately 4 Hertz oscillations of approximately one second duration. The next really distinctive arrival on the vertical component is a single pulse of about the same frequency occurring some three seconds after the onset of the S-wave motion. This pulse is faithfully duplicated on virtually all model accelerograms but has the proper frequency content only on those with 0.25 sec rise times.

There are also notable failures of any of the artificial records to match some features of the observed motion. The comparison between model and real horizontal motion is generally much less satisfactory than a similar comparison between vertical motions. This is difficult to explain in terms of minor model parameter variation especially for the first horizontal S-wave pulse which apparently have significantly different frequency content on the vertical and horizontal Pacoima Dam records. For the moment let it merely be contended that the best model found of those tried is that employing the Alewine and Jordan derived fault geometry, a fault rupture propagation velocity of approximately 2 km/sec, and a rise time of 0.25 sec. This model rather well duplicates the first 6.5 seconds of the recorded Pacoima Dam vertical component both with respect to amplitude and phase character but does a considerably less impressive job of matching the recorded horizontal component with respect to the character of the individual phases although the overall amplitude variation with time relative to the vertical component is fairly successful.

4.4 Discussion of the Results

The purpose of this section is essentially to set reasonable limits of uncertainty on the basic model parameters. The achievement of this goal is aided by the deterministic nature of the modeling process. That is, we have access to the origin of each feature of the model motion either explicitly through consideration of the equations governing it or implicitly by observation of the effect of parameter variation. It is possible to pick a distinctive phase and unambiguously state that it is due to a given type of elastic wave arrival from a specific part of the model fault. Insofar as we may confidently pair such an arrival with one on the observed record the same conclusions hold for the actual record motion.

Let us begin in the most straightforward way imaginable. That is, let us calculate for some particular model the arrival times of body wave phases from significant parts of the fault. In this analysis, which is wholly an exercise in geometry, we will use the model accelerogram of Figure 4.3(40) which was found to be a fairly successful attempt to reproduce the observed accelerations. As we have seen this model employs a fault derived from that of Alewine and Jordan (1973), a rupture propagation velocity of 1.969 km/sec and a rise time of 0.25 sec for source-instrument term three. The points of interest along this fault from which phase arrivals will be calculated are, in order of origin along the fault with decreasing depth:

i) the hypocenter - point a

ii) the point at which the slope of the fault changes from 52° to 40° - point b

iii) the point at which the slope of the fault changes

from 40° to 35° - point c

iv) the lower point of intersection of the fault plane with the wedge of $\theta \leq \theta_{cr}$ where θ_{cr} is the critical angle as discussed in Chapter 2 and where θ and θ_{cr} are measured from the vertical at the receiving station - point θ^{L}_{cr}

v) the upper point of intersection of the fault plane with the wedge of $\theta \leq \theta_{cr}$ - point θ^{U}_{cr}

vi) the point of closest approach of the fault plane to the receiving station - point CA

vii) the point at which the slope of the fault plane changes from 35° to 30° - poind d

viii) the point of intersection of the fault plane with the surface of the half space - point e

The coordinates of these points as well as of the receiving station are given in Table 4-1. The reasons for selecting these particular points is quite obvious. In the case of the fault hinge points we expect a reordering of the importances of the various Green's function terms to occur as may be seen from a consideration of equation 3.4-5. Between θ^{L}_{cr} and θ^{U}_{cr} no energy in the form of SP motion may arrive at the receiving station. Thus it is of interest to look for differences in the character of the record in this interval that might distinguish it from the remainder of the record. Finally, the point of closest approach is a superficially obvious place from which to expect large-amplitude motion.

As in Table 4-1 let us designate the model equivalent of the receiving station at Pacoima Dam as point PD. Then, where $\overline{ab}$ is the

Table 4-1

Co-ordinates of proposed significant points of hinged fault model

Point	Description	Co-ordinates
a	Hypocenter	(0.0,14.0)
b	Point at which the slope of the fault changes from 52° to 40°	(3.91,9.0)
c	Point at which the slope of the fault changes from 40° to 35°	(6.29,7.0)
θ^{L}_{cr}	Lower point of intersection of the fault plane with the wedge of $\theta \leq \theta_{cr}$	(6.37,6.95)
θ^{U}_{cr}	Upper point of intersection of the fault plane with the wedge of $\theta \leq \theta_{cr}$	(12.29,2.80)
CA	Point of closest approach of the fault plane to the receiving station	(12.47,2.68)
d	Point at which the slope of the fault changes from 35° to 30°	(14.86,1.0)
e	Point of intersection of the fault plane with the surface of the half-space	(16.59,0.0)
PD	Pacoima Dam - the receiving station	(10.59,0.0)

length of the line segment between points a and b and where v_p, v_s, and v_f are the compressional wave, shear wave, and fault rupture propagation velocities, respectively, the arrival of the P-wave from point c is simply

$$\overline{ab}/v_f + \overline{bc}/v_f + \overline{cPD}/v_p$$

The time interval between the arrival of this phase and the arrival of the hypocentral P-wave is the difference between the above quantity and $\overline{aPD}/v_p$. In this way a number of relative or absolute arrival times may be worked out. The computation of the arrival times of SP phases are somewhat more complex but hardly more difficult.

In Figure 4.4(1) are presented the arrival times of the compressional phases from each of the above eight points superimposed on the model accelerogram of Figure 4.3(40). Only one arrival is shown for P-waves from points c and θ^L_{cr}. This is due to the extreme proximity of these two points for the particular fault geometry used as may be seen by comparing their coordinates in Table 4-1. In Figures 4.4(2) and 4.4(3) are presented similar plots for S- and SP-wave arrivals. Again, in both cases arrival times from points c and θ^L_{cr} are essentially indistinguishable.

Perhaps the single most impressive feature of these three plots is the complete unconcern of the model motions for my seismological preconceptions. With a few exceptions to be discussed below, not a single important feature of the model records can be attributed to phase arrivals from any of the points proposed as significant.

The most notable exception, of course, is the initial S-P interval. This interval, which is not dependent upon the fault rupture propagation velocity but only upon the hypocenter-receiver separation and the shear-

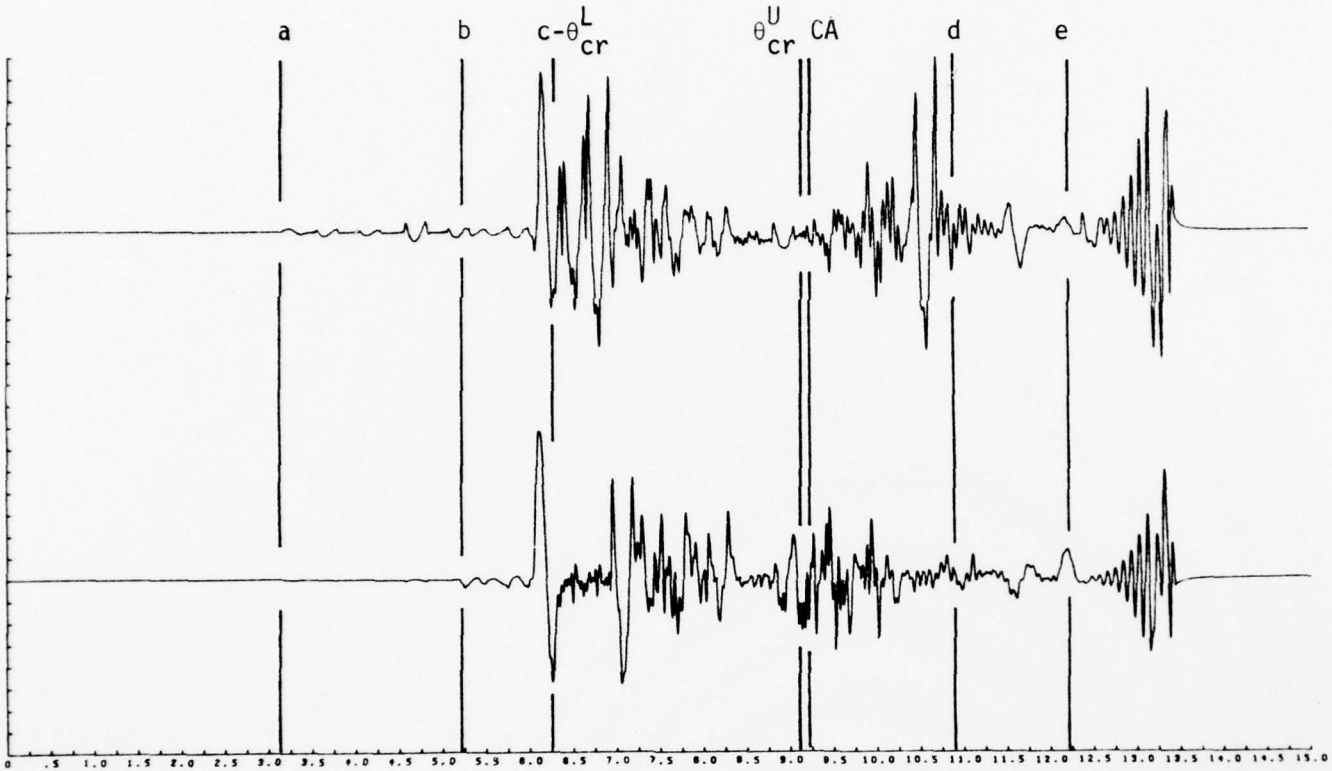


Fig. 4.4(1) P-wave arrivals from the significant points of Table 4-1 for a fault rupture propagation velocity of 1.969 km/sec. The model accelerogram upon which these arrival times are superposed is that of Fig. 4.3(40).

BEST AVAILABLE COPY

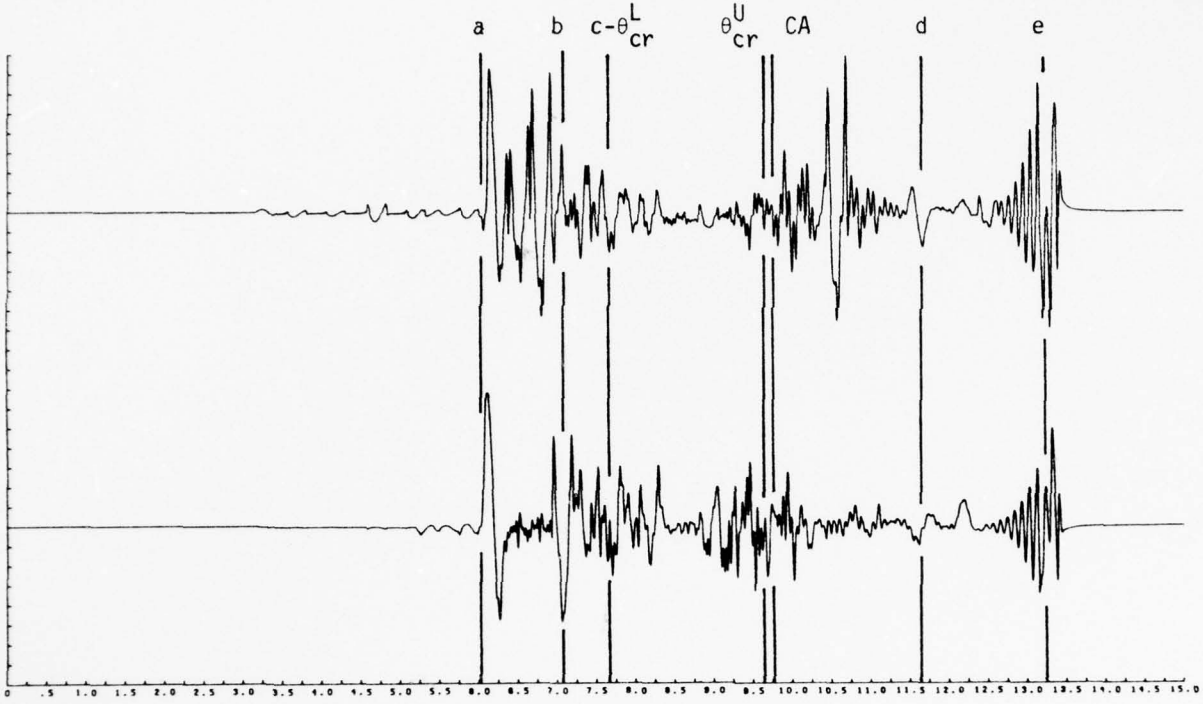


Fig. 4.4(2) S-wave arrivals from the significant points of Table 4-1 for a fault rupture propagation velocity of 1.969 km/sec. The model accelerogram upon which these arrivals are superposed is that of Fig. 4.3(40).

BEST AVAILABLE COPY

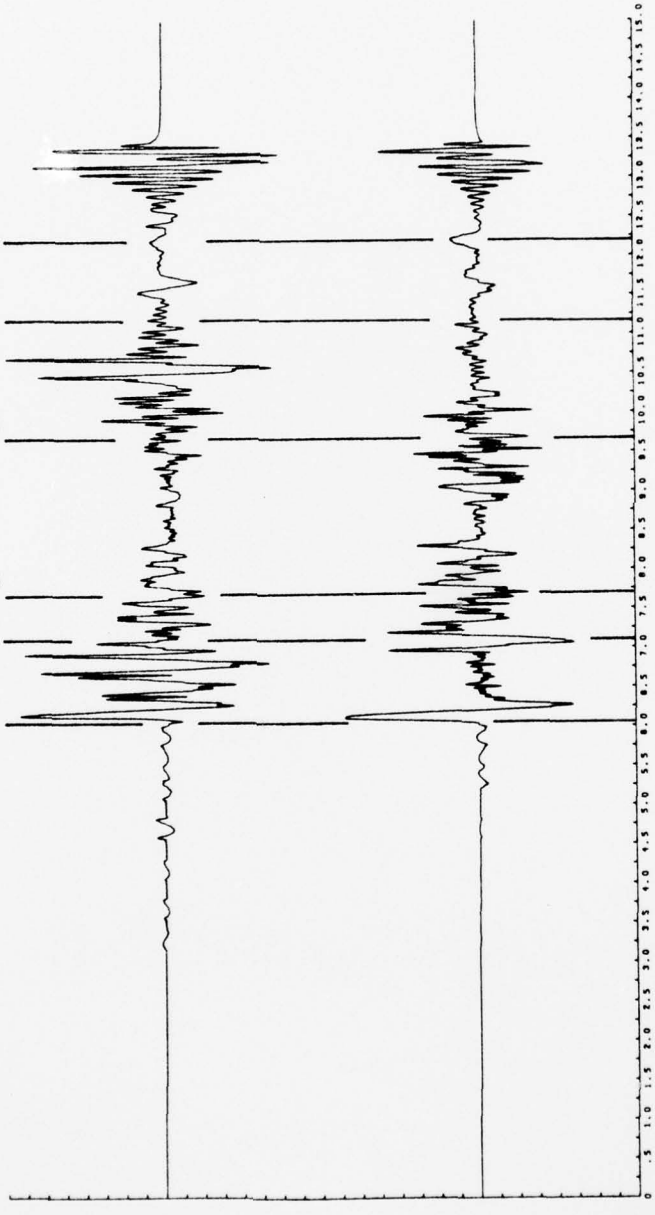


Fig. 4.4(3) SP-wave arrivals from the significant points of Table 4-1 for a fault rupture propagation velocity of 1.969 km/sec. The model accelerogram upon which these arrival times are superposed is that of Fig. 4.3(40).

and compressional-wave velocities, is 2.91 seconds. That is a somewhat higher value than observation would indicate. Assuming that the Pacoima Dam accelerometers were tripped very near the initial P-wave arrival and that the S-wave arrival is signaled in actuality by the onset of long-period motion on the horizontal records, a more realistic S-P interval for the observed case is approximately 2.5 seconds.

The model and observed intervals may be reconciled by decreasing the model hypocenter-receiver distance, by decreasing the model compressonal wave velocity, or by increasing the model shear-wave velocity. The last alternative seems the most satisfactory since the S-wave velocity employed is lower than that of other studies--2.9 as opposed to 3.2 or 3.3 km/sec. A shear-wave velocity of 3.1 km/sec for this geometry and a P-wave velocity of 5.58 km/sec produces an S-P interval of 2.52 sec in much better agreement with observation. We shall keep this point in mind as a source of uncertainty in other faulting parameters which are implicitly dependent on the S-wave velocity.

Another minor exception to the failure of the generated motion to obey our preconceptions is in the case of the P-wave arrival from point b. A small but definite increasein P-wave amplitude is seen to occur at the arrival of compressional energy from this point. Can we explain the general unimportance to model motion of the rapid changes in fault dip? It turns out that we can and that the explanation is surprisingly simple.

Consider from equation 3.4-5 the fault slope dependence of the total solution

$$u_1(\text{horizontal}) = \mu\{\sin 2\theta[G_{11,1} - G_{13,3}] - \cos 2\theta[G_{11,3} + G_{13,1}]\}$$

$$u_3(\text{vertical}) = \mu\{\sin 2\theta[G_{31,1} - G_{33,3}]$$

$$- \cos 2\theta[G_{33,1} + G_{31,3}]\}$$

In these equations θ is the dip of the fault. Thus $\sin 2\theta$ and $\cos 2\theta$ may be thought of as the coefficients due to the fault orientation which determine which of the spatial derivatives of the Green's functions--$G_{ij,p}$--will be of dominant importance. Unlike the source-receiver angular dependence buried within the Green's functions (also, somewhat unfortunately, symbolized by θ in Chapter 2) which is varying constantly as the fault rupture process propagates from the hypocenter to the half-space surface these 2θ dependent coefficients remain constant for constant fault plane orientation. Thus, in going from the fault segment between points a and b to that between points b and c, 2θ changes from 104° to 80° and the factors $\sin 2\theta$ and $\cos 2\theta$ change from 0.970 and -0.242 to 0.985 and 0.174, respectively. This is simply not a large effective difference. Apparently it is virtually insignificant when compared to the variation of the Green's functions themselves over rather small distances. Similarly, the variations of $\sin 2\theta$ and $\cos 2\theta$ between the fault segments $\overline{bc}$ and $\overline{cd}$ are 0.985 to 0.940 and 0.174 to 0.342. Finally, between segments $\overline{cd}$ and $\overline{de}$ the variation in $\sin 2\theta$ is from 0.940 to 0.866 while that of $\cos 2\theta$ is from 0.342 to 0.500. These changes, if they are visible at all are obscured by the complexity of motions in the latter part of the record where, unlike the case of compressional arrivals from point b, different elastic wave types are simultaneously arriving from different parts of the fault.

Figure 4.4(3) graphically shows that very little of the character of the model accelerogram can be attributed to the SP phase as defined in Chapter 2. This may very well be due to the small amplitude of this

phase relative to the other body-wave phases, especially the S-wave. In particular, that section of the model record during which no SP motion is allowed (between the SP arrivals from θ_{cr}^{L} and θ_{cr}^{U} in Figure 4.4(3)) is not apparently different from those portions directly adjacent.

This leaves only the arrivals from the point of closest approach of fault to receiver. Any contention that this point is significant must apparently be regarded as unconvincing. Simply very little is happening at the appropriate time. This must be due to the fact that a point dislocation does not radiate energy independently of azimuth but prefers some directions to others. Thus the amplitude at the receiver is greatly affected by the source-receiver angular relationship and not merely by source-receiver separation. The necessary angular condition for large-amplitude motion is lacking in this case. Conversely, they must be fulfilled in the case of the aforementioned single pulse visible on all model accelerograms of the last series. This pulse represents one of the most convincing equivalencies between model and observed motion so it is worthwhile to dwell on its implications for a moment.

Assuming that this pulse is indeed equivalent to that on the Pacoima Dam vertical component at approximately 5.8 seconds after the onset of the record motion, what may we infer about the actual fault rupture history? It seems most likely that the model pulse is due to an S-wave arrival from some point on the fault near its upper end. This is supported by Figure 4.3(1) which shows the ground displacement from a single point dislocation with the Heaviside unit step source function. In this figure, in which the source-receiver geometry is fairly

comparable to one appropriate for a source near the upper end of the fault of Figure 4.3(30) the amplitude of the S-wave motion is seen to be completely predominant. Given, then, that this pulse on the model accelerograms is due to some shear-wave arrival, from what point on the fault does it come?

From Figure 4.4(2) we see that it must be from a point between that of closest approach and point d. Indeed, once we have selected an appropriate arrival time for this model pulse it is trivial to construct equations of constraint and solve for the source point uniquely. The exact time of pulse onset is somewhat problematical but 7.2 seconds after the first P-wave arrival seems a good estimate. The S-wave arriving at this time, given a fault rupture propagation velocity of 1.969 km/sec and model compressional and shear velocities of 5.58 and 2.90 km/sec can only come from the point on the fault whose coordinates are (13.32, 2.08). The important thing to note is that alteration of any of these three velocities will change the arrival time of the model pulse but not its character. At least this is what all our previous experience with parameter variation would indicate. We may bring the model interval of 7.2 seconds into closer agreement with the observed interval of 5.8 seconds either by increasing the rupture propagation velocity or the S-wave velocity or by decreasing the P-wave velocity. As before in discussing the S-P interval, the last alternative seems least satisfactory. Changing the shear velocity alone is not likely to be adequate since the source-receiver separation is rather small (3.43 km). This implies that a large change in the S-wave velocity would be necessary. In fact no increase in shear velocity alone will suffice since at the time the pulse in question appears on the observed record the

model has not yet propagated to the critical point on the fault. Therefore, it must be that the difference between model and observed intervals is primarily due to the difference between model and actual fault rupture propagation velocity.

If the entire difference is to be so explained the implied actual rupture velocity is 2.32 km/sec. If the shear velocity is increased somewhat to 3.1 km/sec as we have seen is indicated by the observed S-P interval the pertinent fault rupture propagation velocity falls to 2.30 km/sec. Thus, it would seem that if we have properly matched model and observed phases the average rupture velocity of the faulting process over a very substantial part of the fault may be given as 2.3 km/sec within very restrictive limits of uncertainty. In the absence of confident pairing of other model and actual phases nothing can be said about possible variation of fault rupture velocity along the fault. There is nothing in this study to either support or contradict such a possibility.

Finally, aside from the overall satisfactory appearance of models of the last series employing a source rise time of 0.25 seconds the width of the particular S-wave pulse to which we have been referring also supports this rise time. As may be seen by examining Figures 4.3(34) through 4.3(41) this particular arrival is a sensitive indicator of model source rise time and allows us to contend with some assurance that 0.25 seconds is the best to be found. There is nothing in the character of the vertical S-wave motion coming from the hypocentral region--and thus from a completely different part of the fault--to contradict this conclusion.

In terms of the parameters inferred from model studies to be most

appropriate for the faulting episode associated with the San Fernando earthquake of February 9, 1971 we may conclude that rupture occurred along a surface substantially similar to that of Figure 4.3(30), that the form of the dislocation time history was closely approximated by a smoothed ramp whose rise time was near 0.25 seconds, that this dislocation propagated along the fault surface at a velocity near 2.3 km/sec, and that it had an average amplitude of between one and two meters.

Chapter 5

Conclusions and Areas for Future Study

The primary goal of this study was fairly limited: to show whether or not a near-field strong-motion record could be modeled using the mathematical representation of motion arising from dislocations embedded in an elastic homogeneous isotropic half-space and, thus, to add to our knowledge of the seismic source. It is felt that this goal has been realized; if not perfectly, then at least substantially.

To gain knowledge of real phenomena from model studies, of course, the model must duplicate the actuality in some way. The more satisfactory the duplication the more far-reaching and likely are the inferences that may be drawn. The question of drawing valid inferences from an imperfect model is a delicate one largely defying generalization but it is believed that the following conclusions may be reached from this study:

1) It is clear both from the discussion in Chapter 3 and from the many different accelerograms presented in Chapter 4 that in order to adequately characterize the high-order behavior of real dislocation source functions frequencies must be considered that are high relative to the inverse of the source rise time. Given most proposed rise times and the instrument response spectra of modern seismographs this implies that it is necessary to consider accelerometer records. This is far from a trivial point since the accelerations to be expected from different seismic sources are just as important as the velocities, displacements, and magnitudes to be expected from these same sources.

2) The characterization of accelerations associated with any earthquake as being the result of an essentially random process no longer seems quite as necessary. This concept is valid only so long as it is maintained that small portions of the source act independently of each other. The evidence of this thesis weakens the necessity of this notion for the San Fernando earthquake. The general character and many individual features of an actual accelerogram may evidently be duplicated by considering a faulting process that is perfectly homogeneous over the entire fault surface. It is not necessary, for the first 6.5 seconds of the Pacoima Dam record at least, to call upon specialized situations to occur at particular points. This is most notably true for those portions of the record associated with the peak recorded accelerations in that part of the observed accelerogram for which a good model match was obtained. This conclusion suggests many interesting ramifications. For example, although it is mechanically simple to postulate situations with a dislocation model in which long- and short-period phenomena are virtually unrelated, it appears that this is not always the case. This, in turn, implies that the vast scatter observed in empirical relations between magnitude and acceleration are not necessarily a fundamental property of the seismic source but may be due to other complexities such as those that undoubtedly exist in the medium between source and receiver. This argument is made less convincing by the

the failure of any model to match the observed motion in that part of the Pacoima Dam records in which the peak acceleration of 1.25 actually occurred. It is also less convincing as very large-magnitude events are considered where some material inhomogeneity must occur over the fault surface. However, the implication of this study is that aspects of fault motion of substantially disparate frequencies are more closely related than was previously believed.

3) A practically important principal, termed previously the conservation of character, has emerged for strong-motion accelerometer model studies. This principal states that near the source the effects of variation of source rise time, source rupture propagation velocity, and source-receiver geometry are quite separate and distinguishable for high-frequency ground motions.

Areas for future study are many but they can, perhaps, be placed into two broad categories. The first involves better model refinement so that better knowledge of the processes occurring at the seismic source may be obtained. For example, the two-dimensional source may be fundamentally objectionable in that it requires the simultaneous rupture of greatly separated parts of the fault. This is not intuitively pleasing and it becomes less tractable as the total size of the source increases. It is clearly desirable to extend the two-dimensional method of this thesis to a three-dimensional method. Such an extension will lead to a major increase in computational complexity but in principal there is no reason why it cannot be accomplished. The groundwork for

such an extension has already been done (Johnson, 1974).

The second major area for future research is the converse to the first. If we may successfully model the motion on a fault from a given accelerogram then we may also successfully produce the acceleration to be expected from a given fault motion. The implications to earthquake-resistant design of structures in a given geologic setting would be significant. Certainly the gross characterization of the strong motion to be expected at a given site by duration, peak acceleration, general frequency content, and amplitude variation with time would be an important step towards rational engineering design.

Finally, as with any study, there are important questions left to be resolved by future investigations. The failure to duplicate the observed motion after the first 6.5 seconds is disappointing particularly in view of the fact that the peak acceleration occurred in the later part of the Pacoima record. The failure of any model horizontal component to equal the success of its vertical counterpart is a fundamental problem that remains unexplained. As more data becomes available from future earthquakes it is hoped that these difficulties may be overcome.

Perhaps it is best merely to contend that many of the properties of strong motion that are now obscure are indeed fathomable. In a small way it is believed that this work supports this contention.

References

Alewine, R.W. and T.H. Jordan (1973). Generalized inversion of earthquake static displacement fields, Geophys. J. Roy. astr. Soc. 35, 357-361.

Allen, C.R., G.R. Engen, T.C. Hanks, J.M. Nordquist, and W.R. Thatcher (1971). Main shock and larger aftershocks of the San Fernando earthquake, February 9 through March 1, 1971, U.S. Geol. Surv. Prof. Pap. 733, 17-20.

Allen, C.R., T.C. Hanks, and J.H. Whitcomb (1975). Seismological studies of the San Fernando earthquake and their tectonic implications, Calif. Div. Mines Geol. Bull. 196, 257-262.

Berger, J. (1971). Some observations of the San Fernando, California, earthquake with a laser strain meter, U.S. Geol. Surv. Prof. Pap. 733, 150-152.

Bolt, B.A. (1972). San Fernando rupture mechanism and the Pacoima strong-motion record, Bull. Seism. Soc. Am. 62, 1053-1061.

Bolt, B.A., and B.S. Gopalakrishnan (1975). Magnitudes, aftershocks, and fault dynamics, Calif. Div. Mines Geol. Bull. 196, 263-272.

Boore, D. (1972). The effect of simple topography on seismic waves: Implications for the recorded accelerations at Pacoima Dam, (abs) Nat. Conf. Earthquake Eng., Los Angeles.

Brady, A.G., D.E. Hudson, and M.D. Trifunac (1971). Strong motion earthquake accelerograms Vol. 1, C, Uncorrected accelerograms, EERL 71-20, Earthquake Eng. Res. Lab., Calif. Inst. of Tech., Pasadena.

Burford, R.O., R.C. Castle, J.P. Church, W.T. Kinoshita, S.H. Kirby, R.T. Ruthven, and J.C. Savage (1971). Preliminary measurements of tectonic movement, U.S. Geol. Surv. Prof. Pap. 733, 80-85.

Burridge, R. and L. Knopoff (1964). Body force equivalents for seismic dislocations, Bull. Seism. Soc. Am. 54, 1875-1888.

Cagniard, L. (1939). Reflexion et Refraction des Ondes Seismiques Progressives, Gauthier-Villars, Paris.

_____(1962). Reflection and Refraction of Progressive Seismic Waves, translated by Dr. Edward A. Flinn, McGraw-Hill, New York.

Canitez, N. and M.N. Toksöz (1972). Static and dynamic study of earthquake source mechanism: San Fernando earthquake, J. Geophys. Res. 77, 2583-2594.

Chinnery, M.A. (1963). The stress changes that accompany strike-slip faulting, Bull. Seism. Soc. Am. 53, 921-932.

Chinnery, M.A. and J.A. Petrak (1968). The dislocation fault model with a variable discontinuity, Tectonophysics 5, 513-529.

Dillinger, W. and A.F. Espinosa (1971). Preliminary fault-plane solution for the San Fernando earthquake, U.S. Geol. Surv. Prof. Pap. 733, 142-149.

Hanks, T. (1974). The faulting mechanism of the San Fernando earthquake, J. Geophys. Res. 79, 1215-1229.

Hanks, T., T.H. Jordan, and J.B. Minster (1971). Precise locations of aftershocks of the San Fernando earthquake 2300 (GMT) February 10 - 1700 February 11, 1971, U.S. Geol. Surv. Prof. Pap. 733, 21-23.

Haskell, N.A. (1969). Elastic displacements in the near-field of a propagating fault, Bull. Seism. Soc. Am. 59, 865-908.

Hoop, A. de (1960). A modification of Cagniard's method for solving seismic pulse problems, Appl. Sci. Res. B, 8, 349-356.

Hudson, D.E. (1972). Strong-motion seismology, Proc., Intern. Conf. Microzonation Safer Construction Res. Appl., Seattle, Washington.

Johnson, Lane R. (1974). Green's function for Lamb's problem, Geophys. J. Roy. astr. Soc. 37, 99-131.

Jungels, P.H. (1973). Modeling of Tectonic processes associated with earthquakes, Ph.D. Thesis, Calif. Inst. of Tech., Pasadena.

Jungels, P.H. and D.L. Anderson (1971). Strains and tilts associated with the San Fernando earthquake, U.S. Geol. Surv. Prof. Pap. 733, 77-79.

Kahle, James E. (1975). Surface effects and related geology of the Lakeview fault segment of the San Fernando fault zone, Calif. Div. Mines Geol. Bull. 196, 119-135.

Kamb, B., L.T. Silver, M.J. Abrams, B.A. Carter, T.H. Jordan, and J.B. Minster (1971). Pattern of faulting and nature of fault movement in the San Fernando earthquake, U.S. Geol. Surv. Prof. Pap. 733, 41-54.

Mansinha, L. and D.E. Smylie (1971). The displacement fields of inclined faults, Bull. Seism. Soc. Am. 61, 1433-1440.

Maruyama, T. (1963). On the force equivalents of dynamical elastic dislocations with reference to the earthquake mechanism, Bull. Earthquake Res. Inst., Tokyo Univ. 41, 467-486.

_____(1964). Statical elastic dislocations in an infinite and semi-infinite medium, Bull. Earthquake Res. Inst., Tokyo Univ. 42, 289-368.

Mikumo, T. (1973). Faulting process of the San Fernando earthquake of February 9, 1971 inferred from static and dynamic near-field displacements, Bull. Seism. Soc. Am. 63, 249-270.

Niazy, A.M. (1974). An exact solution for a finite moving dislocation in an elastic half-space, with application to the San Fernando earthquake of 1971, Ph.D. Thesis, Mass. Inst. of Tech., Cambridge, Massachusetts.

Nigam, N.C. and P.C. Jennings (1968). Digital calculation of response spectra from strong-motion earthquake records, Earthquake Eng. Res. Lab., Calif. Inst. of Tech., Pasadena.

Reimer, R.B. (1973). Deconvolution of seismic response for linear systems, EERC 73-10, Univ. Calif., Berkeley.

Solomon, S. (1971). Seismic wave attenuation and the state of the upper mantle, Ph.D. Thesis, Mass. Inst. of Tech., Cambridge, Massachusetts.

Steketee, J.A. (1958). Some geophysical application of the elasticity theory of dislocations, Can. J. Phys. 36, 1168-1198.

Trifunac, M.D. (1973). Scattering of plane SH waves by a semi-cylindrical canyon, Inter. J. Earthquake Eng. and Dyn. of Struct. 1, 267-281.

_____(1974). A three-dimensional dislocation model for the San Fernando, California, earthquake of February 9, 1971, Bull. Seism. Soc. Am. 64, 149-172.

Trifunac, M.D. and D.E. Hudson (1971). Analysis of the Pacoima Dam accelerogram - San Fernando, California earthquake of 1971, Bull. Seism. Soc. Am. 61, 1393-1411.

Tsai, Y.B. and K. Aki (1969). Simultaneous determination of the seismic moment and attenuation of seismic waves, Bull. Seism. Soc. Am. 59, 275-287.

Tsai, Y.B. and H.J. Patton (1972). Near-field small earthquakes--dislocation motion, Semi-annual Technical Report No. 1, AFOSR Contract No. F44620-72-C-0073, Texas Instruments Incorporated, Dallas.

_____(1973). Dislocation motion and theoretical far-field source spectra of four California earthquakes, Semi-annual Technical Report No. 2, AFOSR Contract No. F44620-72-C-073, Texas Instruments Incorporated, Dallas.

Turnbull, L.S. and J.C. Barris (1973). Interpretation of strong-motion earthquake accelerograms using a moving dislocation model, Semi-annual Report No. 3, AFOSR Contract No. F44620-72-C-0073, Texas Instruments Incorporated, Dallas.

U.S. Geological Survey Staff (1971). Surface faulting, U.S. Geol. Surv. Prof. Pap. 733, 55-76.

Wesson, R.L. and J.F. Gibbs (1971). Crustal structure in the vicinity of the San Fernando, California, earthquake of 9 February 1971. EOS 52, 864.

Wesson, R.L., W.H.K. Lee, and J.F. Gibbs (1971). Aftershocks of the earthquake, U.S. Geol. Surv. Prof. Pap. 733, 24-29.

Whitcomb, J.H. (1971). Fault-plane solutions of the February 9, 1971, San Fernando earthquake and some aftershocks, U.S. Geol. Surv. Prof. Pap. 733, 30-32.